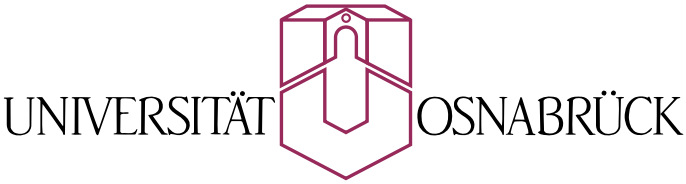

On Classical and Quantum Mechanical Energy Spectra of Finite Heisenberg Spin Systems

Dissertation

zur Erlangung des Grades eines
Doktors der Naturwissenschaften

Dem Fachbereich Physik
vorgelegt von

Dipl.-Phys. Matthias Exler

Osnabrück, März 2006

Betreuer und Erstgutachter	:	Apl. Prof. Dr. J. Schnack
Zweitgutachter	:	Jun.-Prof. Dr. J. Gemmer

Datum der mündlichen Prüfung: 8.Mai 2006

Contents

List of Figures

1 Introduction

Polyoxometalate chemistry has successfully improved the synthesis of magnetic molecules in recent years. Since the synthesis of Mn_{12} [1], which can be regarded as the birth of this new class of materials, many different molecules of various sizes and structures have been produced [2, 3]. These molecules consist of many atoms, but their magnetic nature originates from a number of paramagnetic ions, whose unpaired electrons form collective angular momenta, referred to as spins. The number of interacting spins ranges from as few as two up to several dozens, which is realized in the giant Keplerate molecule $\{Mo_{72}Fe_{30}\}$, where 30 paramagnetic Fe^{3+} ions occupy the vertices of an icosidodecahedron [4].
Magnetic molecules usually appear as macroscopic samples. However, the magnetic interactions between molecules are often negligible compared to the intramolecular interactions. Measurements of the sample hence reflect properties of single molecules, which are significantly different from bulk magnets. Various possible fields of application may be offered by the magnetic molecules, including quantum computing, data storage, nano switches, and even biomedicine [2, 3, 5, 6]. However, some applications have to be considered as speculative so far. Our main interest in magnetic molecules arises from the fact that they represent mesoscopic quantum systems, i.e. they can neither be described as single particles nor as solids.
In most magnetic molecules the localized spins couple antiferromagnetically, and the interaction can be accurately described by the Heisenberg model [7]. For the understanding and prediction of the properties of a spin system, the eigenvalue spectrum of the Hamiltonian has to be calculated or at least approximated. To this end, various methods have been developed, or adopted from other fields.
The existence of symmetries can allow the analytical solution of the eigenvalue problem. Analytical solutions are found very rarely, since their derivations often rely on special substitutions of the operators in the Hamiltonian, which are possible only for certain systems. Furthermore, no general recipe can be given for the development of an analytical solution. The existence (and knowledge) of an analytical solution hence remains an exceptional situation. However, analytical solutions are extremely valuable for the verification of numerical data, so that new algorithms can first be applied to systems whose eigenspectra are known, and used to calculate data for other systems only after they have been proven to deliver accurate results.
Another more general tool for the calculation of the eigenvalue spectrum is the numerical exact diagonalization method. It is not limited to a special class of systems,

but only by the size of the Hilbert space of the model. The term "numerical exact method" refers to the fact that the method uses the unmodified Hamiltonian, hence it is exact, but incorporates numerical algorithms to perform the diagonalization. This approach is therefore only exact with respect to the numerical precision of the algorithm and the computer it is processed on. Exact diagonalization is limited to small systems, since the size of the Hilbert space grows exponentially with the number of spins, although the exploitation of symmetries can help to reduce the effective size [8].
For the analysis of ground state (or low-temperature) properties, the Lanczos or DMRG methods [9] extend the class of numerically treatable molecules, since they reduce the numerical effort by targeting only a limited number of eigenstates.
Monte Carlo methods have been utilized to calculate thermodynamic properties directly, but their main focus is on the behavior of an infinite lattice of spins [10]. Although the simulations are performed with a finite number of spins, the results are extrapolated after analyzing the dependence on the system size. The application of Monte Carlo methods to magnetic molecules is only found rarely, e.g. in references [11, 12].
The methods presented above operate on the unmodified Hamiltonian, the approximation arises from the use of numerical algorithms with a limited precision or the reduction of the set of solutions. Another approach of approximation is the substitution of the Hamiltonian by a simplified model that can be diagonalized more easily. The Ising model, e.g., reduces an $s = \frac{1}{2}$ Heisenberg system to a dependence on only the z-component, and the Ising Hamiltonian is automatically diagonal in the basis of $\hat{S}^z$-eigenstates. Analytical solutions are known for both one- and two-dimensional Ising systems, hence the Ising model has become the standard model to demonstrate and verify Monte Carlo implementations [10].
For the class of magnetic molecules, the rotational band model was introduced to describe the low-energy spectrum of the antiferromagnetic Heisenberg Hamiltonian [13]. Whereas some structures (e.g. dimer, trimer, tetrahedron) possess strict rotational bands, the spectra of ring systems and various polytopes were shown to exhibit a nearly quadratic dependence on the total spin S.
In this work, we will use the rotational band model to derive an approximation of the inelastic neutron scattering (INS) cross-section of $\{Mo_{72}Fe_{30}\}$ (see chapter 2). We will analyze the degeneracies of the eigenvalues and infer the dependence of the energy spectrum on an external magnetic field. Our results are then compared to INS experiments, which were performed at various temperatures and magnetic field strengths. The verification of our results by comparison with the experiment is intended to broaden the knowledge of the range of applicability of the rotational band model. The model has already been shown to comply with magnetization and susceptibility data [14], but since inelastic neutron scattering can directly measure the excitation spectrum of the molecule, the successful application of our approach

substantiates the validity of the rotational band model.
Whereas the comparison of the rotational band model approximation to experimental results verifies a theory that was developed specifically for magnetic molecules, this class of materials can serve as an example for studying general questions of quantum mechanics, as well.
Since chemistry now allows the preparation of magnetic molecules with various spin quantum numbers, this class of materials can also be utilized for studying the relations between classical and quantum regime. Due to the correspondence principle, a quantum spin system can be described exactly by classical physics for $s \to \infty$. However, the question remains for which quantum numbers s a classical calculation yields a reasonable approximation. Classical Monte Carlo has been used to study the properties of several magnetic systems [10], and the numerical data has been successfully verified by experiments. The general assumption is that, for high temperatures, the classical model can accurately predict the thermodynamic properties, and that with growing spin quantum number, the range of applicability extends to lower temperatures, since the system approaches the classical limit.
However, the argument for the allowed temperature range, where the quantum system essentially behaves as a classical system, is often derived from the comparison with the experiment, rather than from the analysis of the quantum Hamiltonian.
Our approach in this work is to develop a converging scheme that adds systematic quantum corrections to the classical density of states. To this end, we will first introduce the classical density of states in chapter 3 by giving a general definition and relating it to statistical thermodynamics. We will give an exact solution for Heisenberg spin rings, derived from an expression for the partition function. Furthermore, we will discuss the two stochastic algorithms of classical Monte Carlo and Wang-Landau sampling. Whereas Monte Carlo is mainly used as a reference method for thermodynamic quantities, Wang-Landau sampling is able to give a numerical approximation of the density of states itself.
The classical density of states is determined by the phase space volume of an energy shell, i.e. all phase space points whose corresponding energies lie within a given energy interval. The definition of the quantum spectrum is rather different, since it is derived from the discrete set of energy eigenvalues [15]. Nevertheless, we will implement a formalism that connects quantum and classical spectrum. The correspondence of the two differently defined quantities relies on special quantum states that span the Hilbert space and are parametrized by continuous variables. The main requirement for these states is, however, that the expectation value of the quantum Hamiltonian equals the value of the classical Hamiltonian function for the given parameters. For the Heisenberg model this correspondence is satisfied by the spin-coherent states.
The main goal of the work presented in chapters 3 and 4 is to derive a controllable, converging algorithm that approximates the quantum spectrum of a general Heisenberg spin system. The availability of such a method is eminently valuable, since

other approaches such as classical Monte Carlo rely on empirical arguments whether the system is in the classical domain or not. Furthermore, our algorithm allows the analysis of how the classical limit is approached, which gives general criteria for the similarity of the classical density of states to the quantum spectrum.

2 Quantum mechanical eigenvalue spectrum

This chapter deals with aspects of the quantum mechanical energy spectrum of spin systems. We will first introduce the Heisenberg Hamiltonian, which is used throughout this thesis. The spectrum is then related to thermodynamical properties of the system. The main focus of the chapter is on approximate methods to describe the spectrum. After reviewing the eigenvalue problem and discussing aspects of exact diagonalization, we will give brief summaries of two simplifications of the spectrum. The rotational band model is presented more thoroughly, since it will be used to explain results of neutron scattering experiments later.

2.1 Heisenberg model

In the work presented here, we will solely use the Heisenberg model to describe magnetic interactions between the localized magnetic moments of the molecules. The Heisenberg model introduces an effective Hamiltonian, describing the electrostatic interactions between the electrons as a coupling of the spins of the ions. The magnetic exchange interactions between two spins of the system are assumed to be scalar products of the spin angular momentum operators, multiplied by the exchange parameter J:

$$\hat{H}_{12} = J\,\hat{\mathbf{s}}_1 \cdot \hat{\mathbf{s}}_2 \ . \tag{2.1}$$

For a magnetic molecule, the Heisenberg Hamiltonian for the whole system is written as the sum over all interacting pairs,

$$\hat{H} = \sum_{i<j} J_{ij}\,\hat{\mathbf{s}}_i \cdot \hat{\mathbf{s}}_j \ , \tag{2.2}$$

where J_{ij} denotes the interaction matrix, containing the exchange parameters of pairs (i, j). The sign of the exchange parameter determines the type of interaction, i.e. $J_{ij} > 0$ denotes antiferromagnetic exchange, and $J_{ij} < 0$ denotes ferromagnetic exchange. This is easily deduced from eq.(2.2), when the spin operators are replaced by classical vectors. Positive J then favors anti-parallel alignment of the vectors.

2.1.1 Angular momentum operators

The operators $\hat{\mathbf{s}}_i$ in eq.(2.2) are spin angular momentum operators. We will give a brief summary of their properties [16].
The states $|\, s \,\rangle$ are eigenstates of the square of the spin operator $\hat{\mathbf{s}}$:

$$\hat{\mathbf{s}}^2 \,|\, s \,\rangle = s(s+1) \,|\, s \,\rangle \tag{2.3}$$

The components of the vector operator $\hat{\mathbf{s}}$ satisfy the commutation relation

$$\left[\hat{s}^\alpha, \hat{s}^\beta\right] = \mathrm{i}\, \epsilon_{\alpha\beta\gamma}\, \hat{s}^\gamma \quad \text{with} \;\; \alpha, \beta, \gamma \in \{x, y, z\} \;, \tag{2.4}$$

where $\epsilon_{\alpha\beta\gamma}$ denotes the Levi-Civita symbol. All components commute with the square of the spin operator:

$$\left[\hat{\mathbf{s}}^2, \hat{s}^\alpha\right] = 0 \quad \text{with} \;\; \alpha \in \{x, y, z\} \;. \tag{2.5}$$

However, the components do not commute with each other, and the usual choice for the axis of quantization is the z-axis. We can form a basis of the Hilbert space with eigenstates of the $\hat{s}^z$-operator, denoted by $|\, s, m \,\rangle$:

$$\hat{s}^z \,|\, s, m \,\rangle = m \,|\, s, m \,\rangle \;. \tag{2.6}$$

The quantum number m can take values $m = -s, -s+1, \ldots, s$ (the dimension of the Hilbert space is $2s+1$), and the states are connected with the ladder operators

$$\hat{s}^+ \,|\, s, m \,\rangle = \sqrt{s(s+1) - m(m+1)} \;\, |\, s, m+1 \,\rangle \tag{2.7}$$

and

$$\hat{s}^- \,|\, s, m \,\rangle = \left(\hat{s}^+\right)^\dagger \,|\, s, m \,\rangle = \sqrt{s(s+1) - m(m-1)} \;\, |\, s, m-1 \,\rangle \tag{2.8}$$

The ladder operators can be expressed as linear combinations of the x- and y-components of $\hat{\mathbf{s}}$:

$$\hat{s}^+ = \hat{s}^x + \mathrm{i}\hat{s}^y \quad \text{and} \quad \hat{s}^- = \hat{s}^x - \mathrm{i}\hat{s}^y \;, \tag{2.9}$$

Note that we have set the Planck constant $\hbar = 1$ in all definitions. This convention is used throughout this thesis, unless we specifically require $\hbar$, e.g. for the derivation of the classical limit of a quantum mechanical property.

Product states

For a system of N spins, the Hilbert space is the product of the single-spin Hilbert spaces. The basis states can be expressed as product states

$$|\, s_1, m_1, s_2, m_2, \ldots, s_N, m_N \,\rangle := |\, s_1, m_1 \,\rangle \otimes |\, s_2, m_2 \,\rangle \otimes \cdots \otimes |\, s_N, m_N \,\rangle \;. \tag{2.10}$$

The dimension of the product Hilbert space is

$$\dim \mathcal{H} = \prod_{i=1}^{N} (2s_i + 1) \ , \tag{2.11}$$

or in case of a common spin quantum number s,

$$\dim \mathcal{H} = (2s+1)^N \ . \tag{2.12}$$

The total spin operator of the system is the sum of the individual spin operators:

$$\hat{\mathbf{S}} = \sum_{i=1}^{N} \hat{\mathbf{s}}_i \ . \tag{2.13}$$

However, the product states of the form (2.10) are not eigenstates of $\hat{\mathbf{S}}^2$, but of the z-component of the total spin

$$\hat{S}^z = \sum_{i=1}^{N} \hat{s}_i^z \ , \tag{2.14}$$

with

$$\hat{S}^z \, | \, s_1, m_1, s_2, m_2, \ldots, s_N, m_N \, \rangle \\ = \left(\sum_{i=1}^{n} m_i \right) \, | \, s_1, m_1, s_2, m_2, \ldots, s_N, m_N \, \rangle \ , \tag{2.15}$$

where $\sum_{i=1}^{n} m_i$ is referred to as the quantum number M.

2.1.2 Magnetic field

Eq.(2.2) only describes the mutual interactions of the spins of the molecule. Being magnetic moments, the spins naturally interact with an external field, as well. The Zeeman Hamiltonian describes the interaction of a magnetic moment with an external magnetic field $\mathbf{B}$:

$$\hat{H}_{\text{Zeeman}} = -g\mu_{\text{B}} \mathbf{B} \cdot \hat{\mathbf{S}} \ , \tag{2.16}$$

where the magnetic moment is proportional to the total spin $\hat{\mathbf{S}}$ of the system with the Landé factor $g = 2$ and the Bohr magneton μ_{B}. Since we assume the isotropic Heisenberg model, we can choose the z-axis as the axis of quantization, and the total Hamiltonian can be written as

$$\hat{H} = \sum_{i<j} J_{ij} \, \hat{\mathbf{s}}_i \cdot \hat{\mathbf{s}}_j - g\mu_{\text{B}} B \hat{S}^z \ , \tag{2.17}$$

where B is the magnetic field in z-direction. Note that the sign of the Zeeman interaction is arbitrary, since the Heisenberg model is symmetric in changing the sign of the total quantum number M. We have chosen the minus sign for compatibility with previous numerical calculations.

2.2 Exact diagonalization

The basis for the calculation of any physical property of the system is given by the eigensystem of the Hamiltonian. In order to obtain the eigenvalues and eigenstates, the equation

$$\hat{H} \,|\, \psi \,\rangle = \lambda \,|\, \psi \,\rangle \tag{2.18}$$

has to be solved.
For the numerical evaluation of the eigensystem, the Hamiltonian has to be expressed by its matrix representation H, i.e. $H_{ij} = \langle\, i \,|\, \hat{H} \,|\, j \,\rangle$, where the states $|\, i \,\rangle$ with $i = 1, 2, \ldots, \dim \mathcal{H}$ form a basis of the Hilbert space. The algorithm then uses matrix operations to find the matrix U that diagonalizes the Hamiltonian H:

$$H_{\mathrm{diag}} = U^{\dagger} H U \tag{2.19}$$

The columns of the matrix U represent the eigenvectors, and H_{diag} is a diagonal matrix containing the eigenvalues (hence the term "diagonalization"). The numerical exact diagonalization results presented here are calculated using the linear algebra package LAPACK [17].
Since the diagonalization is an algorithm that scales with the cube of the dimension of the Hilbert space, it is important to minimize this dimension. If one can find a set of mutually commuting operators, the diagonalization can be performed in subspaces characterized by the quantum numbers related to the chosen operators. For the Heisenberg Hamiltonian, e.g., one can use the total $\hat{S}^z$-operator with the corresponding quantum number M to divide the Hilbert space into mutually orthogonal subspaces $\mathcal{H}(M)$, and perform the diagonalization in each subspace separately. In the case of a ring system, a "shift-operator" T can be defined, which cyclically remaps each spin to its next neighbor position. It commutes with both $\hat{H}$ and $\hat{S}^z$ and can be used to further reduce the dimensions of the matrices to be diagonalized. For molecules of different structures, analogous symmetry operators can often be found.

2.2.1 Thermodynamic averages

The statistical operator describing the canonical ensemble is given by [18]

$$\hat{\rho} = \frac{e^{-\beta \hat{H}}}{\mathrm{Tr}\, e^{-\beta \hat{H}}} \,, \tag{2.20}$$

where the denominator is referred to as the partition function:

$$Z(\beta) = \mathrm{Tr}\, e^{-\beta \hat{H}} = \sum_{\nu} e^{-\beta E_\nu} \,, \tag{2.21}$$

with $\beta = 1/k_{\mathrm{B}}T$ and E_ν the eigenvalues of $\hat{H}$.

Thermodynamic averages are evaluated using the trace over the product of the statistical operator and the respective observable $\hat{A}$:

$$\langle\langle \hat{A} \rangle\rangle = \mathrm{Tr}\left(\hat{\rho}\hat{A}\right) = \frac{1}{Z}\,\mathrm{Tr}\left(e^{-\beta\hat{H}}\hat{A}\right) \ . \tag{2.22}$$

The internal energy is defined as the thermodynamic mean of the Hamiltonian of the system:

$$U(\beta) := \langle\langle \hat{H} \rangle\rangle = \frac{1}{Z(\beta)} \sum_{\nu} E_\nu\, e^{-\beta E_\nu} = -\frac{\partial}{\partial\beta}\ \ln Z(\beta) \ . \tag{2.23}$$

The specific heat can either be expressed as a second order derivative of the partition function, or it can be described by the fluctuations of the Hamiltonian:

$$C(\beta) = \left(\frac{\partial U}{\partial T}\right)_V = k_\mathrm{B}\,\beta^2\ \frac{\partial^2}{\partial\beta^2}\ \ln Z(\beta) \tag{2.24}$$

$$= k_\mathrm{B}\,\beta^2 \left(\langle\langle \hat{H}^2 \rangle\rangle - \langle\langle \hat{H} \rangle\rangle^2\right) \ . \tag{2.25}$$

2.3 Approximation of the quantum mechanical energy spectrum

After discussing the exact diagonalization of the Hamiltonian in the previous section, we will now give examples of approximations of the energy spectrum. These methods will not be used to derive new results, but they will serve as background for discussions in later sections. Although the rotational band model described in section 2.4 certainly is a method for the approximation of the quantum mechanical energy spectrum, it is presented in a separate chapter, since it will be used to explain experimental results in section 2.5

2.3.1 "Binning" of energy eigenvalues

The true spectrum of a Heisenberg system consists of a vast number of different eigenvalues (up to $\dim\mathcal{H}$, if no degeneracies are present). We will now analyze the effect of reducing the number of distinct contributions to the spectrum by summating over the weights of the eigenvalues contained in equally-sized energy intervals (energy bins). The resulting approximated spectrum then consists only of the central energies of the bins and the corresponding summated weights.
Figure 2.1 shows the temperature dependence of the internal energy with applied "binning" of the spectrum compared to the exact result. The approximations with $\Delta E \leq 5J$ can accurately describe the exact dependence except for very low temperatures. Since the curves are qualitatively very similar, the internal energy does not

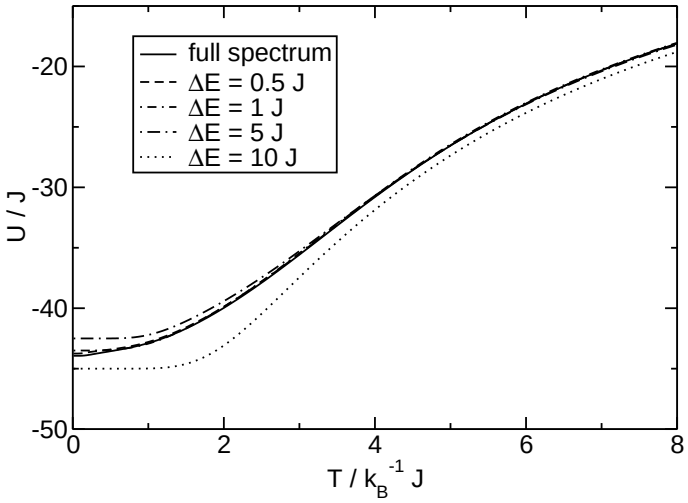

Figure 2.1: Internal energy vs. temperature for the spin ring with $N = 6$, $s = \frac{5}{2}$. The solid line represents the result for the full eigenvalue spectrum; other curves are approximations for "binned" spectra with the given width of the energy bins.

provide us with an adequate tool for the distinction of the quality of the approximations.

Figure 2.2 shows the specific heat for different widths of the energy bins. The main features of the exact curve are reproduced by all "binned" spectra but the ones with $\Delta E \geq 5J$, which significantly differs for the temperature interval that is shown. The other two curves can reproduce the exact one for almost all temperatures. Only for $J^{-1}k_{\mathrm{B}}T < 1$, we can see a deviation from the so-called "Schottky peak"[1] which is determined by the gap between ground state and first excited state ($E_1 - E_0 \approx 0.692J$). This energy difference cannot be reproduced by a binned spectrum with equidistant intervals, unless the width of the bins equals this energy gap (or is a divisor, respectively).

Comparing to the results for the internal energy, we find that the specific heat is more sensitive to the level of approximation of the energy spectrum. It exhibits much stronger visual differentiation between the curves, since it is a second-order derivative of the partition function, whereas the internal energy is of first order. We will therefore use the specific heat as the measure of quality for other approximate methods described in later sections.

[1]The Schottky peak is referred to as the maximum of the specific heat $C(T)$ of a system with two energy levels

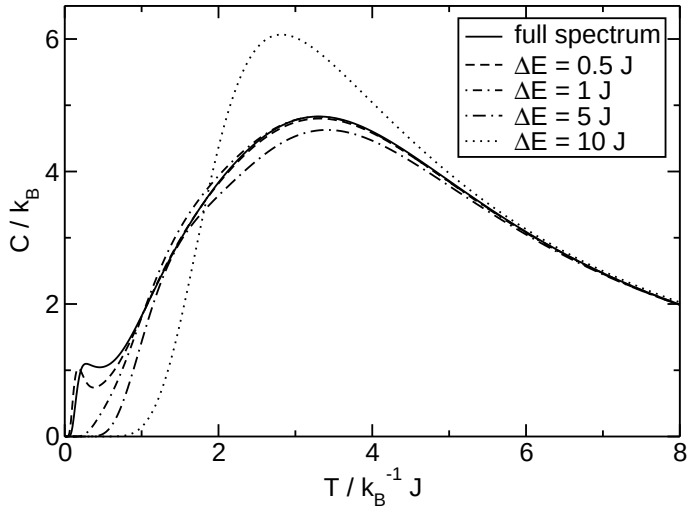

Figure 2.2: Specific heat vs. temperature for the spin ring with $N = 6$, $s = \frac{5}{2}$. The solid line represents the result for the full eigenvalue spectrum; other curves are approximations for "binned" spectra with the given width of the energy bins.

2.3.2 High-temperature expansion of the partition function

The partition function (2.21) can be expressed as a series of traces of powers of $\hat{H}$:

$$Z = \mathrm{Tr}\; e^{-\beta\hat{H}} = \sum_{n=0}^{\infty} \frac{(-1)^n}{n!}\beta^n \;\mathrm{Tr}\,\hat{H}^n \;. \tag{2.26}$$

This can be used to derive a high-temperature (low β) expansion of the internal energy, since the literature lists exact expressions for traces of powers of $\hat{H}$ [19]:

$$\mathrm{Tr}\,\hat{H}^0 = (2s+1)^N = \dim\mathcal{H} \;, \tag{2.27}$$

$$\mathrm{Tr}\,\hat{H}^1 = 0 \;, \tag{2.28}$$

$$\mathrm{Tr}\,\hat{H}^2 = \Big(\sum_{i<j} J_{ij}^2\Big)\frac{1}{3}s^2(s+1)^2(2s+1)^N \;. \tag{2.29}$$

Inserting (2.26) into the definition (2.23) and keeping only first-order terms in β, one obtains

$$U(\beta) \approx -\frac{\mathrm{Tr}\hat{H}^2}{\mathrm{Tr}\hat{H}^0}\,\beta \;. \tag{2.30}$$

Hence, the high-temperature limit of the specific heat can be expressed as

$$C(T) = \frac{\mathrm{Tr}\hat{H}^2}{\mathrm{Tr}\hat{H}^0}\frac{1}{k_\mathrm{B}T^2} \;, \tag{2.31}$$

which becomes

$$C(T) = \frac{N}{3} s^2(s+1)^2 \frac{1}{k_\mathrm{B} T^2} \tag{2.32}$$

for rings with N sites.
The high-temperature limit is equivalently obtained when the energy spectrum is approximated by a Gaussian distribution with the same variance as the Hamiltonian $\hat{H}$.

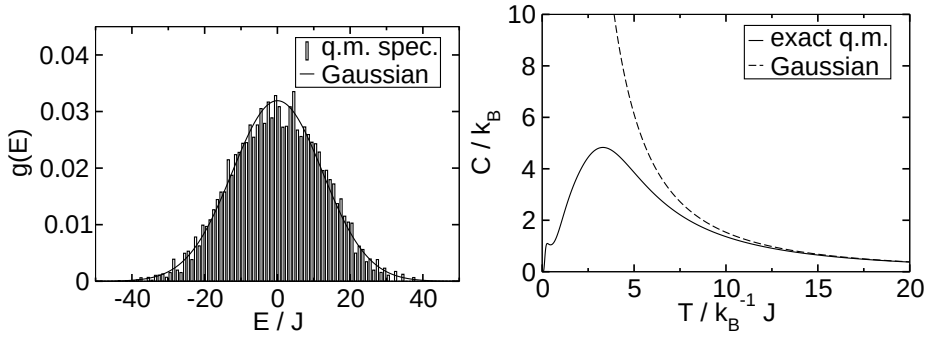

Figure 2.3: Spin ring with $N = 6$,$s = \frac{5}{2}$. Left: histogram of the quantum mechanical energy spectrum (width of bins $\Delta E = 1J$) and approximation with a Gaussian. Right: high-temperature approximation of the specific heat compared to exact quantum mechanical result.

Figure 2.3(left) shows a histogram of the quantum mechanical eigenvalue spectrum of the spin ring with $N = 6$, $s = \frac{5}{2}$. The general shape of the energy distribution is well described by the Gaussian, which has the same variance as the Hamiltonian. The histogram entries add up to a total weight of 1, and the normalization of the Gaussian is chosen so that it matches the histogram.
The graph on the right of figure 2.3 gives a comparison of the high-temperature approximation of the specific heat with the exact result. Since only the second moment of the energy distribution is used, we could not expect any details of the shape of the specific heat to be reproduced by this approximation.

Classical limit of the variance of $\hat{H}$

As mentioned in section 2.1.1, we set $\hbar = 1$ in all equation, unless otherwise noted. When we rewrite eq.(2.29) with $\hbar$, we can calculate the classical limit of the width of the spectrum. The classical limit is approached when $\hbar \to 0$ and $s \to \infty$, so that $\hbar s \to 1$. For the variance of the spectrum, this means that

$$\lim_{\substack{s\to\infty \\ \hbar\to 0}} \frac{\mathrm{Tr}\,\hat{H}^2}{\mathrm{Tr}\,\hat{H}^0} = \lim_{\substack{s\to\infty \\ \hbar\to 0}} \frac{1}{3}\Big(\sum_{i<j} J_{ij}^2\Big)\hbar^4 s^2(s+1)^2 = \frac{1}{3}\Big(\sum_{i<j} J_{ij}^2\Big)\,. \tag{2.33}$$

The above formula allows us to calculate the variance of the classical density of states analytically, thus providing a tool for the verification of numerical Wang-Landau results (cf. Sec. 3.5).

2.4 Rotational band model

The thermodynamic behavior of a quantum system can be described completely, if the full energy spectrum is known. However, the full quantum spectrum is not always accessible. In the case of spin systems, the dimension of the Hilbert space grows exponentially with the number of spins.

On the other hand, the Boltzmann factor $e^{-\frac{E_i}{k_B T}}$ decides how much a given energy eigenstate state $|\,\psi_i\,\rangle$ contributes to the thermodynamic averages. If the temperature is low, only a small number of energy levels is actually occupied and a huge part of the spectrum can be neglected. It is therefore still valuable to develop an approximation that can only describe the low-energy part of the spectrum.

For magnetic molecules of the form of rings with an even number of spins, it was found that the series of minimum energies in subspaces of the total spin $\mathcal{H}(\mathcal{S})$ follow a Landé rule: $(E_{\min}(S) - E_0) \propto S(S+1)$ [20, 21].

These systems are bipartite, i.e. they can be decomposed into two sublattices of spins, with no spin interacting with any other spin of the same sublattice. Classical systems of this kind have a well known ground state referred to as a Néel state. Neighboring spins are aligned anti-parallelly (next-nearest neighbors are parallel). This feature of the classical ground state can be used to construct a quantum mechanical trial state as an approximation of the true ground state. The Néel-like quantum ground state would consist of two spins S_A and S_B, representing each sublattice and assuming their maximum value $S_A = S_B = \frac{Ns}{2}$, which are coupled to a total spin of $S = 0$. The series of all Néel-like quantum states from coupling to the minimum $S = 0$ to the maximum $S = Ns$ leads to a parabolic energy spectrum [22]:

$$E_{\text{Néel}}(S) = 4\,\frac{J}{2N}\left[S(S+1) - 2\,\frac{Ns}{2}\left(\frac{Ns}{2}+1\right)\right] \tag{2.34}$$

The factor 4 fixes the equality of the energy of the Néel-like state with $S = Ns$ and the ground state of the corresponding ferromagnetically coupled system, which has $E = JNs^2$. The term rotational band was introduced for this type of spectrum, because it resembles the spectrum of a rigid rotor.

Eq.(2.34) describes the spectrum of a two-spin system with an interaction strength of $\frac{2J}{N}$, where both spins $\hat{\mathbf{S}}_A$ and $\hat{\mathbf{S}}_B$ have quantum numbers $S_A = S_B = \frac{Ns}{2}$. Thus, an equivalent representation of (2.34) can be given by an effective Hamiltonian [13]

$$\hat{H} = 4\,\frac{J}{2N}\left[\hat{\mathbf{S}}^2 - \hat{\mathbf{S}}_A^2 - \hat{\mathbf{S}}_B^2\right]\ . \tag{2.35}$$

The above equation can be used to derive an approximation of the whole spectrum, because the spins of the sublattices A and B can be allowed to couple to sublattice spin values between $S_A = 0$ and $S_A = \frac{Ns}{2}$ (S_B accordingly). Reference [13] shows that many systems exhibit a second parabolic band above the lowest one (Néel band). In the rotational band model, this first excited band can be described by coupling the two sublattice spins with $S_A = \frac{Ns}{2}$ (maximum) and $S_B = \frac{Ns}{2} - 1$ (maximum decreased by one) to a total spin $S = [1, 2, \ldots, Ns - 1]$. The missing $S = 0$ level also agrees with the exact spectra of bipartite systems. However, higher excitations should not be expected to be described adequately by the rotational band model.
In reference [13] it was also shown that the rotational band model can be extended to rings with an odd number of spins as well as to other structures like octahedra, icosahedra, and rings with next-nearest neighbor interaction. The formula for the series of minimum energy states in subspaces $\mathcal{H}(\mathcal{S})$ has to be modified to match the given structure:

$$E_{\min}(S) \approx E_0 + J\frac{D(N,s)}{2N}S(S+1)\ . \tag{2.36}$$

The spin- and size-dependent parameter $D(N, s)$ describes the curvature of the parabola, whereas E_0 is the ground state energy. These parameters were adjusted so that eq.(2.36) reproduces the ground state energies of both the antiferromagnetic and the ferromagnetic case. It was found that eq.(2.36) then showed good numerical agreement to the minimum energies of the $\mathcal{H}(\mathcal{S})$ subspaces of the full Heisenberg Hamiltonian.

2.4.1 Application to $\{\mathbf{Mo_{72}Fe_{30}}\}$

Since the number of states in $\{Mo_{72}Fe_{30}\}$ is astronomically large ($(2s+1)^N = 6^{30}$, which is about Avogadro's number), we don't have access to the true energy spectrum of this molecule. However, we can establish an approximation of the spectrum using the rotational band model described in the previous section.
The ground state of the corresponding classical Hamiltonian of $\{Mo_{72}Fe_{30}\}$, where the vector spin operators are replaced by classical vectors, can be found analytically. Using graph theory, one can show that the corresponding graph to the interaction matrix J_{ij} in eq.(2.2) is three-colorable. This means each site can be assigned one out of three colors, so that none of the neighboring sites has the same color. Therefore, the ground state structure is composed of three sublattices, each containing ten spins. On each of these sublattices, all spins point to the same direction. The sublattice vectors are coplanar, and the angle between each two of them is 120 degrees [23].
The knowledge of the classical ground state forms the basis for the construction of an approximate quantum Hamiltonian according to the rotational band model. The ten spins on each sublattice first couple to a super-spin, and these three spin operators

$\hat{\mathbf{S}}_1$, $\hat{\mathbf{S}}_2$, and $\hat{\mathbf{S}}_3$ then interact via a Heisenberg Hamiltonian:

$$\begin{aligned}\hat{H}_{\text{rot.band}} &= J\frac{D(N,s)}{N}\left[\hat{\mathbf{S}}_1\cdot\hat{\mathbf{S}}_2+\hat{\mathbf{S}}_2\cdot\hat{\mathbf{S}}_3+\hat{\mathbf{S}}_3\cdot\hat{\mathbf{S}}_1\right]\\ &= J\frac{D(N,s)}{2N}\left[\hat{\mathbf{S}}^2-\hat{\mathbf{S}}_1^2+\hat{\mathbf{S}}_2^2+\hat{\mathbf{S}}_3^2\right]\ .\end{aligned} \tag{2.37}$$

In order to achieve a better approximation of the real spectrum in the form of eq.(2.36), the refined Hamiltonian introduced in reference [24] is used. A parameter γ is introduced, which adjusts the offset determined by the configuration of the sublattice spins, and thereby shifts the ground state energy.

$$\hat{H}_{\text{rot.band}} = J\frac{D(N,s)}{2N}\left[\hat{\mathbf{S}}^2-\gamma\left(\hat{\mathbf{S}}_1^2+\hat{\mathbf{S}}_2^2+\hat{\mathbf{S}}_3^2\right)\right]\ . \tag{2.38}$$

This Hamiltonian can easily be diagonalized, and its energy eigenvalues are

$$E\left(S;S_1,S_2,S_3\right) = J\frac{D(N,s)}{2N}\left[S\left(S+1\right)-\gamma\sum_{k=1}^{3}S_k\left(S_k+1\right)\right]\ . \tag{2.39}$$

This follows from the fact that each sublattice spin operator $\hat{\mathbf{S}}_k$ commutes with the total spin $\hat{\mathbf{S}}^2$ and both the other sublattice spins.
Using the simple model, we can generate an approximate energy spectrum for our molecule. We can independently choose the three sublattice spins in the allowed interval $\left[0,\frac{N}{3}s=25\right]$. We refer to a band as the series of energy levels $E(S;S_1,S_2,S_3)$ we get for a given choice of S_1, S_2, and S_3, when the total spin quantum number S is varied. The energy levels of the lowest band are obtained when all sublattice spin quantum numbers assume their maximum value, $S_k=\frac{N}{3}s=25$.
The parameters $D(N,s)$ and γ can be derived by enforcing the same energy eigenvalue of the ferromagnetic ground state for both the full Heisenberg Hamiltonian and the simplified rotational band model. The ferromagnetic ground state exhibits the maximum total spin $S=Ns$, and the corresponding energy eigenvalue is

$$E = 2Ns^2J = 60\,(\frac{5}{2})^2\,J = 375\,J \tag{2.40}$$

for the full Hamiltonian (2.2). The energy is doubled compared to a ring system of N spins because each spin in $\{Mo_{72}Fe_{30}\}$ has four instead of two neighbors. In the simple model, the parameter $\gamma=1$. Hence, the parameter D has to equal 6, in order eq.(2.39) yields $E=2JNs^2$ for $S=Ns$ and $S_k=\frac{Ns}{3}$ (all sublattice spins S_k assume their maxima and couple to the maximum total spin).
In earlier investigations [25], we have confirmed that the series of lowest energies of the $\mathcal{H}\left(\mathcal{S}\right)$ subspaces indeed show a nearly parabolic dependence on S. Figure 2.4

shows our numerical results for the eigenvalues of the full Heisenberg Hamiltonian using the DMRG algorithm [9, 26], and a fit to the refined rotational band model as in eq.(2.39). The least-squares fitting procedure yields parameters $D = 6.17$ and $\gamma = 1.05$, leading to a good global consistency of both curves.

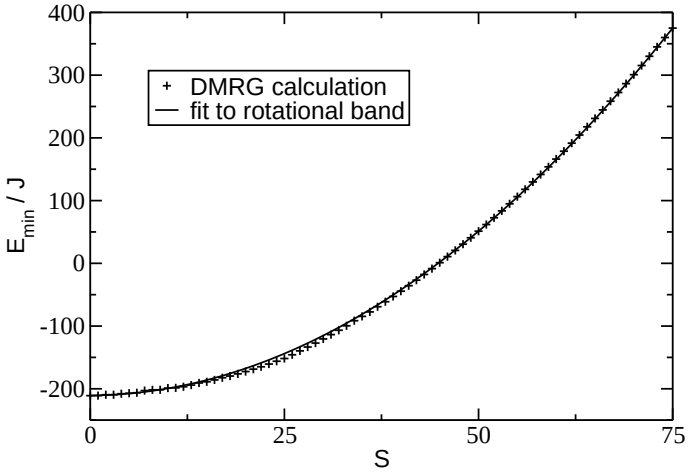

Figure 2.4: DMRG approximations for the lowest energy eigenvalues in subspaces $\mathcal{H}(\mathcal{S})$, and the corresponding fit to the rotational band model

An alternative method to determine the parameters is by comparing to magnetization measurements, resulting in $D = 6.23$ and $\gamma = 1.07$ [24]. The good agreement with the above mentioned values of $D = 6$ and $\gamma = 1$ shows the applicability of this simplified model.

Magnetic field

Adding a Zeeman term (cf. Sec. 2.1.2) for the interaction with a magnetic field, eq.(2.38) becomes

$$\hat{H}_{\text{rot.band}} = J\frac{D(N,s)}{2N}\left(\hat{\mathbf{S}}^2 - \gamma\sum_{k=1}^{3}\hat{\mathbf{S}}_k^2\right) - g\mu_{\text{B}}\,B\hat{S}^z\ . \tag{2.41}$$

Therefore the energy levels are:

$$E\,(S,M) = J\frac{D(N,s)}{2N}\left[S\,(S+1) - \gamma\sum_{k=1}^{3}S_k\,(S_k+1)\right] - g\mu_{\text{B}}\,BM\ . \tag{2.42}$$

Sources for degeneracies of energy levels

Each band generated by eq.(2.36) consists only of $S_{\max} + 1 = S_1 + S_2 + S_3 + 1$ different energy levels ($S = [0, 1, \ldots, S_{\max}]$). However, the dimension of the Hilbert space $(2s+1)^N = 6^{30}$ is retained by the simplified Hamiltonian, and these bands are highly degenerate. The sources for the degeneracies can be classified by four types:

Type a): Coupling paths of sublattice spins

There are different paths to couple the ten spins to the respective sublattice spin S_k. The number of degeneracies can be calculated using the following procedure:
Starting with one spin of quantum number $S_1 = s$ (where the index 1 now denotes the number of spins N, and not the number of the sublattice), the possible total spin when coupled to another spin of the same kind can be $S_2 = [|S_1 - s| = 0, 1, \ldots, S_1 + s = 2s]$. There is only one path to reach each of the possible values of S_2. When another spin s is added, the total spin S_3 of three spins can assume values from 0 ($\frac{1}{2}$ for half-integer s) to $3s$. Now for each possible configuration of S_3, one has to add the degeneracies of all those S_2 configurations that can be coupled with s to the resulting S_3. Coupling S_2 with s to S_3 is possible, if

$$|S_2 - s| \leq S_3 \leq S_2 + s \ . \tag{2.43}$$

The procedure is continued accordingly until the total number of spins is reached (S_{10} in the case of the $\{Mo_{72}Fe_{30}\}$ sublattices).
Another formulation of the above can be given with a recurrence formula. The number of paths leading to a given configuration (S, N) is

$$d_{\mathrm{s}}(S, N+1) = \sum_{S'=|S-s|}^{\min(S+s, Ns)} d_{\mathrm{s}}(S', N)$$
$$\text{with} \quad (N+1)\, s \geq S \geq \begin{cases} 0 & \text{if } 2s\,(N+1) \text{ even} \\ \frac{1}{2} & \text{if } 2s\,(N+1) \text{ odd} \end{cases} \ . \tag{2.44}$$

and trivially,

$$d_{\mathrm{s}}(S, 1) = \begin{cases} 1 & \text{if } S = s \\ 0 & \text{else} \end{cases} \ . \tag{2.45}$$

Table 2.1 illustrates the algorithm for the example of coupling four spins $s = \frac{3}{2}$. In order to find the number of paths leading to $S_4 = 2$, the degeneracy levels of the three-spin system have to be summed from $S_3 = |S_4 - s| = \frac{1}{2}$ to $S_3 = S_4 + s = \frac{7}{2}$. Accordingly, the coupling paths for the sublattice spins (ten spins $s = \frac{5}{2}$) were calculated using a simple computer program implementing eq.(2.44). Table 2.2 only shows the numbers of coupling paths which are interesting for our simulation, since

	S									
N	0	$\frac{1}{2}$	1	$\frac{3}{2}$	2	$\frac{5}{2}$	3	$\frac{7}{2}$	4	$\frac{9}{2}$	...
1				1							
2	1		1		1		1				
3		2		4		3		2		1	...
4					11						
⋮											

Table 2.1: Coupling pyramid for an $s = \frac{3}{2}$ system

only the sublattice spin configurations with large S_k are responsible for the low-lying rotational bands.

	S															
N	0	$\frac{1}{2}$	1	$\frac{3}{2}$	2	$\frac{5}{2}$	3	$\frac{7}{2}$	4	$\frac{9}{2}$	5	...	23	$\frac{47}{2}$	24	$\frac{49}{2}$	25
1						1											
2	1		1		1		1		1		1						
3		2		4		6		5		4	...						
⋮																	
10												...	45		9		1

Table 2.2: Coupling pyramid for a sublattice spin of the rotational band model. Ten spins with $s = \frac{5}{2}$ are coupled to the resulting sublattice spin.

Type b): Permutation of lattice spins

The three sublattice spins S_k contribute symmetrically to the Hamiltonian (2.38). They can therefore be permuted without changing the energy eigenvalue. The number of permutations depends on the configuration of the sublattice spins S_k:

$$d_{\text{perm}}(S_1, S_2, S_3) = \begin{cases} 1 & \text{if } S_1 = S_2 = S_3 \\ \frac{3!}{2!} = 3 & \text{if only two of the } S_k \text{ are equal} \\ 3! = 6 & \text{if the } S_k \text{ are all different} \end{cases} . \tag{2.46}$$

Type c): Coupling paths for total spin

A given set of sublattice spins S_1, S_2 and S_3 can be coupled to the total spin S via different paths. The procedure to calculate the number of these paths is similar to the

one described for type a). Whereas for type a) ten spins of the same quantum number $s = \frac{5}{2}$ were coupled, the S_k can assume different values in the interval $\left[0, \frac{Ns}{3} = 25\right]$. Since we have already calculated the number of permutations of the lattices, we can now choose one sequence for the coupling. At first, S_1 and S_2 are coupled to S_{12}, then the third sublattice spin S_3 is added to S_{12} to obtain the total spin S.
The simple algorithm was implemented using a loop counting from $S_{12} = |S_1 - S_2|$ to $S_{12} = S_1 + S_2$. For every S_{12} that satisfies the condition $|S_{12} - S_3| \leq S \leq S_{12} + S_3$, the counter $d_{\mathrm{S}}(S_1, S_2, S_3)$ is incremented.

Type d): M-degeneracy

In case of no applied magnetic field, the Hamiltonian (2.41) is independent of $\hat{S}^z$. Therefore, each energy level is $d_{\mathrm{M}} = 2S + 1$ times degenerate (quantum number M can assume values from $-S$ to $+S$). This degeneracy is of course lifted when a magnetic field is present.

Product of degeneracies

Thus, the degeneracy for a given eigenstate of the rotational band Hamiltonian, characterized by the total and the three sublattice spin quantum numbers, is given by the product of all types of degeneracies introduced above:

$$\begin{aligned} d(S, S_1, S_2, S_3) = d_{\mathrm{s}}(S_1) \cdot d_{\mathrm{s}}(S_2) \cdot d_{\mathrm{s}}(S_3) & \qquad \text{(type a)} \\ \cdot\, d_{\mathrm{perm}}(S_1, S_2, S_3) & \qquad \text{(type b)} \\ \cdot\, d_{\mathrm{S}}(S_1, S_2, S_3) & \qquad \text{(type c)} \\ \cdot\, d_{\mathrm{M}}(S) & \qquad \text{(type d)} \end{aligned} \tag{2.47}$$

2.4.2 Energy levels and degeneracies of the lowest two bands

The lowest band is formed by coupling the sublattices with equal (maximum) spin $S_1 = S_2 = S_3 = 25$. Therefore, the degeneracy of these energy levels arises only from types c) and d) of the above mentioned sources. The level of degeneracy according to type c) can be calculated using the inequality $|S_{12} - S_3| \leq S \leq |S_{12} + S_3|$, with $S_3 = 25$ and $0 \leq S_{12} \leq 50$. Depending on S, there are two situations. When $S \leq 25$, the right inequality always holds, and only $|S_{12} - 25|$ needs to be evaluated. All configurations $S_{12} = \{25 - S, 25 - S + 1, \ldots, 25 + S\}$ can couple to the given S, leading to a $(2S + 1)$-fold degeneracy.
In the case of $S > 25$, the left inequality is always satisfied. Therefore, only $S_{12} + 25 \leq S$ is to be considered, yielding $S_{12} = \{S - 25, S - 25 + 1, \ldots, 50\}$.

The $\hat{S}^z$ degeneracy type d) is always (2S+1)-fold. This leads to the following formula:

$$d(S,25,25,25) = (2S+1) \cdot \begin{cases} (2S+1) & \text{if } S \leq 25 \\ (76-S) & \text{else} \end{cases} . \tag{2.48}$$

The levels of degeneracy in the first excited band ($S_1 = S_2 = 25$, $S_3 = 24$) also have a component of type a) and type b). In the coupling pyramid for ten spins $s = \frac{5}{2}$ (table 2.2), we find nine paths to couple ten spins with $s = \frac{5}{2}$ to a total $S = 24$. There are three permutations of the lattice spins S_1, S_2, S_3 in this case. The level of degeneracy of type c) can be calculated analogously to the lowest band:

$$d(S,25,25,24) = 3 \cdot 9 \cdot (2S+1) \cdot \begin{cases} (2S+1) & \text{if } S \leq 24 \\ 49 & \text{if } S = 25 \\ (75-S) & \text{if } S \geq 26 \end{cases} . \tag{2.49}$$

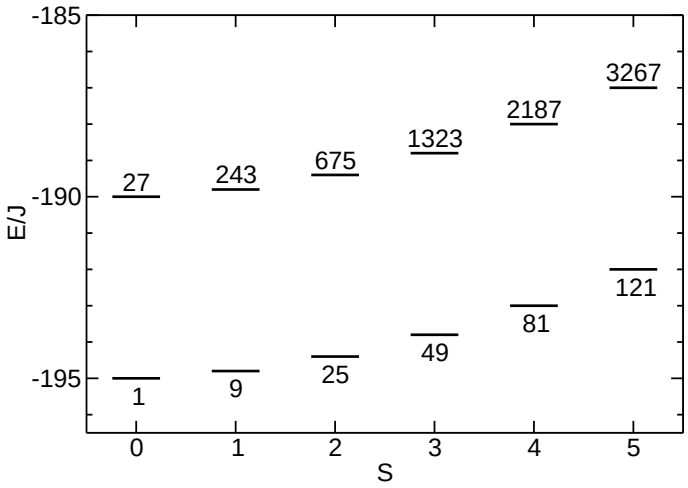

Figure 2.5: Rotational band model for {$Mo_{72}Fe_{30}$}. Numbers next to the energy levels specify the level of degeneracy, with none of the types of degeneracies lifted mentioned in section 2.4.1

Figure 2.5 illustrates the energy levels and the degeneracies for the lowest two bands for small S. The two bands are parallel and are separated by an energy gap of $E^1(S) - E^0(S) = 5\gamma J$ with $\gamma = 1$ for this graph.

2.4.3 Field dependence of the ground state

When the external magnetic field B is raised, the Zeeman energy in eq.(2.42) lifts the $(2S+1)$-fold degeneracies of the $\hat{\mathbf{S}}^2$-eigenstates. Due to the linearity of the Zeeman

energy with the M quantum number, states from multiplets with higher S become ground state with increasing magnetic field.
One can calculate the total spin of the ground state depending on the external magnetic field B. According to eq.(2.42), the minimum energy states ($M = S$) have

$$E\left(S\right) = J\frac{D(N,s)}{2N}\left[S\left(S+1\right) - \gamma\sum_{k=1}^{n_L} S_k\left(S_k+1\right)\right] - g\mu_{\mathrm{B}}\,BS\;. \tag{2.50}$$

Introducing the dimensionless variables

$$B' = \frac{2Ng\mu_{\mathrm{B}}}{DJ}B\;,\quad E' = \frac{2N}{DJ}E\;, \tag{2.51}$$

eq.(2.50) simplifies to

$$E'(S) = S(S+1) - B'S - \text{const}\;. \tag{2.52}$$

The energy difference between two levels $E'(S)$ and $E'(S+1)$ in the same band is

$$E'(S+1) - E'(S) = 2(S+1) - B'\;, \tag{2.53}$$

and therefore, these levels cross at magnetic field strengths of

$$B'_{\text{cross}} = 2(S+1)\;. \tag{2.54}$$

Thus, the spin quantum number of the ground state at the current magnetic field is the largest integer smaller than $B'/2$:

$$S_0(B') = \left\lfloor \frac{B'}{2} \right\rfloor\;. \tag{2.55}$$

2.4.4 Lifting of degeneracies

Due to its simplicity, the rotational band model possesses certain characteristics that are absent for the exact Hamiltonian (2.2). The degeneracies introduced by the simplified Hamiltonian (2.38) are likely to be lifted in this complex structure, i.e. energy levels in this system are presumably not exactly aligned to parabolic bands. Therefore, one might think of the following change to the model. Instead of assuming all levels exactly at the calculated band energy $E(S, S_1, S_2, S_3)$, one could rather group the levels around those energies, with eq.(2.39) only describing the average energy in the respective band.
This broadening of the bands could be described by Gaussian distributions of energy levels centered at the respective band energy. The density of states can then be expressed as

$$\rho(E) \propto e^{-\frac{[E-E(S,S_1,S_2,S_3)]^2}{2\sigma^2}}\;. \tag{2.56}$$

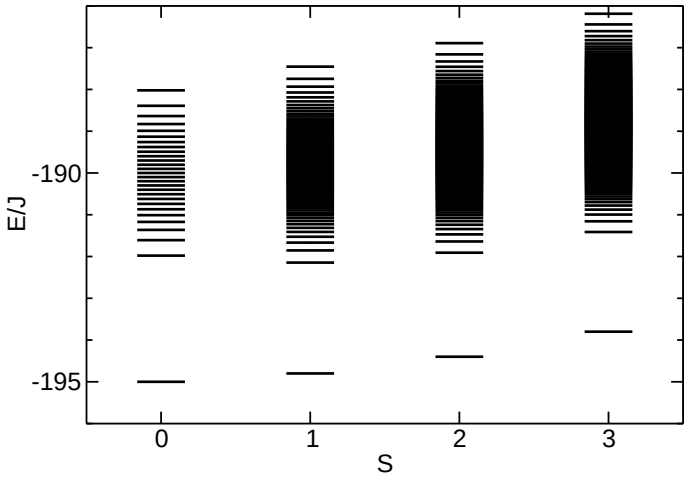

Figure 2.6: Energy levels for $\{Mo_{72}Fe_{30}\}$ with broadened rotational bands. The degeneracies of figure 2.5 are all lifted except for type d) (M-degeneracy). The broadening parameter is $\sigma = 1J$.

The Gaussian has a mean value of $E(S, S_1, S_2, S_3)$ and its variance is specified by σ^2. A distribution with the required Gaussian density can be generated by inverting the integral of the density $\rho(E)$ and applying the resulting function to a uniform distribution [27].

$$E = \Phi^{-1}(x) = \sqrt{2}\,\sigma\,\mathrm{erf}^{-1}\,(1-2x) \quad \text{with} \quad x \in (0,1) \tag{2.57}$$

yields a Gaussian distribution for the energy E with variance σ^2. For an improvement of our approximation, we can now generate energy levels with a broadening parameter σ_{band} using the above formula:

$$E_j(S) = E(S, S_1, S_2, S_3) \; - \; \frac{\sigma_{\mathrm{band}}}{\sigma(n_S)}\,\mathrm{erf}^{-1}\left(1 - 2\frac{j}{n_S+1}\right) \; ; \; j = 1, 2, \ldots, n_S \; . \tag{2.58}$$

erf^{-1} denotes the inverse error function, and n_S is the degeneracy of the respective energy level, excluding the degeneracy arising from the M quantum number:

$$n_S = d_{\mathrm{s}}(S_1) \cdot d_{\mathrm{s}}(S_2) \cdot d_{\mathrm{s}}(S_3) \cdot d_{\mathrm{perm}}(S_1, S_2, S_3) \cdot d_{\mathrm{S}}(S_1, S_2, S_3) \; . \tag{2.59}$$

Eq.(2.57) is strictly valid only for continuous distributions. The variance of a discrete set generated with this formula differs from the desired σ^2 (in the limit of large n this difference vanishes). In order to obtain a distribution of energy levels with variance

σ_{band}, the fraction $\frac{\sigma_{\text{band}}}{\sigma(n_S)}$ is introduced to formula (2.58) with

$$\sigma^2(n_S) = \text{var}\left\{\text{erf}^{-1}\left(1 - 2\frac{j}{n_S+1}\right)\right\}_{j=1,2,\ldots,n_S} \tag{2.60}$$

being the n_S-dependent variance of the generator.
Figure 2.6 shows an example spectrum with broadened bands (broadening parameter $\sigma = 1J$). The band structure is still visible since the density of states is concentrated at the band energies of eq.(2.39), however, the spectrum could be more realistic than the pure rotational band structure with its artificial degeneracies.

2.5 Inelastic neutron scattering on $\{\mathbf{Mo_{72}Fe_{30}}\}$

This chapter deals with the simulation of inelastic neutron scattering (INS) spectra for $\{Mo_{72}Fe_{30}\}$ using the rotational band model. A brief introduction on neutron scattering will be given, both on principal experimental setup and on basic theory. Thereafter, we will outline the relations between properties of the magnetic probe and the cross-section of the scattering process. We will recall the information on the energy spectrum of $\{Mo_{72}Fe_{30}\}$ developed in the previous chapter. The insights gained from the above will then be used to derive a simple method to simulate INS spectra for $\{Mo_{72}Fe_{30}\}$ for given temperatures and external magnetic field strengths. This simulation is then compared to experimental results, and the quality of our method is discussed with respect to these results.

2.5.1 Introduction

Neutrons are baryons and form the basis of atomic nuclei together with the protons. They carry no charge, but a spin of $s_{\text{n}} = \frac{1}{2}$, their mass is $m_{\text{n}} = 1.008665\,\text{u}$. The operator of the magnetic moment for a neutron is

$$\hat{\boldsymbol{\mu}}_{\text{n}} = \gamma_{\text{n}}\mu_{\text{N}}\,\hat{\boldsymbol{\sigma}} \tag{2.61}$$

with $\mu_{\text{N}} = \frac{e\hbar}{2m_{\text{p}}} \approx 5.050 \cdot 10^{-27}\,\text{J}\,\text{T}^{-1}$ being the nuclear magneton and $\gamma_{\text{n}} = -1.91$ the gyromagnetic ratio for neutrons. The operator $\hat{\boldsymbol{\sigma}}$ represents the Pauli spin matrices. According to their kinetic energy, neutrons are classified into groups relating the energy to a temperature scale. The INS experiments on $\{Mo_{72}Fe_{30}\}$ were carried out using cold neutrons ($E \approx 2\,\text{meV} \approx 20\,k_{\text{B}}\text{K}$), i.e. with a substantially lower energy compared to thermal neutrons ($k_{\text{B}} \cdot 300\,\text{K} \approx 25\,\text{meV}$).
Neutrons can be obtained from nuclear reactions such as take place in accelerator collisions or nuclear reactors. Since they have no charge, neutrons cannot be as easily directed or accelerated as protons or electrons.

At the ISIS pulsed neutron source [28], a high-energy beam of protons is directed to a metal target, where the collision process creates neutrons that are emitted in all directions. To achieve coherent **k**-vectors for the scattering experiments, the actual facilities for performing INS experiments are supplied with neutrons via long tubes emerging from the spallation target area.
The interaction between neutrons and matter is relatively weak, and the penetration depth in matter is very large, making neutrons suitable mainly for analyzing bulk properties. Neutron scattering can measure the undistorted properties of the target sample, manifested in the fact the cross-section can be written as a product of two parts, a response function depending only on the target sample, and a function describing the neutron-matter interaction (cf. Sec. 2.5.2). INS experiments are therefore an excellent tool to investigate the nature of the energy spectrum of magnetic molecules.
The basic quantity measured in an INS experiment is the partial differential cross-section

$$\frac{\mathrm{d}\sigma^2}{\mathrm{d}\Omega\,\mathrm{d}E'}\ . \tag{2.62}$$

Given an incident beam of neutron of energy E, it denotes the fraction of neutrons scattered into the element of solid angle $\mathrm{d}\Omega$ around Ω with energies between E' and $E'+\mathrm{d}E'$. In the following paragraph, we will give a short outline of scattering theory necessary to calculate the cross-section from properties of the target material. We mainly reproduce the derivation given in reference [29]:

2.5.2 Outline of scattering theory

At first, an expression for the cross-section of elastic scattering is developed. An incident neutron, described by a plane wave function $\psi_{\mathbf{k}} = \frac{1}{L^{3/2}}\, e^{\mathrm{i}\mathbf{k}\cdot\mathbf{r}}$, is scattered into the plane wave function $\psi_{\mathbf{k}'}$. The probability of state $\psi_{\mathbf{k}}$ changing to $\psi_{\mathbf{k}'}$ can be calculated using Fermi's Golden rule:

$$W_{k\to k'} = \frac{2\pi}{\hbar}\left|\int \mathrm{d}\mathbf{r}\,\psi^*_{\mathbf{k}'}\hat{V}\psi_{\mathbf{k}}\right|^2 \rho_{\mathbf{k}'}(E)\ . \tag{2.63}$$

$\hat{V}$ denotes the interaction potential of the neutron with the target, and $\rho_{\mathbf{k}'}(E)$ the density of final scattering states per energy unit. This result is derived from perturbation theory and is therefore only approximate. However, the scattering of neutrons at the target is a weak process, justifying the assumption the scattering can be described perturbatively.
Enclosing the entire system into an artificial box of volume L^3, normalizing the states $\psi_{\mathbf{k}}$ and $\psi_{\mathbf{k}'}$, and relating the incident flux of neutrons to their velocity, the cross-

section can be expressed as

$$\frac{\mathrm{d}\sigma}{\mathrm{d}\Omega} = \left| \langle\, \mathbf{k}' \,|\, \hat{V} \,|\, \mathbf{k} \,\rangle \right|^2 \ , \tag{2.64}$$

with

$$\langle\, \mathbf{k}' \,|\, \hat{V} \,|\, \mathbf{k} \,\rangle = \frac{L^3 m_\mathrm{n}}{2\pi\hbar^2} \int \mathrm{d}\mathbf{r}\, \psi^*_{\mathbf{k}'} \hat{V} \psi_{\mathbf{k}} \ . \tag{2.65}$$

Eq.(2.64) describes elastic scattering. In order to obtain a formula for inelastic neutron scattering, i.e. scattering incorporating a transfer of energy, the wave functions have to be extended so they include the state $|\,\lambda\,\rangle$ of the target. The incident state of the system then becomes $|\,\mathbf{k}\,\rangle\,|\,\lambda\,\rangle = |\,\mathbf{k}\lambda\,\rangle$.
The cross-section of the scattering process involving a change of the system state $|\,\lambda\,\rangle$ to $|\,\lambda'\,\rangle$ is, according to eq.(2.64),

$$\left(\frac{\mathrm{d}\sigma}{\mathrm{d}\Omega}\right)^{\lambda}_{\lambda'} = \frac{k'}{k} \left| \langle\, \mathbf{k}'\lambda' \,|\, \hat{V} \,|\, \mathbf{k}\lambda \,\rangle \right|^2 \ . \tag{2.66}$$

The fraction $\frac{k'}{k}$ takes into account that the wavelength of the neutron has changed after the scattering process. Since the energy has to be conserved, the energy change of the neutron must equal the change of energy of the sample. The common notation for the energy change of the neutron is $\hbar\omega$, being positive when energy is transferred to the sample:

$$\hbar\omega = E_{\lambda'} - E_\lambda \ . \tag{2.67}$$

Eq.(2.66) can now be transformed to a partial differential cross-section, using a delta function describing the energy conservation:

$$\left(\frac{\mathrm{d}\sigma}{\mathrm{d}\Omega\,\mathrm{d}E'}\right)^{\lambda}_{\lambda'} = \frac{k'}{k} \left| \langle\, \mathbf{k}'\lambda' \,|\, \hat{V} \,|\, \mathbf{k}\lambda \,\rangle \right|^2 \delta\left(\hbar\omega + E_\lambda - E_{\lambda'}\right) \ . \tag{2.68}$$

Since the target has several initial states $|\,\lambda\,\rangle$ and final states $|\,\lambda'\,\rangle$, the cross-sections (2.68) for all combinations λ and λ' have to be added. The transitions in the target system have different weights $p_{\lambda\lambda'}$, consisting of a product of the Boltzmann weight of the initial state $e^{-\frac{E_\lambda}{k_\mathrm{B}T}}$ and degeneracy factors d_λ and $d_{\lambda'}$ of both initial and final state. The normalization is chosen to be $\sum_\lambda p_{\lambda\lambda'} = 1$. Thus, the partial differential cross-section is given by the expression

$$\frac{\mathrm{d}\sigma^2}{\mathrm{d}\Omega\,\mathrm{d}E'} = \frac{k'}{k} \overline{\sum_{\lambda\lambda'} p_{\lambda\lambda'} \left| \langle\, \mathbf{k}'\lambda' \,|\, \hat{V} \,|\, \mathbf{k}\lambda \,\rangle \right|^2 \delta\left(\hbar\omega + E_\lambda - E_{\lambda'}\right)} \ . \tag{2.69}$$

The horizontal bar in the previous formula denotes the average over properties not included in the weights $p_{\lambda\lambda'}$ as e.g. the distribution of isotopes. Furthermore, eq.(2.69)

is independent of the neutron spin. In the next section, we will give the cross-section for magnetic scattering on a spin system. The neutron spin $\hat{\boldsymbol{\sigma}}$ is needed for the derivation of the cross-section, but will be averaged over in the end, and is therefore not included in eq.(2.69).

Magnetic scattering on spin systems

To derive the cross-section for magnetic scattering, one has to replace the operator $\hat{V}$ in eq.(2.69) with the appropriate interaction operator. We assume the magnetic structure of $\{Mo_{72}Fe_{30}\}$ to be describable by localized spins situated at the Fe^{3+} sites of the molecule [30]. Therefore, we will replace $\hat{V}$ with the operator representing the interaction of the magnetic moment of the neutron with the magnetic field generated by the spins. The magnetic field of a dipole with magnetic moment $\boldsymbol{\mu}_\nu$ situated at $\mathbf{r}_\nu$ at a distance $\mathbf{R}_\nu = \mathbf{r} - \mathbf{r}_\nu$ is [31]

$$\mathbf{B} = -\frac{\mu_0}{4\pi}\boldsymbol{\nabla} \times \left(\boldsymbol{\mu}_\nu \times \boldsymbol{\nabla}\frac{1}{|\mathbf{R}_\nu|} \right) . \tag{2.70}$$

Using the correspondence principle, we replace the magnetic moment by the magnetic moment operator of a localized spin $\hat{\boldsymbol{\mu}}_\nu = -g\mu_\mathrm{B}\hat{\mathbf{s}}_\nu$. Therefore, the interaction operator $\hat{V}$ is

$$-\hat{\boldsymbol{\mu}}_n \cdot \mathbf{B} = \frac{\mu_0}{4\pi}\gamma\mu_\mathrm{N} g\mu_\mathrm{B}\, \hat{\boldsymbol{\sigma}} \cdot \left\{ -\boldsymbol{\nabla} \times \left(\hat{\mathbf{s}}_\nu \times \boldsymbol{\nabla}\frac{1}{|\mathbf{R}_\nu|} \right) \right\} , \tag{2.71}$$

and, because the interaction now depends on the neutron spin orientation, the matrix element in eq.(2.69) has to be extended by the neutron spin state $|\,\sigma\,\rangle$:

$$\langle\, \mathbf{k}'\lambda' \,|\, \hat{V} \,|\, \mathbf{k}\lambda \,\rangle \;\rightarrow\; \langle\, \mathbf{k}'\lambda'\sigma' \,|\, -\hat{\boldsymbol{\mu}}_n \cdot \mathbf{B} \,|\, \mathbf{k}\lambda\sigma \,\rangle \tag{2.72}$$

In order to evaluate the previous matrix element, we will first rewrite the expression for the field by inserting the Fourier transform of the potential $\frac{1}{|\mathbf{R}_\nu|}$:

$$\frac{1}{|\mathbf{R}_\nu|} = \frac{1}{2\pi^2}\int \mathrm{d}\mathbf{q}\, \frac{1}{q^2}\, e^{\mathrm{i}\mathbf{q}\,\cdot\,\mathbf{R}_\nu} . \tag{2.73}$$

The magnetic dipole field then becomes

$$\begin{aligned} -\frac{\mu_0}{4\pi}\boldsymbol{\nabla} \times \left(\hat{\mathbf{s}}_\nu \times \boldsymbol{\nabla}\frac{1}{|\mathbf{R}_\nu|} \right) &= -\frac{\mu_0}{4\pi}\frac{1}{2\pi^2}\int \mathrm{d}\mathbf{q}\, \frac{1}{|\mathbf{q}|^2}\, \{\boldsymbol{\nabla} \times (\hat{\mathbf{s}}_\nu \times \boldsymbol{\nabla})\}\; e^{\mathrm{i}\mathbf{q}\,\cdot\,\mathbf{R}_\nu} \\ &= \frac{\mu_0}{4\pi}\frac{1}{2\pi^2}\int \mathrm{d}\mathbf{q}\, \frac{1}{|\mathbf{q}|^2}\, \{\mathbf{q} \times (\hat{\mathbf{s}}_\nu \times \mathbf{q})\}\; e^{\mathrm{i}\mathbf{q}\,\cdot\,\mathbf{R}_\nu} , \end{aligned} \tag{2.74}$$

because $\boldsymbol{\nabla}\, e^{\mathrm{i}\mathbf{q}\cdot\mathbf{R}_\nu} = \mathrm{i}\mathbf{q}\, e^{\mathrm{i}\mathbf{q}\cdot\mathbf{R}_\nu}$. This result enables us to evaluate the $\mathbf{k}$-dependent part of the matrix element:

$$\begin{aligned}
&\langle\, \mathbf{k}' \,|\, -\hat{\boldsymbol{\mu}}_n \cdot \mathbf{B} \,|\, \mathbf{k} \,\rangle \\
&\quad = -\frac{\mu_0}{4\pi}\gamma\mu_\mathrm{N} g\mu_\mathrm{B}\, \frac{L^3 m_\mathrm{n}}{2\pi\hbar^2}\frac{1}{2\pi^2}\int \mathrm{d}\mathbf{r}\, e^{-\mathrm{i}\mathbf{k}'\cdot\mathbf{r}}\, \hat{\boldsymbol{\sigma}}\cdot \int \mathrm{d}\mathbf{q}\, \frac{1}{|\mathbf{q}|^2}\left\{\mathbf{q}\times(\hat{\mathbf{s}}_\nu\times\mathbf{q})\right\} e^{\mathrm{i}\mathbf{q}\cdot\mathbf{R}_\nu}\, e^{\mathrm{i}\mathbf{k}\cdot\mathbf{r}} \\
&\qquad\qquad = -\frac{\mu_0}{4\pi}\gamma\mu_\mathrm{N} g\mu_\mathrm{B}\, \frac{m_\mathrm{n}}{2\pi\hbar^2} 4\pi \frac{1}{|\boldsymbol{\kappa}|^2}\, e^{\mathrm{i}\boldsymbol{\kappa}\cdot\mathbf{r}_\nu}\, \hat{\boldsymbol{\sigma}}\cdot\left\{\boldsymbol{\kappa}\times(\hat{\mathbf{s}}_\nu\times\boldsymbol{\kappa})\right\} \ . \qquad (2.75)
\end{aligned}$$

This follows the fact that the $\mathbf{r}$-integration yields a delta function $\delta\,(\boldsymbol{\kappa}+\mathbf{q})$, with $\boldsymbol{\kappa} = \mathbf{k}-\mathbf{k}'$ being the scattering vector.
When the neutron is scattered at a system of spins, the magnetic field $\mathbf{B}$ is generated by the magnetic moments of all spins:

$$\mathbf{B} = -\frac{\mu_0}{4\pi}\boldsymbol{\nabla}\times\sum_\nu\left(\boldsymbol{\mu}_\nu\times\boldsymbol{\nabla}\frac{1}{|\mathbf{R}_\nu|}\right) \ , \qquad (2.76)$$

so with $\tilde{\boldsymbol{\kappa}} = \frac{\boldsymbol{\kappa}}{|\boldsymbol{\kappa}|}$, eq.(2.75) becomes

$$\begin{aligned}
\langle\, \mathbf{k}' \,|\, -\hat{\boldsymbol{\mu}}_n \cdot \mathbf{B} \,|\, \mathbf{k} \,\rangle &= -r_0\, \hat{\boldsymbol{\sigma}}\cdot\left\{\tilde{\boldsymbol{\kappa}}\times\left(\sum_\nu e^{\mathrm{i}\tilde{\boldsymbol{\kappa}}\,\cdot\,\mathbf{r}_\nu}\hat{\mathbf{s}}_\nu\times\tilde{\boldsymbol{\kappa}}\right)\right\} \\
&= -r_0\, \hat{\boldsymbol{\sigma}}\cdot\hat{\mathbf{Q}}_\perp \ , \qquad (2.77)
\end{aligned}$$

where $\hat{\mathbf{Q}}_\perp$ is defined by the term in curly brackets, and

$$r_0 = \frac{\mu_0 g\gamma\mu_\mathrm{N}\mu_\mathrm{B} m_\mathrm{n}}{2\pi\hbar^2} = -0.54\cdot 10^{-12}\,\mathrm{cm} \ . \qquad (2.78)$$

The magnetic cross-section is the sum over the spin system states $|\,\lambda\,\rangle$ and neutron spin states $|\,\sigma\,\rangle$ (with weights p_σ) of the square of the absolute value of (2.77):

$$\begin{aligned}
\frac{\mathrm{d}^2\sigma}{\mathrm{d}\Omega\,\mathrm{d}E'} &= r_0^2\frac{k'}{k}\sum_{\lambda\lambda'}\sum_{\sigma\sigma'} p_{\lambda\lambda'}p_\sigma \left|\langle\,\lambda'\sigma'\,|\,\hat{\boldsymbol{\sigma}}\cdot\hat{\mathbf{Q}}_\perp\,|\,\lambda\sigma\,\rangle\right|^2 \delta\left(\hbar\omega+E_\lambda-E'_\lambda\right) \\
&= r_0^2\frac{k'}{k}\sum_{\lambda\lambda'}\sum_{\sigma\sigma'} p_{\lambda\lambda'}p_\sigma \langle\,\lambda\sigma\,|\,\left(\hat{\boldsymbol{\sigma}}\cdot\hat{\mathbf{Q}}_\perp\right)^\dagger\,|\,\lambda'\sigma'\,\rangle\langle\,\lambda'\sigma'\,|\,\hat{\boldsymbol{\sigma}}\cdot\hat{\mathbf{Q}}_\perp\,|\,\lambda\sigma\,\rangle \\
&\quad \delta\left(\hbar\omega+E_\lambda-E'_\lambda\right) \qquad (2.79)
\end{aligned}$$

Since we are describing an experiment with unpolarized neutrons, the sum over the neutron spin states is

$$\sum_\sigma p_\sigma\langle\,\sigma\,|\,\hat{\sigma}_\alpha\hat{\sigma}_\beta\,|\,\sigma\,\rangle = \frac{1}{2}\sum_\sigma\langle\,\sigma\,|\,\hat{\mathbb{1}}\delta_{\alpha\beta}+\mathrm{i}\,\epsilon_{\alpha\beta k}\,\hat{\sigma}_k\,|\,\sigma\,\rangle = \delta_{\alpha\beta} \ . \qquad (2.80)$$

Furthermore, The scalar product

$$\hat{\mathbf{Y}}^\dagger \cdot \hat{\mathbf{Y}} = \sum_{\alpha\beta} \left(\delta_{\alpha\beta} - e_\alpha e_\beta\right) \hat{X}^{\dagger\,\alpha} \hat{X}^\beta \tag{2.81}$$

for $\hat{\mathbf{Y}} = \mathbf{e} \times \left(\hat{\mathbf{X}} \times \mathbf{e}\right)$, with $\mathbf{e}$ being an arbitrary unit vector, and $\hat{X}^\alpha$ denoting the α-th component of the vector operator $\hat{\mathbf{X}}$. Using first eq.(2.80) and then (2.81), the cross-section can finally be written as

$$\begin{aligned}
\frac{\mathrm{d}^2\sigma}{\mathrm{d}\Omega\,\mathrm{d}E'} &= r_0^2 \frac{k'}{k} \sum_{\lambda\lambda'} p_{\lambda\lambda'} \langle\, \lambda \,|\, \hat{\mathbf{Q}}_\perp^\dagger \,|\, \lambda' \,\rangle \cdot \langle\, \lambda' \,|\, \hat{\mathbf{Q}}_\perp \,|\, \lambda \,\rangle\, \delta(\hbar\omega + E_\lambda - E'_\lambda) \\
&= r_0^2 \frac{k'}{k} \sum_{\alpha\beta} \left(\delta_{\alpha\beta} - \tilde{\kappa}_\alpha \tilde{\kappa}_\beta\right) \sum_{\lambda\lambda'} p_{\lambda\lambda'} \sum_{\nu\nu'} e^{\mathrm{i}\tilde{\boldsymbol{\kappa}} \cdot (\mathbf{r}_{\nu'} - \mathbf{r}_\nu)} \\
&\quad \cdot \langle\, \lambda \,|\, \hat{s}_\nu^\alpha \,|\, \lambda' \,\rangle \langle\, \lambda' \,|\, \hat{s}_{\nu'}^\beta \,|\, \lambda \,\rangle\, \delta(\hbar\omega + E_\lambda - E'_\lambda)\ .
\end{aligned} \tag{2.82}$$

As mentioned in the introduction, the cross-section factorizes into an interaction part $r_0^2 \frac{k'}{k}$, and a response function (usually denoted $S(\boldsymbol{\kappa}, \omega)$) that only depends on the properties of the sample. The response function contains matrix elements of unperturbed eigenstates $|\,\lambda\,\rangle$ with the spin operators $\hat{s}_\nu^\alpha$, and the unperturbed eigenenergies appear in the delta function as well as in the Boltzmann factor in the weights $p_{\lambda\lambda'}$. INS experiments are therefore well suited for directly probing the energy spectrum of magnetic systems.
The result (2.82) is based on the assumption of localized magnetic moments generated by the 3d electrons of the Fe^{3+} ions situated at positions $\mathbf{r}_\nu$. A more precise formula would have to include the spin density of these ions (the Fourier transform thereof is the so-called form factor). However, since we do not have access to the eigenfunctions λ of the full Heisenberg Hamiltonian, and the experimental data is already an integral over a range of scattering vectors κ, we use eq.(2.82) only to derive selection rules for the allowed transitions the neutrons can initiate.

Selection rules for allowed transitions

The matrix elements in eq.(2.82) decide whether a transition from a state $|\,\lambda\,\rangle$ to a state $|\,\lambda'\,\rangle$ is allowed or not. We now represent the states $|\,\lambda\,\rangle$ by total S and M, because we will derive selection rules for these quantum numbers:

$$|\,\lambda\,\rangle \rightarrow |\,SM\,\rangle\ . \tag{2.83}$$

Matrix elements of the $\hat{s}^z$ operator can trivially only connect states with the same M:

$$\langle\, SM \,|\, \hat{s}_\nu^z \,|\, S'M' \,\rangle = 0 \quad \text{if} \quad M \neq M'\ , \tag{2.84}$$

and the ladder operators involve a change of the M quantum number by one:

$$\langle SM | \hat{s}_\nu^\pm | S'M' \rangle = 0 \quad \text{if} \quad M \neq M' \pm 1 \,, \tag{2.85}$$

with the relation $s^\pm = s^x \pm \mathrm{i}s^y$.
The Wigner-Eckart theorem [32] states that calculating matrix elements of the form $\langle SM | \hat{s}^\alpha | S'M' \rangle$ is equivalent to coupling a spin with $s = 1$ to the state $|SM\rangle$, based on the tensor nature of the operators $\hat{s}^\alpha$. This leads to the following selection rules for total S:

$$\begin{aligned} & |S - s| \leq S' \leq S + s \quad \text{with} \quad s = 1 \\ \Rightarrow \quad & \langle SM | \hat{s}_\nu^\alpha | S'M' \rangle = 0 \quad \text{if} \quad \begin{cases} |S' - S| > 1 & \text{if} \quad S > 0 \\ S' \neq 1 & \text{if} \quad S = 0 \end{cases} . \end{aligned} \tag{2.86}$$

Combining all three equations, we arrive at the selection rules for S and M. A transition from a state $|SM\rangle$ to a state $|S'M'\rangle$ can only occur, if

$$\Delta S = S' - S = \begin{cases} -1, 0, +1 & \text{if} \quad S > 0 \\ +1 & \text{if} \quad S = 0 \end{cases} , \tag{2.87}$$

and

$$\Delta M = 0, \pm 1 \,. \tag{2.88}$$

2.5.3 Simulation of the INS spectrum

Our goal now is to give an approximation of the INS spectrum based on the rotational band model for the energy spectrum, the formula for the cross-section (2.69), and the selection rules derived in the previous section. Since we do not have access to the eigenstates $|\lambda\rangle$ for $\{Mo_{72}Fe_{30}\}$, we cannot use eq.(2.82) to calculate the cross-section directly. We will rather start from the general form of the cross-section given in (2.69) and use the selection rules to decide which transitions contribute to the INS spectrum. A transition between two levels is only possible if the rules (2.87) and (2.88) are satisfied. For each possible transition there is a corresponding peak in the INS spectrum. The height of this peak is proportional to $p_{\lambda\lambda'}$ and the matrix element for the neutron-scattering-induced transition between the levels, according to eq.(2.68). The weight $p_{\lambda\lambda'}$ is the product of the degeneracies of the two levels and the occupancy (Boltzmann weight) of the starting level. These two quantities can easily be calculated from our model. However, the matrix elements $\langle \lambda | \hat{V} | \lambda' \rangle$ have to be approximated. We assume they are equal to one for all allowed transitions. This is a rather coarse approximation, but it will still allow predictions as to where peaks should appear in the INS spectrum. Nevertheless, predictions about the height of those peaks will be uncertain without having further knowledge about at least the

orders of magnitude of the associated matrix elements. The results obtained from this simulation will have the character of a qualitative description rather than allowing direct fitting to experimental data.
Additionally, we will restrict the simulation to transitions from the lowest rotational band to the first excited band. For magnetic molecules that also exhibit rotational band structures in the low-energy regions of their spectra, it was shown that transitions to higher-energy states have negligible influence on the INS spectrum [33]. We will show later that the experimental INS data for $\{Mo_{72}Fe_{30}\}$ does not indicate that the restriction to the lowest two bands has to be lifted.

Algorithm for the simulation

For our simulation of the INS spectrum, we replace the Dirac delta function in eq.(2.68) for each allowed transition from an initial (E_i) to a final (E_f) energy level by a Lorentzian. Since the experimental data we will discuss later is already integrated over a range of wave vectors, we give a simplified version of the integral of (2.68):

$$\sigma_{i\to f}^{B,T}(E) = d_i\, d_f\, e^{-\frac{E_i}{k_\mathrm{B}T}}\, \frac{\Gamma}{\Gamma^2 + \left[(E_f - E_i) - E\right]^2}\,, \tag{2.89}$$

with d_i and d_f being the degeneracy factors for the respective levels, T the temperature, and Γ a common broadening parameter for all signals. Γ corresponds to the half-width at half-maximum (HWHM) of the Lorentzian. The superscript B, T denotes the dependence of the signal on the temperature and on the applied magnetic field, since the energy eigenvalues of (2.42) are shifted by the Zeeman term.
We have implemented the approximate method described above as a C program. The program has to be provided with a set of parameters: exchange constant J, magnetic field value B, temperature T, width of the Lorentzians Γ, and an optional broadening parameter σ for the rotational band model.
As a first step, the spectrum of energy levels is generated according to the rotational band model, with an optional broadening of the bands. The generation of the spectrum can be omitted, and the spectrum can be imported from another source instead, e.g. an exact diagonalization program. This can be used to simulate neutron scattering on molecules whose Heisenberg Hamiltonian can be treated with numerical exact methods.
After the energy levels have been generated, all transitions between two levels are evaluated in order to find the ones allowed by the following criteria:

- We are interested in the absorption spectrum only, so the energy difference between the final and the initial state of a transition has to be positive

$$E_\mathrm{f} - E_\mathrm{i} \overset{!}{>} 0\,. \tag{2.90}$$

- The selection rules (2.87) and (2.88) have to be satisfied.
- To allow calculation of the scattering spectrum for a large number n of energy levels, we define a temperature dependent cut-off for allowed initial levels. Only transitions initiating from states within $20\,k_\mathrm{B}T$ of the ground state are assumed to contribute to the scattering spectrum:

$$E_\mathrm{i} - E_0 \overset{!}{<} 20\,k_\mathrm{B}T\ , \tag{2.91}$$

  where E_0 is the ground state energy for the given magnetic field. The states that are omitted by this procedure have a Boltzmann weight of less than $2 \cdot 10^{-9}$ relative to the (field dependent) ground state, therefore they can safely be neglected.

  If one would not establish this cut-off, n^2 transitions would have to be evaluated, rendering the approach unfeasible for a large number n of energy levels.

For each transition that satisfies these conditions, a Lorentzian according to eq.(2.89) is added to the simulated spectrum. Thus, the simulated INS spectrum can be expressed as

$$\sigma^{B,T}(E) = \frac{1}{C^{B,T}} \sum_{i,f} \sigma^{B,T}_{i\to f}(E)\ , \tag{2.92}$$

where $C^{B,T}$ is a factor to normalize the total area of the INS spectrum:

$$C^{B,T} = \int \mathrm{d}E \sum_{i,f} \sigma^{B,T}_{i\to f}(E)\ . \tag{2.93}$$

This quantity is proportional to the number of neutrons collected at the detector and can be used to fit the theoretically predicted INS spectrum to experimental results.

Types of transitions

At very low temperatures, the ground state is dominantly populated. We will now describe the transitions originating from the field-dependent ground state, which form the basis of the low-temperature INS spectrum. The derivation is based on the results of section 2.4.3 and the notation used there.
There are six basic types of transitions with different weights according to eq.(2.89). The transition types represent the possible changes of S to $S' = S-1, S, S+1$ with or without a transition to the excited band. Figure 2.7 shows an example situation for a magnetic field of $B' = 5$, which produces a ground state with quantum numbers $S = 2$, $M = 2$. In this case, all six transition types can occur. If $S = 0$, of course types I and IV are impossible.

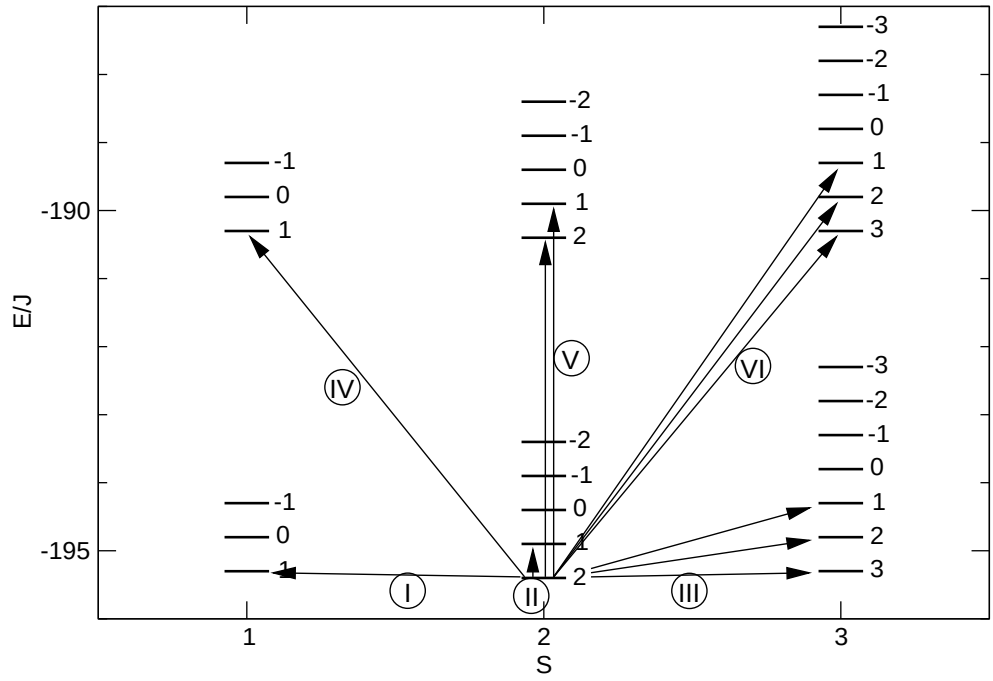

Figure 2.7: Rotational band model for $\{Mo_{72}Fe_{30}\}$. Allowed transition originating from the ground state for $B' = 5$, which has $S = 2$, $M = 2$. Roman numbers describe the type of transition, Arabic numbers next to the levels show their M-quantum numbers.

The number of signals generated is three for the types III and VI ($\Delta M = -1, 0, +1$), two for type V ($\Delta M = 0, -1$), and one for types I, II, and IV (only $\Delta M = -1$). The rotational bands are parallel, therefore there is a constant gap $\Delta E_{\text{band}} = 5J$ between states in different bands but with the same quantum numbers S and M. As a simplification, we use the energy formula (2.52) with dimensionless E' and B'. The energy difference when S changes to S' is

$$\Delta E'_S = \begin{cases} -2S & \text{if } S' = S - 1 \\ 0 & \text{if } S' = S \\ 2(S+1) & \text{if } S' = S + 1 \end{cases} . \tag{2.94}$$

A change in the quantum number M leads to an energy transfer of

$$\Delta E'_M = \begin{cases} B & \text{if } M' = M - 1 \\ 0 & \text{if } M' = M \\ -B & \text{if } M' = M + 1 \end{cases} . \tag{2.95}$$

With these equations, we can now describe the dependence of the energy difference of the allowed transitions on the magnetic field. We concentrate on the transitions that involve a change to the excited rotational band. Transitions inside a band lead to relatively small energy differences. Additionally, the excited band is 27 times degenerate compared to no band degeneracy in the lowest band. This leads to a 27 times weaker signal for transitions which remain in the lowest band according to eq.(2.89). In inelastic neutron scattering, one usually gets a very strong signal at low energies, which prevents the analysis of weak peaks in the vicinity of zero energy transfer. This justifies the concentration on the interband transitions (types IV to VI). In the following formulas, we will use the dependence of the ground state spin quantum number S_0 on the field B given in eq.(2.55).

Type IV

$$\begin{aligned} &\Delta S = -1;\ \Delta M = -1 \\ \Rightarrow\ &\Delta E' = \Delta E'_{\text{band}} - 2S_0(B') + B' \\ &= \Delta E'_{\text{band}} - 2\left\lfloor \frac{B'}{2} \right\rfloor + B' \end{aligned} \tag{2.96}$$

Type V

$$\begin{aligned} &\Delta S = 0;\ \Delta M = \begin{cases} -1 \\ 0 \end{cases} \\ \Rightarrow\ &\Delta E' = \Delta E'_{\text{band}} + \begin{cases} B' \\ 0 \end{cases} \end{aligned} \tag{2.97}$$

Type VI

$$\begin{aligned} &\Delta S = +1;\ \Delta M = \begin{cases} -1 \\ 0 \\ +1 \end{cases} \\ \Rightarrow\ &\Delta E' = \Delta E'_{\text{band}} + 2\left[S_0(B') + 1\right] + \begin{cases} B' \\ 0 \\ -B' \end{cases} \\ &= \Delta E'_{\text{band}} + 2 + 2\left\lfloor \frac{B'}{2} \right\rfloor + \begin{cases} B' \\ 0 \\ -B' \end{cases} \end{aligned} \tag{2.98}$$

Figure 2.8 shows the dependence of the three transition types into the excited band. They form three groups, which have characteristic average behaviors: three energy

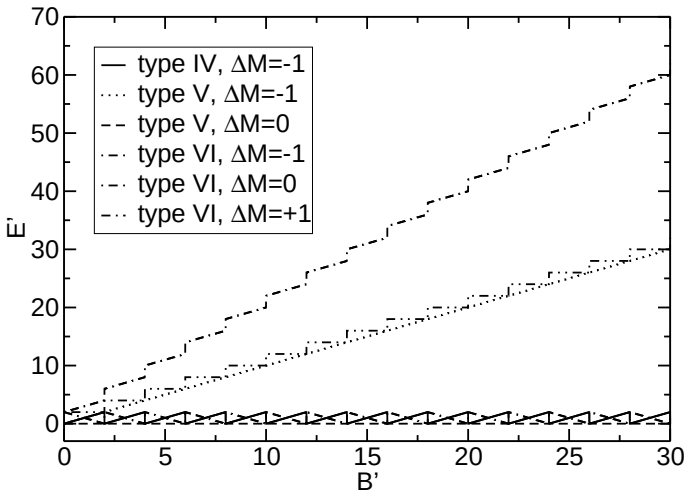

Figure 2.8: Energy transfer for different transition types into excited rotational band depending on the applied magnetic field

transfers are static, two grow proportional to B', and one proportional to $2B'$. This can be derived from eqs.(2.96) to (2.98), when the step function $\left\lfloor \frac{B'}{2} \right\rfloor$ is replaced by the identity $\frac{B'}{2}$.

Therefore, we expect the neutron scattering spectrum for $B = 0$ to consist of one major peak at $\Delta E_{\text{band}} = 5J$, and two satellite peaks emerging from it with increasing magnetic field. One peak's position is expected to be at $\Delta E_{\text{band}} + g\mu_B B$, whereas the second one should be located at $\Delta E_{\text{band}} + 2g\mu_B B$. The relative heights of the peaks are determined by the number of signals added and the level of degeneracy of the final state.

According to eq.(2.49), the ratio of the degeneracies (M-degeneracy lifted) of a level with $S = S_0 - 1$ to the one with $S = S_0$ is

$$\frac{d_{S_0-1}}{d_{S_0}} = \frac{2\,(S_0 - 1) + 1}{2S_0 + 1} = 1 - \frac{2}{2S_0 + 1}\,. \tag{2.99}$$

This corresponds to a transition of type IV. A transition with $\Delta S = +1$ (type VI) has

$$\frac{d_{S_0+1}}{d_{S_0}} = \frac{2\,(S_0 + 1) + 1}{2S_0 + 1} = 1 + \frac{2}{2S_0 + 1}\,. \tag{2.100}$$

The above is only valid as long as $S_0 < 24$. For larger fields, and therefore larger total spin S_0 of the ground state, the ratios can be calculated accordingly: type IV

has

$$\frac{d_{S_0-1}}{d_{S_0}} = \begin{cases} 1 & \text{if} \quad S_0 = 24 \vee S_0 = 25 \\ 1 + \frac{1}{75-S_0} & \text{if} \quad S_0 > 25 \end{cases} , \tag{2.101}$$

and type VI

$$\frac{d_{S_0+1}}{d_{S_0}} = \begin{cases} 1 & \text{if} \quad S_0 = 24 \vee S_0 = 25 \\ 1 - \frac{1}{75-S_0} & \text{if} \quad S_0 > 25 \end{cases} . \tag{2.102}$$

The stationary peak consists of three transitions of types IV, V, and VI. Thus, the height of this peak is

$$h_0 = \frac{k}{d_{S_0}} \left(d_{S_0-1} + d_{S_0} + d_{S_0+1} \right) . \tag{2.103}$$

The peak displaced by $g\mu_B$ has

$$h_1 = \frac{k}{d_{S_0}} \left(d_{S_0} + d_{S_0+1} \right) , \tag{2.104}$$

and the peak with position proportional to $2g\mu_B$

$$h_2 = \frac{k}{d_{S_0}} d_{S_0+1} . \tag{2.105}$$

In the above formulas, k is a factor common to all three types of peaks, containing the Boltzmann weight of the ground state and the levels of degeneracy of the bands.

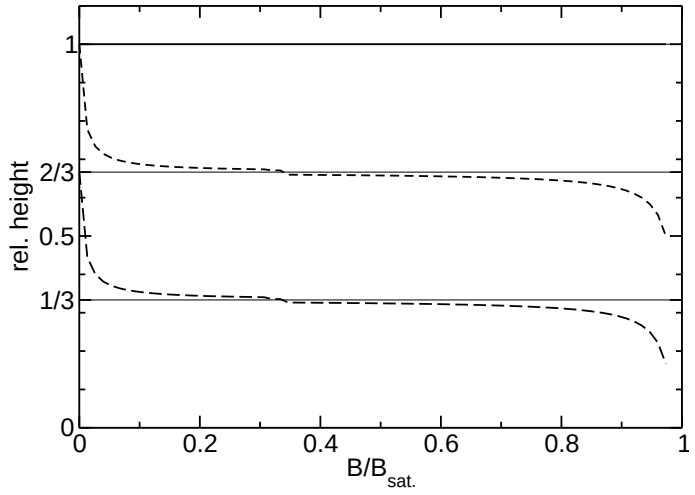

Figure 2.9: Relative height of the three major peaks depending on the applied magnetic field up to saturation ($B_{\text{sat}} \approx 17.4\,\text{T}$). The major static peak is set to a constant height of 1.

The ratio $h_0 : h_1 : h_2$ depends on S_0 and therefore on the applied magnetic field. Figure 2.9 shows the ratio from zero field up to the saturation level. The height of the main peak h_0 is set to 1. The graph indicates one can expect the three peak heights to have an approximate ratio of 3:2:1 for the most part of the region of applied magnetic fields.

2.5.4 Experimental INS data

Recently, several INS experiments were carried out, in order to get more insight into the structure of the spectrum of the magnetic interactions in the molecule $\{Mo_{72}Fe_{30}\}$. The scattering experiments were performed on deuterated samples, i.e. with hydrogen atoms replaced by deuterium, since the incoherent scattering cross-section is much smaller for deuterium. The properties of the deuterated samples were shown to be consistent with the original molecule [30].
The experimental data presented here [34] was obtained at the OSIRIS spectrometer at ISIS [28]. The neutrons had a fixed final energy of 1.845 meV, i.e. cold neutrons were used.
Figure 2.10 shows experimental results for the INS spectrum of $\{Mo_{72}Fe_{30}\}$. The main contribution to the spectrum is located at energy transfers close to $\Delta E = 0$, as can be seen in (b). This strong background is expected to arise from quenched static structural disorder, and therefore is of non-magnetic nature [34]. The background was modeled using the sum of a Gaussian and a Lorentzian. The procedure of extracting the magnetic spectrum from the measured data can be seen in figure 2.10(a), performed at the data for the base temperature $T = 65$ mK. The main graph shows the model for the background fitted to the raw data. The inset contains the background-subtracted data, which is assumed to be the pure magnetic spectrum. Figure 2.10(b) also reveals a problem for the interpretation of the data. The background is actually stronger than the magnetic part of the spectrum. The broad peak of the magnetic spectrum is only represented by a shoulder in the raw data, and the low-energy section is uncertain for the analysis because of the strong signal of the background residing at $\Delta E = 0$.

2.5.5 Comparison of simulation and experiment

Our theoretical model (2.41) suggests the use of J as the unit of energy transfer. It is also common notation to measure the energy in units of K, which means $E[\mathrm{J}] = k_\mathrm{B} E[\mathrm{K}]$ in SI. Since for neutron scattering experiments meV is the most widely used unit, we have to convert our data using

$$1\, k_\mathrm{B}\mathrm{K} = 0.0862\,\mathrm{meV}\ . \tag{2.106}$$

The interaction constant between the spins in $\{Mo_{72}Fe_{30}\}$ was determined in [30] to be $J = 1.57\, k_\mathrm{B}\mathrm{K} = 0.135\,\mathrm{meV}$.

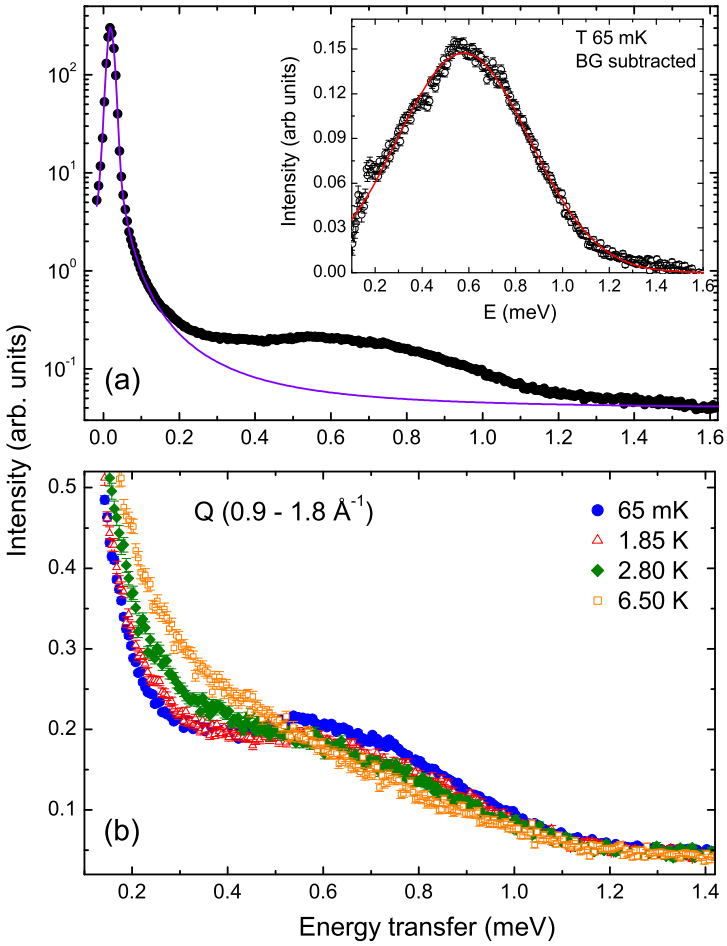

Figure 2.10: (a) Inelastic neutron scattering spectrum at $T = 65\,\mathrm{mK}$. The solid line shows an estimate of the non-magnetic scattering background, the inset gives the spectrum with the background subtracted. (b) shows the raw data for different temperatures. [34]

Our simulation can now be compared to the experimental results. Since the background signal in the measured spectra is stronger than the magnetic contribution, we limit the discussion to a qualitative comparison of theory and experiment. Numerical analysis as direct fitting of our simulation to the data is not justified because of the uncertainties in the gathering of the magnetic part of the spectrum.

Zero-field

Figure 2.11 gives the background-subtracted INS data for different temperatures. At the base temperature, the broad peak is centered at approximately 0.6 meV, with a HWHM (half-width at half-maximum) of about 0.3 meV [34]. With increasing temperature, the low-energy section at about 0.2 meV gains spectral weight, and dominates the spectrum for large temperatures ($T = 6.5\,\mathrm{K}$).
These results are now compared to our simulations. We assume a rotational band structure for the eigenvalue spectrum of $\{Mo_{72}Fe_{30}\}$. Due to the limited accuracy of the experiment, we do not incorporate the refined estimates for D and γ in (2.42), but use the values $D = 6$ and $\gamma = 1$ derived from the constraint for the ferromagnetic ground state energy (2.40). Following from that, the energy gap between the two lowest bands is $5J = 0.676\,\mathrm{meV}$, and an intraband transition $S \to S + 1$ requires $(S + 1) \cdot \frac{J}{5} = (S + 1) \cdot 0.027\,\mathrm{meV}$.
For low temperatures, the ground state is dominantly populated. Thus, we expect two transitions to constitute the INS spectrum: The interband transition with $\Delta E = 5J + \frac{J}{5}$ and the intraband transition with $\Delta E = \frac{J}{5}$, whereas the latter is expected to be much weaker (the degeneracy factor is 27 times smaller).
When the temperature is increased, states of the first excited band become populated, allowing intraband transitions in this band. The degeneracy factor for states in the upper band is 27 times larger than for states in the lowest band (for states with the same S, see Fig. 2.5). Therefore, these intraband transitions will dominate the resulting spectrum with increasing temperature, leading to a prominent peak in the section of low energy transfer.
Following these preliminary remarks, we use our program to generate simulated INS spectra for the same temperatures as in the experiment. We base the simulation on the measurement at the lowest temperature $T = 65\,\mathrm{mK}$, using the HWHM value of 0.3 meV, obtained for the single peak structure, as the parameter Γ in eq.(2.89).
Figure 2.12 shows the simulated INS spectrum for different temperatures. The normalization factors $C^{B,T}$ have been adjusted so the maxima of both experiment and simulation have the same heights. Comparing the experimental and simulated result, we find good qualitative agreement. The spectrum for the lowest temperature $T = 65\,\mathrm{mK}$ yields a single peak, and with increasing temperature, a second signal at lower energies ($\sim 0.2\,\mathrm{meV}$) becomes visible and dominates for $T = 6.5\,\mathrm{K}$.

Magnetic field

Figure 2.13 shows the experimental data of INS on $\{Mo_{72}Fe_{30}\}$ with applied magnetic field of various strengths. It is obvious that the strong background at low energy transfers renders quantitative analysis of the field dependent behavior very difficult. Nevertheless, the curve was fitted to three Lorentzians with a central peak and two

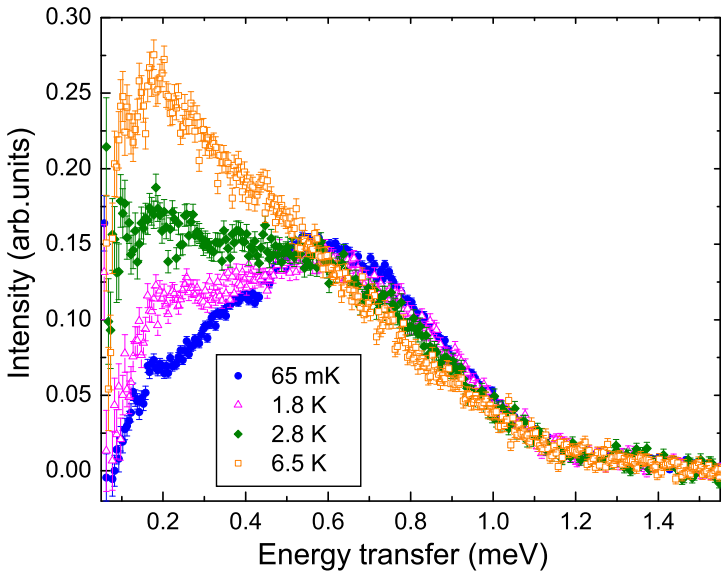

Figure 2.11: INS spectrum of $\{Mo_{72}Fe_{30}\}$ for different temperatures at $B = 0$ [34]. The background has been subtracted as illustrated in figure 2.10

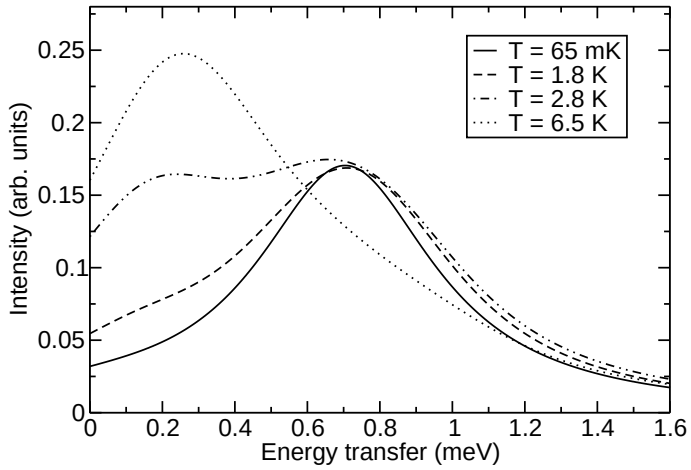

Figure 2.12: Simulated INS spectrum based on the rotational band model, normalization factors set to appropriate values in order to match the proportions of the curves in figure 2.11

sidebands. Whereas the strong background prevented a quantitative description of the field dependence of the lower sideband, a linear behavior could be extracted for the upper sideband. The slope is approximately 0.049 meV/T [34].

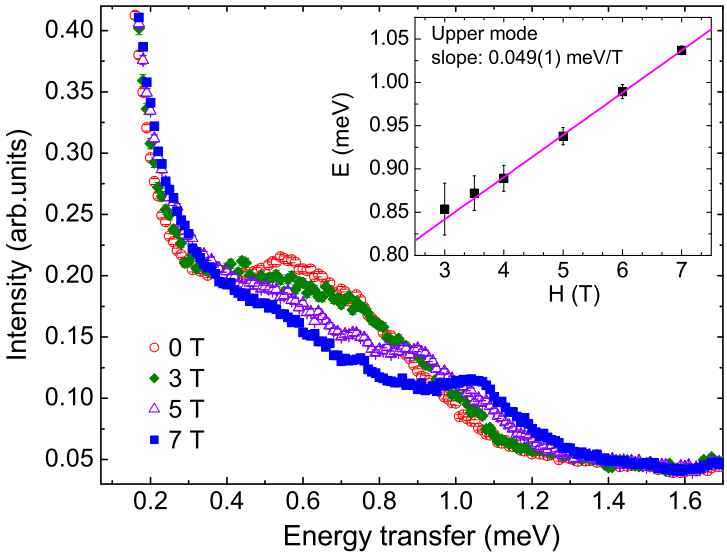

Figure 2.13: Inelastic neutron scattering on $\{Mo_{72}Fe_{30}\}$. Experimental results for different strengths of the applied magnetic field [34]. The inset shows the dependence of the upper sideband on the applied magnetic field.

Again, we use the algorithm described in section 2.5.3 to simulate the INS spectra. However, now the magnetic field is varied at a fixed temperature of $T = 65\,\mathrm{mK}$. We use the same broadening parameter as in the previous section. The result of our simulation is shown in figure 2.14. The normalization factor for these curves was set to retain a constant area of the spectrum (cf. eq.(2.93)). We could not follow the fitting procedure used for the $B = 0$ results, because the background has not been subtracted from the data shown in figure 2.13. This has been omitted in order to directly extract the dependence on the magnetic field shown in the inset.

The simulated spectra show the behavior predicted in section 2.5.3. Two extra peaks emerge from the central peak and move proportional to the applied field, while the displacement of the smaller one is twice as large as for the other one.

This is a clear discrepancy with the behavior extracted from the experiment, where two symmetric sidebands appear at lower and higher energies from the central stationary peak. When we try to fit the slope of the upper sideband extracted from the

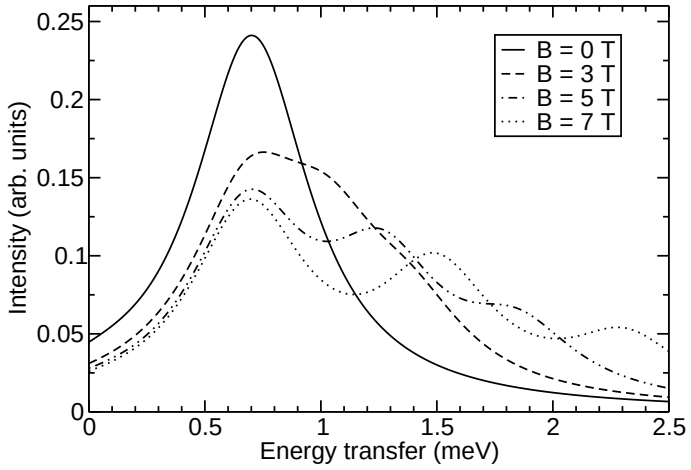

Figure 2.14: Simulated INS spectrum for $\{Mo_{72}Fe_{30}\}$ at $T = 65\,\mathrm{mK}$ for the same strengths of the applied magnetic field as in figure 2.13. Normalization factors are the same for all curves since we cannot compare to background-subtracted experimental results.

experimental data to the theoretical prediction for the first satellite peak, we find

$$0.049\,\frac{\mathrm{meV}}{\mathrm{T}} = g\,\mu_{\mathrm{B}} \quad \Rightarrow \quad g \approx 0.85\,. \tag{2.107}$$

On the other hand, the upper sideband position does not reach zero displacement when extrapolated to $B = 0$. Assuming its source is in the Zeeman interaction of the magnetic field with the spins in $\{Mo_{72}Fe_{30}\}$, the sideband has to disappear when the external field is absent.

2.5.6 Discussion

We will now summarize the results from the previous sections. The aim of the INS spectrum simulation was to verify the applicability of the rotational band model to the complex magnetic molecule $\{Mo_{72}Fe_{30}\}$. The main features we expected to show in the experimental data for low temperatures were a dominant peak at fixed position corresponding to the gap between the lowest two rotational bands, and two peaks emerging from the latter when a magnetic field is present.
We find very good agreement of our simulations with the experimental data in the absence of a magnetic field. Figures 2.11 and 2.12 are qualitatively equivalent. Especially the one-peak structure at low temperatures is a clear indication that the eigenvalue spectrum has a gap as predicted by the rotational band model of about

$5J = 0.68\,\mathrm{meV}$. If there were an enhanced density of states at the band separation of the two lowest bands, corresponding peaks in the low energy region of the INS spectrum should be visible in the experimental data. The fact that only one peak is visible for low temperatures also justifies our restriction to the lowest two bands in our simulation. If transitions to higher energy levels had non-negligible matrix elements with respect to neutron scattering, this should be manifested in additional peaks at higher energy transfers. Assuming the rotational band model to be valid for the second excited band, these energy transfers should be in the region of $\Delta E = 9.8J = 1.32\,\mathrm{meV}$. If these matrix elements were of the same order of magnitude as the ones between the lowest two bands, the corresponding peaks in the INS spectrum would be even larger than the ones visible in the graphs, because the degeneracy factors are much larger for higher bands. The absence of these signals complies with reference [33], which states that transitions to energy levels above the first excited band are negligible.
The broadening of the bands proposed in section 2.4.4 cannot be verified easily with the available experimental data. The structures in the measured spectra do not consist of a series of narrow lines as comparable experiments would suggest (cf. Ref. [35]). The experimental spectra could be simulated equally well with a small width Γ of the Lorentzians in eq.(2.89) and a broadening parameter σ for the first excited rotational bands that yields the same HWHM as in the measured peak (the HWHM of a Gaussian with variance σ is $\sqrt{2\log 2}\,\sigma$). It is hence difficult to tell whether the broad structures arise from the difficult experimental setup or from the energy spectrum of the magnetic molecule.
Despite the striking resemblance of the simulated curve to the experimental data for $T = 6.5\,\mathrm{K}$, the simulated spectrum has to be regarded as speculative for this temperature. At $T = 6.5\,\mathrm{K}$, the first excited band will be strongly populated, and even higher excitations would have to be considered. The simple two-band approach is possibly invalid, because the temperature is already in the range of the energy gap ($5J = 7.85\,k_\mathrm{B}\mathrm{K}$) between the two bands. More rotational bands in the higher-energy spectrum of $\{\mathrm{Mo}_{72}\mathrm{Fe}_{30}\}$ are probably not to be expected. Even for smaller systems, the energy levels above the second excited band fill the spectrum more densely and form a quasi-continuum [33]. Since the rotational band model was developed for the approximation of the low-energy spectrum, it cannot deliver information about the quasi-continuum in the eigenvalue spectrum for higher energies.
In the presence of a magnetic field, simulation and experiment do not agree to a large extend. The simulation predicts two additional peaks at higher energy transfers to appear with an applied field. Their positions relative to the central peak should be equal to $g\mu_\mathrm{B}B$ and $2g\mu_\mathrm{B}B$, respectively. The behavior extracted from the experiment suggests one peak at higher energy transfers, the slope of its relative position being $\sim 1\mu_\mathrm{B}$ with increasing field and an additional offset. This both contradicts the nature of the energy shift introduced by the Zeeman term in the Hamiltonian.

However, the experimental data is uncertain for the $B \neq 0$ measurements. The subtraction procedure for eliminating the background from the scattering data could not be performed, leading to relatively imprecise results, as can be seen in figure 2.13. It is hence impossible to tell whether the model describes the field-dependent behavior improperly, or whether the discrepancy of measurement and simulation arises from inaccurate experimental data. A better spectrometer with a defined background function is being installed at the HMI in Berlin. In contrast to the experimental data presented here, the magnetic scattering data of future measurements could be extracted using a well-defined and also faster-decreasing function describing the background of this spectrometer [36]. This could bring more clarity to the behavior of $\{Mo_{72}Fe_{30}\}$ in the presence of a magnetic field.
Summarizing the results, we can conclude the INS experiments endorse the assumption that the low-energy region of the energy spectrum of $\{Mo_{72}Fe_{30}\}$ can be described by rotational bands. However, the measurements at $B \neq 0$ neither support the model nor do they indicate to which extent the model might have to be modified. The question might be solved by future INS measurements that deliver clearer results. It remains to point out that so far, no other method can adequately explain the low-energy spectrum of $\{Mo_{72}Fe_{30}\}$. Hence the rotational band model remains the most suitable tool for the description of the INS experiments on $\{Mo_{72}Fe_{30}\}$.

3 Classical density of states

After discussing aspects of the quantum mechanical spectrum of spin systems in the previous chapter, we will now switch to a classical description. This chapter deals with the formulation of the classical density of states, its relevance for thermodynamics, and methods to obtain its numerical representation via exact methods as well as with stochastic algorithms.

3.1 Definition and relation to statistical mechanics

The density of states $\rho(E)$ represents the amount of phase space volume per energy unit occupied by states with energies from an infinitesimally small interval centered at energy E. It can be derived from the Hamiltonian function describing the system [37]. We first think of the volume of phase space that contains all states with energies from the interval $[E - \epsilon/2, E + \epsilon/2]$:

$$G(E, \epsilon) = \int \mathrm{d}^{3N}p \, \mathrm{d}^{3N}q \, \Theta\left(\frac{\epsilon}{2} - |E - H(\mathbf{p}, \mathbf{q})|\right) , \tag{3.1}$$

with p and q describing the variables of the N-particle system and Θ denoting the Heaviside step function. Taking the limit $\epsilon \to 0$ of $G(E, \epsilon)/\epsilon$, we obtain the density of states

$$\rho(E) = \int \mathrm{d}^{3N}p \, \mathrm{d}^{3N}q \, \delta(E - H(\mathbf{p}, \mathbf{q})) . \tag{3.2}$$

In the canonical ensemble for systems in thermal equilibrium with a temperature $T = \text{const}$, the partition function is the integral over the Boltzmann weights of all phase space points. Since we have introduced the density of states, we can formulate the partition function as an integral over energy [18]:

$$Z(\beta) = \int_{-\infty}^{\infty} \mathrm{d}E \, \rho(E) \, e^{-\beta E} , \tag{3.3}$$

where $\beta = 1/k_\mathrm{B}T$. In general, the thermodynamic mean of a quantity A, which is given as a function of energy, can be calculated as

$$\langle\langle A \rangle\rangle = \frac{1}{Z} \int_{-\infty}^{\infty} \mathrm{d}E \, \rho(E) \, A(E) \, e^{-\beta E} . \tag{3.4}$$

The internal energy U is the thermodynamic average of the Hamiltonian function and can be expressed as a derivative of the partition function:

$$U(\beta) = \langle\langle H \rangle\rangle = \frac{1}{Z(\beta)} \int_{-\infty}^{\infty} \mathrm{d}E \; \rho(E)\, E \; e^{-\beta E} = -\frac{\partial}{\partial \beta} \; \ln Z(\beta) \; . \tag{3.5}$$

The specific heat measures the differential amount of internal energy gained with a differential increase of temperature:

$$C(\beta) = \left(\frac{\partial U}{\partial T} \right)_V = k_\mathrm{B} \, \beta^2 \, \frac{\partial^2}{\partial \beta^2} \; \ln Z(\beta) \; . \tag{3.6}$$

When the system has a discrete set of energies, the density of states can be written as

$$\rho(E) = \sum_\nu \delta \left(E - E_\nu \right) \; g(E_\nu) \; , \tag{3.7}$$

with weights $g(E)$ representing all states with energy E. The partition function then becomes

$$Z(\beta) = \sum_\nu g(E_\nu)\, e^{-\beta E_\nu} \; , \tag{3.8}$$

and thermodynamic averages are evaluated as follows:

$$\langle\langle A \rangle\rangle = \frac{1}{Z} \sum_\nu g(E_\nu)\, A(E_\nu)\, e^{-\beta E_\nu} \; . \tag{3.9}$$

This description is identical to the one given in section 2.2.1 for quantum systems. One can argue whether there are classical systems with a discrete set of energy states, if one thinks of classical systems as a set of particles described by their continuous positions and momenta. Nevertheless, we will utilize discrete energy states for all numerical data, since we cannot represent continuous functions on a computer. The density of states will have to be described as a set of energies and weight factors $g(E_\nu)$, which represent the integrated density of all states from the interval around the respective energy.

3.2 Classical Heisenberg model

Analogous to the quantum mechanical Hamiltonian for a Heisenberg system, one can give the corresponding classical Hamiltonian function

$$H = \sum_{i<j} J_{ij}^c \; \mathbf{s}_i \cdot \mathbf{s}_j \; , \tag{3.10}$$

where the spin operators are replaced by classical unit vectors $\mathbf{s}_i$. This classical Heisenberg model was introduced mainly to simplify the calculation of quantities such as the specific heat for systems which cannot be treated quantum mechanically. The model has to be applied with care, since it is not obvious where to expect the boundary between classical and quantum (small quantum numbers, low temperatures) regime.
The classical exchange constant J^{c} can be scaled to imitate the quantum mechanical operator (2.2) by

$$J^{\mathrm{c}} = s(s+1)\, J^{\mathrm{qm}} \; . \tag{3.11}$$

This stems from the eigenvalue of the squared spin operator,

$$\hat{\mathbf{s}}^2 \mid s \rangle = s(s+1) \mid s \rangle \; . \tag{3.12}$$

Since the classical model is defined using unit vectors $\mathbf{s}_i$, the factor $s(s+1)$ scales to the maximum quantum mechanical "length" of the product of two spin operators. This scaling, however, is rather arbitrary, one could as well scale with a factor s^2, thereby obtaining equal energy for the fully magnetized state (ferromagnetic ground state). Reference [38] shows that correction terms to the field-dependent ground state of a ferromagnetically coupled chain of spins are smaller, if the scaling factor is chosen to be $s(s+1)$.
Although the factor $s(s+1)$ has been successfully used for the scaling of classical Monte Carlo data (cf. Sec. 3.4), one has to keep in mind the model remains classical. Therefore, the question of general applicability, or the temperature range, for which the classical model can be applied, is still unanswered after the scaling. We will discuss relations between classical and quantum description of a system in chapter 4.
Alternatively to scaling the interaction constant J, instead of using unit vectors, one can choose the length of the spin vectors to be $|\mathbf{s}| = \sqrt{s(s+1)}$. Then the distinction between the two interaction constants becomes unnecessary, i.e. $J^{\mathrm{c}} = J^{\mathrm{qm}}$.
The spin vectors can either be represented in Cartesian, or alternatively in spherical coordinates, which is preferable for many applications. The latter introduces two angles, the zenith $\theta \in [0, \pi]$, and the azimuth $\phi \in [0, 2\pi]$. Using this representation, the spin vector in Cartesian coordinates becomes

$$\frac{\mathbf{s}}{|\mathbf{s}|} = \begin{pmatrix} \cos\phi \, \sin\theta \\ \sin\phi \, \sin\theta \\ \cos\theta \end{pmatrix} \tag{3.13}$$

3.3 Exact solution for Heisenberg spin rings

The direct calculation of the density of states from the Hamiltonian function via the integral definition (3.2) is unfeasible for most systems. However, for special systems,

analytical solutions are available, and we will present an expression for the density of states for a one-dimensional system of N spins.
The derivation will start with the partition function, which according to section 3.1 contains all information needed to determine the thermodynamic properties of the system. Nevertheless, the density of states is the spectrum of the respective system, and we will base a numerical method to approximate the quantum spectrum on the classical density of states in chapter 4. An exact solution, even if limited to a special class of systems, provides us with a tool to verify numerical results. Therefore, it proves valuable to calculate the density of states from the partition function, although the latter can already describe the system's thermodynamic properties.
The partition function of a one-dimensional system of N classical spins with nearest-neighbor interaction and periodic boundary condition (spin ring) is given in reference [39]:

$$Z_N = \lambda_1^N + \lambda_2^N + \dots \ . \tag{3.14}$$

λ_1, λ_2, ... are the eigenvalues of the integral equation

$$\int \mathrm{d}\xi_2 \, e^{-\beta U(\xi_1,\xi_2)} \, \psi_k(\xi_2) = \lambda_k \psi_k(\xi_1) \ , \tag{3.15}$$

where the interaction potential $U(\xi_1, \xi_2)$ between two nearest-neighbor pairs for classical spins is defined as

$$U(\xi_1, \xi_2) = -2J\mathbf{s}_1 \cdot \mathbf{s}_2 \ . \tag{3.16}$$

It is found that the eigenvalues can be written as

$$\lambda_k(K) = \sqrt{\frac{\pi}{2K}} \, I_{k+\frac{1}{2}}(K) \ , \tag{3.17}$$

where I_n denotes the modified Bessel function of the first kind of order n, and $K = 2J\beta$. Each eigenvalue λ_k is (2k+1) times degenerate. Since reference [39] uses the interaction potential (3.16), we have $J = -\frac{1}{2}J^{\mathrm{c}}$ in order to match our definition of the classical Hamiltonian given in (3.10). Thus, we obtain $K = -J^{\mathrm{c}}\beta$, and the partition function (3.14) can be written as

$$Z_N(\beta) = \left(\frac{-\pi}{2J\beta}\right)^{\frac{N}{2}} \sum_{k=0}^{\infty} (2k+1) \left(I_{k+\frac{1}{2}}(-J\beta)\right)^N \tag{3.18}$$

The partition function is the Laplace transform of the density of states. Therefore, we can derive the density of states by inverting this transformation:

$$\rho(E) = \frac{1}{2\pi\mathrm{i}} \int_{c-\mathrm{i}\infty}^{c+\mathrm{i}\infty} e^{E\beta} \, Z(\beta) \, \mathrm{d}\beta \tag{3.19}$$

We choose $c = 0$, $\beta = \mathrm{i}x$. By inserting (3.18) into the equation, we obtain

$$\begin{aligned}
\rho_N(E) &= \frac{1}{2\pi}\int_{-\infty}^{\infty} \mathrm{d}x\; e^{\mathrm{i}Ex} \sum_{k=0}^{\infty}(2k+1)\left(\sqrt{\frac{-\pi}{2J\mathrm{i}x}}\; I_{k+\frac{1}{2}}(-J\mathrm{i}x)\right)^N \\
&= \sum_{k=0}^{\infty}(2k+1)\,\mathcal{F}^{-1}\left\{\left(\sqrt{\frac{\mathrm{i}\pi}{2Jx}}\; I_{k+\frac{1}{2}}(-J\mathrm{i}x)\right)^N\right\} \\
&= \sum_{k=0}^{\infty}(2k+1)\;\mathcal{C}^{N-1}\Bigg\{\underbrace{\mathcal{F}^{-1}\left\{\sqrt{\frac{\mathrm{i}\pi}{2Jx}}\; I_{k+\frac{1}{2}}(-J\mathrm{i}x)\right\}}_{=:\tilde{\rho}_k(E)}\Bigg\}\,, \qquad (3.20)
\end{aligned}$$

where $\mathcal{F}^{-1}$ is the inverse Fourier transform, and $\mathcal{C}^{N-1}$ denotes the $(N-1)$-fold convolution of the term in curly brackets with itself, defined as

$$\mathcal{C}^1\left\{\tilde{\rho}_k(E)\right\} = \tilde{\rho}_k(E) * \tilde{\rho}_k(E) = \int_{-\infty}^{\infty}\mathrm{d}E'\,\tilde{\rho}_k(E')\,\tilde{\rho}_k(E-E') \qquad (3.21)$$

and

$$\mathcal{C}^N\left\{\tilde{\rho}_k(E)\right\} = \mathcal{C}^{N-1}\left\{\tilde{\rho}_k(E)\right\} * \tilde{\rho}_k(E)\;. \qquad (3.22)$$

$\tilde{\rho}_k(E)$ can be rewritten in the following way, where we set $J = 1$ from here on, so both energy and density of states become dimensionless.

$$\begin{aligned}
\tilde{\rho}_k(E) &= \frac{1}{2\pi}\int_{-\infty}^{\infty}\mathrm{d}x\; e^{\mathrm{i}Ex}\sqrt{\frac{\mathrm{i}\pi}{2x}}\; I_{k+\frac{1}{2}}(-\mathrm{i}x) \\
&\quad \text{using}\;\; I_n(x) = (-i)^n J_n(\mathrm{i}x)\,: \\
&= \frac{1}{\sqrt{8\pi}}\,\mathrm{i}^{-k}\int_{-\infty}^{\infty}\mathrm{d}x\; e^{\mathrm{i}Ex}x^{-\frac{1}{2}}J_{k+\frac{1}{2}}(x) \\
&\quad \text{using Abramowitz [40] 11.4.26}\,: \\
&= \frac{1}{2}\;(-1)^k\;\; P_k(-E)\;\Theta(1-E^2) \\
&= \frac{1}{2}\;P_k(E)\;\Theta(1-E^2)\,, \qquad (3.23)
\end{aligned}$$

where P_k is the Legendre polynomial of the k-th order and Θ denotes the Heaviside step function. Thus, the density of states can be written as

$$\rho_N(E) = \lim_{k_{\max}\to\infty}\;\sum_{k=0}^{k_{\max}}\;(2k+1)\;\mathcal{C}^{N-1}\left\{\frac{1}{2}\;P_k(E)\;\Theta(1-E^2)\right\}\;. \qquad (3.24)$$

We have hence arrived at an exact solution for the density of states of a spin ring, derived from an analytical expression for the partition function of this system. Eq.(3.24) is an exact expression, but we cannot give it in closed form, since it would require to calculate the limit $k_{\max} \to \infty$. We will therefore only have access to numerical results.

3.3.1 Numerical treatment

The classical density of states (3.24) can now be calculated numerically for a given system. The sum is only calculated up to a maximum index $k_{\max}$, which will be the control parameter for the numerical accuracy. We use the computer algebra software Mathematica [41] to evaluate the expression (3.24). The contributions to the density of states for an N-spin system,

$$\rho_k^N(E) := \mathcal{C}^{N-1}\left\{\tilde{\rho}_k(E)\right\} \ , \tag{3.25}$$

are calculated independently for the orders k. In order to simplify the calculation of the convolution integrals, we make a case differentiation for the energy E. This allows us to omit the Heaviside step function and evaluate the integrals analytically with Mathematica.
For the given order k, we start with the two-spin density

$$\begin{aligned} \rho_k^2(E) &= \int_{-\infty}^{\infty} \mathrm{d}E'\, \tilde{\rho}_k(E')\, \tilde{\rho}_k(E-E') = \frac{1}{4}\int_a^b \mathrm{d}E'\, P_k(E')P_k(E-E') \\ &\text{with} \quad \{a,b\} = \begin{cases} \{-1, E+1\} & \text{if} \quad -2 \le E \le 0 \\ \{E-1, 1\} & \text{if} \quad 0 < E \le 2 \end{cases} \\ &\text{and} \quad \rho_k^2(E) = 0 \ \text{ for } \ |E| > 2 \ . \end{aligned} \tag{3.26}$$

The two cases stem from the product of the Heaviside functions in $\tilde{\rho}_k(E-E')$, and describe the two regions, where the integrand does not vanish. The expression for the border regions of the three-spin density is analogous to (3.26),

$$\begin{aligned} \rho_k^3(E) &= \frac{1}{2}\int_a^b \mathrm{d}E'\, \rho_k^2(E')\, P_k(E-E') \\ &\text{with} \quad \{a,b\} = \begin{cases} \{-2, E+1\} & \text{if} \quad -3 \le E \le -1 \\ \{E-1, 2\} & \text{if} \quad 1 < E \le 3 \end{cases} \\ &\text{and} \quad \rho_k^3(E) = 0 \ \text{ for } \ |E| > 3 \ . \end{aligned} \tag{3.27}$$

However, we express $\rho_k^3(E)$ in the energy interval $[-1, 1]$ as the sum

$$\rho_k^3(E) = \frac{1}{2}\int_{E-1}^{0} \mathrm{d}E'\, \rho_k^2(E')\, P_k(E-E') + \frac{1}{2}\int_0^{E+1} \mathrm{d}E'\, \rho_k^2(E')\, P_k(E-E') \ , \tag{3.28}$$

so that in each integral, $\rho_k^2(E)$ is evaluated in only one of the cases described in (3.26). Using this notation, we can represent each case of (3.26) as an individual function, thereby simplifying the calculation in Mathematica.
Analogously to the calculation for two and three spins, the procedure is iterated up to the given system size N. Because of the Heaviside function in $\tilde{\rho}_k(E)$, each convolution extends the allowed energy interval symmetrically by one energy unit. Therefore, the density of states of a system with N sites vanishes for energies $|E| > N$. For rings with an even number of spins, we have a ground state energy of $E_0 = -N$ and a maximum energy of $E_{\max} = N$. The fact that the ground state energy E_0 does not equal $-N$, when the system is frustrated, is not a constraint imposed by the convolution of Heaviside functions in this method. However, the summation of the convoluted Legendre polynomials will correctly reproduce the ground state energy E_0, because the resulting $\rho(E)$ also vanishes in the energy interval $[-N, E_0]$.
The energy interval $|-N, N]$ is represented by a discrete set of energies

$$E_\nu = E_0 + \frac{\nu}{n}\left(E_{\max} - E_0\right) = N\left(2\frac{\nu}{n} - 1\right) \ , \tag{3.29}$$

where n is set to the desired resolution. The density of states is calculated at these energies according to

$$\rho_N(E_\nu) = \sum_{k=0}^{k_{\max}} (2k+1)\ \rho_k^N(E_\nu) \ , \tag{3.30}$$

where $\rho_k^N(E_\nu)$ is first evaluated numerically at the energies E_ν, and the numerical values are then summated over k. Alternatively, the $\rho_k^N(E)$ can be summated analytically, resulting in one polynomial for $\rho_N(E_\nu)$ that is defined piecewise, reflecting the respective energy intervals as in (3.26). The analytical summation and evaluation of the resulting polynomial reduced the computer time moderately compared to the direct numerical calculation for each order k. However, it proved numerically unstable in Mathematica, which prohibits further use. We will give numerical results for the two different situations, namely an odd or even number of spins, in the following section.

3.3.2 Spin ring with N=6

As the first example system, we choose the classical spin ring with $N = 6$ sites. Eq.(3.24) is evaluated according to the previous section, and the result is given in figure 3.1.
Reviewing the graph qualitatively, we find a very fast convergence of the approximated density of states on growing $k_{\max}$. The result for $k_{\max} = 10$ can hardly be distinguished from the one for $k_{\max} = 1$. We do not show approximations of higher orders, because they would not deviate from the $k_{\max} = 10$ result for this resolution of the graph.

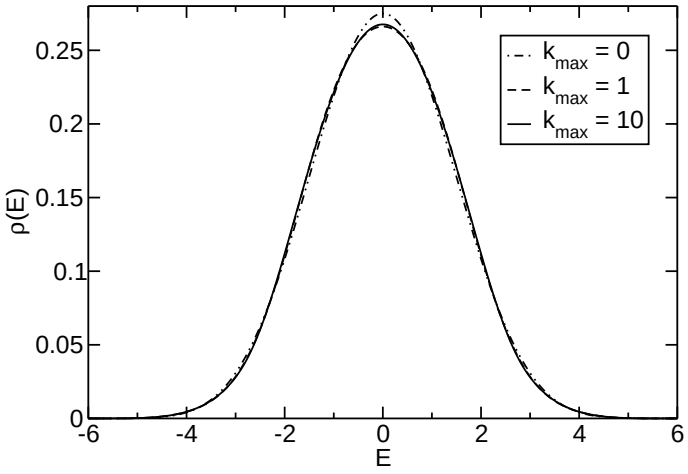

Figure 3.1: Density of states for the classical spin ring with $N = 6$ and $J = 1$. Numerical results derived from eq.(3.24) with given maximum index $k_{\max}$.

From this example, we find that eq.(3.24) is able to deliver precise results for the spin ring with N sites even when only low-order Legendre polynomials are used. However, this is not always the case as we will see when we analyze the results for a different system, namely the trimer, in the following section.

3.3.3 Spin trimer

The density of states for a spin ring with $N = 3$ (equilateral triangle, trimer) can be given analytically in closed form. Reference [42] demonstrates that the partition function, represented by an integral over total spin S rather than energy, is

$$Z = \int_0^3 \mathrm{d}S\, \rho(S)\, e^{-\beta E(S)} \;, \tag{3.31}$$

with

$$\rho(S) = \begin{cases} \frac{S^2}{2} & \text{if} \quad 0 \le S \le 1 \\ \frac{S(3-S)}{4} & \text{if} \quad 1 < S \le 3 \\ 0 & \text{if} \quad S > 3 \end{cases} \;, \tag{3.32}$$

where the total spin $S = |\mathbf{s}_1 + \mathbf{s}_2 + \mathbf{s}_3|$. The energy as a function of S can be expressed as

$$E(S) = \frac{J}{2}\left(S^2 - 3\right) \;. \tag{3.33}$$

Substituting the variable S with the energy E in eq.(3.31), one can identify the energy-dependent density of states as [43]

$$\rho(E) = \begin{cases} \frac{1}{2J}\sqrt{\frac{2E}{J}+3} & \text{if} \quad -\frac{3}{2}J \leq E \leq -J \\ \frac{1}{4J}\left(3-\sqrt{\frac{2E}{J}+3}\right) & \text{if} \quad -J < E \leq 3J \\ 0 & \text{else} \end{cases} \quad . \tag{3.34}$$

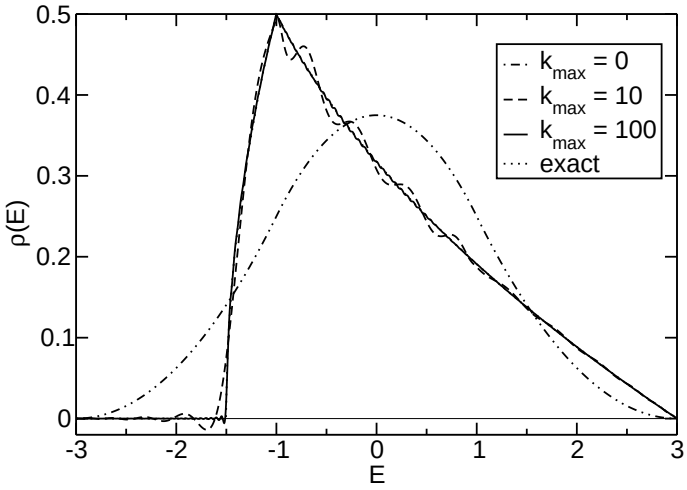

Figure 3.2: Density of states for the classical spin trimer with $J = 1$. Numerical results derived from eq.(3.24) with given maximum index $k_{\max}$ and exact solution from eq.(3.34)

Figure 3.2 shows both numerical results and the exact expression taken from eq.(3.34). The exact curve is almost covered completely by the numerical result for $k_{\max} = 100$, but deviations are visible at the ground state energy $E_0 = -\frac{3}{2}J$. The numerical density of states does not vanish completely in the interval $[E, E_0]$ below the ground state, and it even assumes negative values. This can be explained by the fact that eq.(3.34) is not differentiable at $E = -\frac{3}{2}J$, but is approximated by eq.(3.24) based on polynomials. Furthermore, the ground state $E = -\frac{3}{2}J$ is located inside the first interval of eq.(3.27), so the kink cannot be produced by the case differentiation. Therefore, even for high orders of the approximation ($k_{\max} = 100$), the resulting curve visibly deviates from the exact result.

3.3.4 Comparison of the convergence

From the previous two sections, we have learned that the quality of the approximation using eq.(3.24) depends on the system that is analyzed. Rings with an even number

of spins have a density of states symmetric about the maximum at $E = 0$, whereas for odd-numbered rings the frustration renders $\rho(E)$ more complicated.
In figure 3.3, we give a visualization of the convergence of (3.24) for the two systems, the spin trimer and the ring with six spins. As the measure of convergence, we calculate the mean squared difference between two consecutive approximations with $k_{\max}$ and $k_{\max} - 1$:

$$\begin{aligned} \|\rho_{k_{\max}} - \rho_{k_{\max}-1}\| &:= (E_{\max} - E_0)^{-1} \int_{-\infty}^{\infty} \mathrm{d}E \left[\rho_{k_{\max}}(E) - \rho_{k_{\max}-1}(E)\right]^2 \\ &\approx \frac{1}{n} \sum_{\nu=0}^{n-1}]\rho_{k_{\max}}(E_\nu) - \rho_{k_{\max}-1}(E_\nu)]^2 \ , \end{aligned} \tag{3.35}$$

with $E_\nu = E_0 + \frac{\nu}{n}(E_{\max} - E_0)$ and n the number of points of the discrete energy interval.

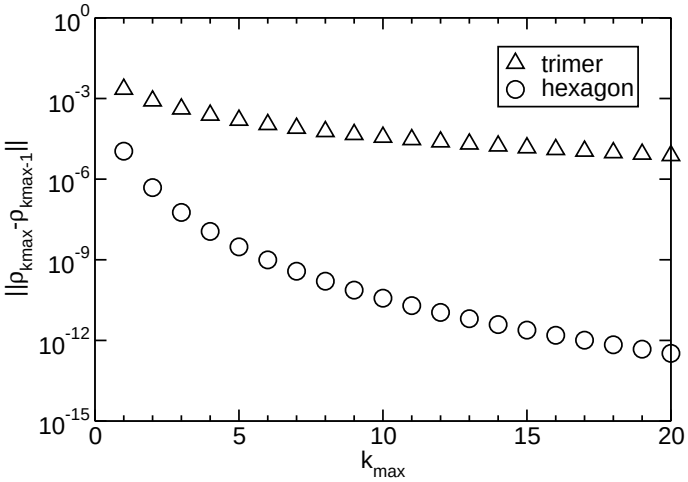

Figure 3.3: Comparison of the convergence of (3.24) for the trimer and the hexagon. The graphs show the logarithm of the average squared differences between the results for $k_{\max}$ and $k_{\max} - 1$ as defined in eq.(3.35)

The difference between two consecutive approximations is orders of magnitude smaller for the hexagon compared to the trimer. As we have already seen qualitatively in figures 3.1 and 3.2, the convergence of the latter is much slower. Eq.(3.35), however, gives a direct numerical measure of the contribution of the order $k_{\max}$ in eq.(3.35) compared to the previous one. Thus, the numerical results shown in figure 3.3 suggest that, generally, the difference between consecutive orders of approximation decreases monotonically.

However, the quality of the approximation does not solely depend on $k_{\max}$. The density of states for the ring of six spins can be precisely calculated with $k_{\max} = 20$, whereas for the same order of the approximation, eq.(3.24) delivers only poor results for the trimer. In order to use the results from eq.(3.24), it is required to check for convergence independently for each system that is analyzed. We will specifically use the results presented in this section for the verification of the Wang-Landau algorithm, which is described in section 3.5. We can prove its applicability to systems with an exactly calculable density of states. Later, the Wang-Landau algorithm will be used to calculate the density of states for systems such as $\{Mo_{72}Fe_{30}\}$, where we cannot apply the scheme presented here.

3.4 Classical Monte Carlo methods

As introduced in section 3.1, the behavior of a system at temperature T is described in the canonical ensemble. In a system with discrete energy levels (denoted by ν), the partition function can be written as

$$Z(\beta) = \sum_{\nu} g(E_\nu)\, e^{-\beta E_\nu} \;, \tag{3.36}$$

and the thermodynamic mean of the quantity A is

$$\langle\langle A \rangle\rangle = \frac{1}{Z} \sum_{\nu} g(E_\nu)\, A(E_\nu)\, e^{-\beta E_\nu} \tag{3.37}$$

However, the direct mathematical evaluation of these quantities is impossible for most systems. Since the number of configurations can be extremely large, the spectral weight $g(E)$ of all states with the same energy E cannot be calculated analytically for an arbitrary system.
If no analytical solution is available, numerical methods have to be applied. The basic idea of stochastic methods is to generate a number of sample configurations and use them to obtain averages for the desired quantities. Since the generation of configurations is based upon the use of random numbers, approaches of this kind are referred to as Monte Carlo methods.
A simple-minded approach to calculate (3.37) would be to generate a number of n independent random configurations. One could calculate the energy E_i and the value of the quantity to be measured, $A_i = A(E_i)$, for each configuration i. Because we are simulating a canonical distribution, the values A_i have to be weighted with the Boltzmann factor, so that the summation over all samples n,

$$\tilde{A} = \frac{1}{n} \sum_{i=1}^{n} A_i\, e^{-E_i/k_{\mathrm{B}}T} \;, \tag{3.38}$$

becomes an approximation of the true thermodynamic mean $\langle\langle A\rangle\rangle$. The degeneracy factors $g(E_i)$ are then included in A_i, because they are proportional to the probabilities of generating the respective configurations i.
However, a purely random generation of configurations will produce many states which do not contribute significantly to the thermodynamic mean, because of their small Boltzmann weight. Especially for low temperatures, only states with low energies have a significant Boltzmann weights, and the probability to generate these states with this simple approach is very small. Thus, generally, this approach will lead to large statistical errors.

3.4.1 Metropolis algorithm

The configurations have to be generated according to their weights in the averaging process, i.e. so-called "importance sampling" has to be used [10]. The most popular method of this class is the Metropolis algorithm [44]. In this algorithm, a sequence of randomly chosen configurations is generated, as well. However, the configurations are not chosen independently. The transition probability from an initial state k to the next state l is made dependent on the energy difference between the two states, and on the temperature of the system. By imposing this scheme, where the transition probability only depends on the properties of the current and the proposed state, a so-called Markov chain is created. Advancing from step t to step $t+1$ can be interpreted as a time evolution, where t is referred to as "Monte Carlo time", since it is not actually a real time.
The dynamics of the Markov process can be described by the master equation

$$\frac{\mathrm{d}P_k(T)}{\mathrm{d}t} = \sum_l P_l(t)\, W_{l\to k} - \sum_l P_k(t)\, W_{k\to l}\ , \tag{3.39}$$

where $P_k(t)$ and $P_l(t)$ are the probabilities for the system to be in states k, or l respectively. $W_{l\to k}$ denotes the transition probability to move from state k to l, and $W_{k\to l}$ describes the opposite direction. The stationary situation (equilibrium) is realized, when

$$P_l\ W_{l\to k} = P_k\, W_{k\to l}\ , \tag{3.40}$$

which is the so-called detailed balance condition. Any transition probability satisfying the detailed balance condition can be used for the generation of the Markov chain. In the canonical ensemble, the probability for the system to be in a state with energy E_i is given by $P_i = \frac{1}{Z} e^{-E_i/k_\mathrm{B}T}$. In the Metropolis algorithm, the following transition probabilities are chosen:

$$W_{k\to l} = \min\left(e^{-\Delta E/k_\mathrm{B}T}, 1\right)\ , \tag{3.41}$$

where $\Delta E = E_l - E_k$.

The algorithm can be summarized in the following way:

1. Start with arbitrary initial state with energy $E_{i=1}$
2. Change the configuration and calculate the energy E_{i+1} of the new state
3. If $E_{i+1} < E_i$, accept the proposed move
4. otherwise, calculate transition probability $p = e^{-\Delta E/k_\mathrm{B}T}$; generate a uniformly distributed random number r from the interval $[0, 1]$; if $r \leq p$, accept move
5. if the move is accepted, calculate value of the variable A_{i+1} (for the new state) and use it for the averaging;
   if the move is rejected, reuse the previous value, i.e. $A_{i+1} = A_i$
6. unless specified number of n samples has been gathered, continue with step 2

The approximation of the thermodynamic mean of the variable A can be calculated afterwards simply as the arithmetic average of the samples A_i,

$$\langle\langle A\rangle\rangle \approx \bar{A} = \frac{1}{n}\sum_{i=1}^{n} A_i \ . \tag{3.42}$$

No weight factors are necessary here, because the states i in the Markov chain were generated according to the Boltzmann distribution. The statistical error of $\bar{A}$ depends of course on the number of samples n. If the samples were generated statistically independent, the error of the mean $\bar{A}$ would just be the standard deviation

$$\text{error} = \frac{\sigma}{\sqrt{n}} \ , \tag{3.43}$$

where the variance σ^2 of the quantity A can be estimated from the samples by

$$\sigma^2 \approx \frac{1}{n-1}\sum_{i=1}^{n} \left(A_i - \bar{A}\right)^2 \ . \tag{3.44}$$

However, the importance sampling scheme introduces correlations between the values of the variable A_i for subsequently generated configurations. The statistical error of $\bar{A}$ is found to be

$$(\text{error})^2 = \frac{\sigma^2}{n}\left(1 + 2\tau_A/\delta t\right) \ , \tag{3.45}$$

where δt is the "time difference" between two consecutive observations A_i and A_{i+1} of the simulated variable A. τ_A is the correlation length, measured in the same units as δt. The correlation time depends on several parameters. It is affected by the Hamiltonian function of the system, by the temperature at which the simulation is

performed, and also by the random number generator (RNG) that is used [10]. We will not go into much detail here, but we will give an example, where despite of the simplicity of the system, τ_A can take large values and thereby lead to "critical slowing down" of the algorithm. In the two-dimensional Ising model, the correlation time can assume large values, when the simulation is performed near the phase transition temperature. The simulation then requires a huge number of samples to achieve the same accuracy as in a temperature region far away from the phase transition. This shortcoming of the method can be partially overcome with the help of advanced methods of generating new configurations (cluster algorithms).

The Metropolis algorithm will be used as a reference for our approximate method presented in chapter 4, and as a verification tool for the Wang-Landau data (cf. Sec. 3.5). We will use it to generate numerical results for the specific heat of the system, so that we can compare the data from this standard method to our new approach.

For the generation of this data, we will use programs from the ALPS project [45] (Algorithms and Libraries for Physics Simulations). The classical Monte Carlo program for Heisenberg systems contained in ALPS is a highly optimized version of the algorithm presented in this section. Because the ALPS implementation makes use of advanced techniques for generating new configurations (cluster updates), the correlation time τ_A is greatly reduced compared to a simple implementation. We therefore prefer the ALPS program to an implementation of our own.

Results

We will only give the results for two ring systems here, because as mentioned above, classical Monte Carlo is not used in this work to produce new data, but only as a reference.

Figure 3.4 shows the specific heat of the two spin rings $N = 6$, $s = \frac{5}{2}$ and $N = 10$, $s = 1$ calculated with classical Monte Carlo compared to the exact quantum mechanical result. The calculation was performed with unit spin length, and the result was scaled to $|\mathbf{s}| = \sqrt{s(s+1)}$. The number of Monte Carlo steps was $5 \cdot 10^7$ for the left and 10^7 for the right graph. Statistical errors are not shown here, since we concentrate on the systematic difference between classical and quantum result, but they are of the order of the linewidth of the curve, except for very low temperatures.

As generally expected, the result for the larger quantum number $s = \frac{5}{2}$ is closer to the exact result than the data for the $s = 1$ system. Whereas the left graph shows good agreement between classical and quantum mechanical result even in the vicinity of the maximum, the classical result in the right graph can only describe the high-temperature region correctly. Naturally, both classical results fail for the low-temperature section and do not vanish for $T = 0$.

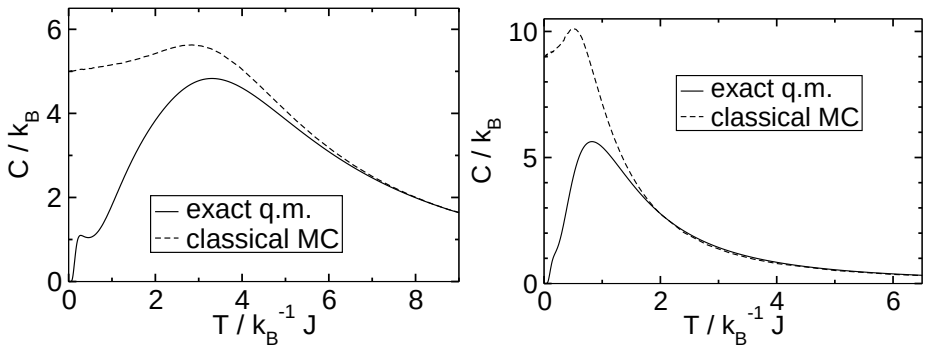

Figure 3.4: Classical Monte Carlo results for the specific heat compared to exact quantum mechanical calculation. Left: ring with $N = 6$, $s = \frac{5}{2}$. Right: ring with $N = 10$, $s = 1$.

3.5 Wang-Landau algorithm

The Wang-Landau algorithm [46] belongs to the class of Monte-Carlo methods, since it is an approximate method and is heavily based on the use of random numbers. It is related to the Metropolis sampling, as it also performs a random walk through energy space. However, the Wang-Landau algorithm directly samples the density of states $g(E)$, rather than the canonical distribution

$$P(E,T) = g(E)\, e^{-\frac{E}{k_B T}} \ , \tag{3.46}$$

as the Metropolis algorithm does. Note that $g(E)$ does not equal the density of states $\rho(E)$ introduced in section 3.1. In contrast to the continuous function $\rho(E)$, $g(E)$ represents the integrated density of all states in the energy interval centered at E:

$$g(E) = \int_{E-\epsilon/2}^{E+\epsilon/2} \mathrm{d}E'\ \rho(E') \ , \tag{3.47}$$

with a common width ϵ of the energy intervals (cf. definition of $G(E,\epsilon)$ in eq.(3.1)). Since $g(E)$ is frequently called density of states in the literature, we will also use this nomenclature here.
Following the presentation of the Wang-Landau algorithm in reference [46], it has been applied successfully to a large variety of problems [47].

3.5.1 Algorithm

The description of the algorithm is mainly based on reference [47]. In order to sample the density of states, the algorithm performs a random walk in energy space.

A simple approach to approximate the density of states would be an unbiased random walk. The state of the system would be changed randomly, and every move would be accepted. The histogram of the energy distribution would be sampled, i.e. the number of visits to each energy bin would be counted. After a long random walk, when every energy bin has been visited, this histogram would converge to the density of states $g(E)$. There is a serious problem with this approach, however. The number of possible configurations is generally a huge number, even for simple systems. The 10x10 square of Ising spins (which can only point up or down) has already $2^{100} \approx 1.27 \cdot 10^{30}$ different configurations. Hence, the probability to randomly generate, e.g., one of the two ground states, is only one out of 2^{99}. An algorithm based on an unbiased random walk is therefore impracticable, since it would require a gigantic number of MC steps to reach every configuration.
The solution to this problem, and key idea of the Wang-Landau algorithm, is the special choice of transition probability for the random walk. In the same way as the Metropolis algorithm does based on the canonical distribution, the Wang-Landau algorithm introduces importance sampling based on the density of states. A proposed change to the configuration of the system state is accepted with a probability proportional to the reciprocal of the density of states. Since the density of states is unknown at the beginning of the algorithm, one starts with an estimate $g(E) = 1$ for all energies (or a better estimate, if available), which is then improved continuously. After each step, the current estimate of $g(E)$ is multiplied by a factor f. During the random walk, also the histogram $h(E)$ is accumulated, i.e. $h(E)$ is increased by one each time the respective energy bin E is visited. Because of the choice of the acceptance probability and the modification of the estimate $g(E)$, the random walk will visit every energy bin E equally frequently (approximately, in the limit of a large number of steps), hence producing a flat histogram.
The modification factor f is changed during the course of the algorithm and has to converge to 1. For $f = 1$, the random walk will produce a flat histogram only for the true density of states $g(E)$.

Technical description

The algorithm is started with a flat density of states $g(E) = 1$. Alternatively, in case more information about the system is available, $g(E)$ can be set to a more suitable estimate. The initial configuration of the system can be chosen arbitrarily. Then a new configuration of the system is proposed, e.g. in a spin system a random spin is picked and changed to a random configuration. The acceptance probability for this move from the state with energy E_1 to the one with E_2 is then

$$W\left(E_1 \to E_2\right) = \min\left(\frac{g(E_1)}{g(E_2)}, 1\right) , \tag{3.48}$$

i.e. if $g(E_2) \leq g(E_1)$, the move to E_2 is always accepted, otherwise the probability of acceptance is $\frac{g(E_1)}{g(E_2)}$. Technically, a random number $r \in [0,1]$ (uniformly distributed) is generated, and if $r \leq \frac{g(E_1)}{g(E_2)}$, the move is accepted. In case of acceptance, the configuration of the system is changed to the proposed one. In any case, $g(E)$ and the histogram $h(E)$ are updated, either at the previous energy of the system or the accepted proposed energy. Every step of the algorithm generates a sample, even if the random walk stays at the same configuration:

$$g(E) \to f \cdot g(E) \tag{3.49}$$

$$h(E) \to h(E) + 1 \; . \tag{3.50}$$

The estimate for $g(E)$ will grow very large due to the multiplication with f every time the bin E is visited. Therefore, it is numerically more adequate to work with the logarithm of $g(E)$ instead. The update then becomes

$$\ln g(E) \to \ln g(E) + \ln f \; , \tag{3.51}$$

and the probability for acceptance

$$W\left(E_1 \to E_2\right) = \min\left(\exp\left[\ln g(E_1) - \ln g(E_2)\right], 1\right) \; . \tag{3.52}$$

The random walk is performed until the histogram is flat. After a given number of MC steps (e.g. 10000), the histogram $h(E)$ is reviewed and is considered flat, if

$$\frac{h(E)}{\bar{h}} \geq x \quad \forall E \tag{3.53}$$

is satisfied, where $\bar{h} = \frac{n_{\mathrm{MC}}}{n_{\mathrm{bins}}}$ is the average number of histogram entries. n_{MC} denotes the number of MC steps performed in this random walk, and n_{bins} is the number of energy bins. The ratio of all histogram entries to the average $\bar{h}$ has to be at least x, where the parameter x is typically chosen between 0.8 and 0.95, depending on the system that is analyzed. When x is set to a too large number, the histogram may never reach "flatness", and too small numbers can affect accuracy.
If the histogram is flat, the factor f is modified. A constraint is that f has to decrease monotonically so that it converges to 1. A common choice is to apply a power law

$$f_{i+1} = f_i^d \quad \text{with} \quad d \in (0,1) \; , \tag{3.54}$$

starting with $f = \exp(1)$, i.e. $\ln f = 1$. The histogram entries are reset to $h(E) = 0$, and a new random walk is started with the updated modification factor f (i.e., a new iteration of the Wang-Landau algorithm is performed). The estimates for the density of states are of course adopted from the previous iteration, since they are to be improved continuously.

The accuracy of the estimate $g(E)$ is proportional to $\ln f$, therefore f will be decreased each time a flat histogram was produced. However, we cannot set f arbitrarily close to 1, since then no modification would take place in eq.(3.51). The simulation is hence stopped when f reaches a final value, e.g. $f_{\text{final}} = \exp(10^{-8})$.
The modification factor f controls the simulation. A large f leads to a fast acquisition (i.e. after a small number of MC steps) of a flat histogram in the early iterations of the algorithm. By decreasing f after each iteration the estimates $g(E)$ will be modified more accurately in later iterations, but the random walk usually requires more steps to produce a flat histogram. The parameter d of the power law (3.54) contains a trade-off between accuracy and computer time. Choosing d too small may not give the algorithm enough time (i.e. MC steps) to reach a good accuracy for $g(E)$ before the final iteration is reached, and too large values can be a waste of computer time. Setting $d = 0.5$ yields good accuracy for many systems while keeping computer time relatively short [47].

Detailed balance

The detailed balance condition (cf. eq.(3.40)) is not strictly satisfied during the course of the simulation. The transition probabilities are not based on the true density of states, but rather on the current estimate for $g(E)$. Thus, the detailed balance condition

$$\frac{1}{g(E_1)} W\left(E_1 \to E_2\right) = \frac{1}{g(E_2)} W\left(E_2 \to E_1\right) \ , \tag{3.55}$$

calculated from (3.52), is only satisfied with accuracy proportional to the modification factor $\ln f$. This is in contrast to the Metropolis algorithm, where detailed balance is always satisfied, because the correct probability for the canonical ensemble is chosen (Boltzmann factor).

Scaling of resulting data

After the algorithm has reached the specified minimum modification factor f_{final}, the values for $g(E)$ represent the final approximation of the density of states. However, the $g(E)$ are only relative densities of the states for different energies. If a normalization is required, the $g(E)$ can be rescaled either in a way that the known degeneracy of a special state (e.g. two for the ground state of the Ising model) is reproduced, or alternatively the weight of all states $\sum_\nu g(E_\nu)$ equals one or the number of states of the system (e.g. 2^N for the Ising model).

Comparison to Metropolis method

Compared to the Metropolis algorithm, the Wang-Landau method has several advantages. For certain situations, e.g. the system being close to a phase transition, the

traditional Metropolis algorithm exhibits long time scales. Additionally, Metropolis sampling is performed at a specified temperature. Thus, in order to obtain the temperature dependence of a variable, several simulations have to be run at different temperatures. Furthermore, it is difficult to extract certain thermodynamic variables such as the free energy or the entropy from Metropolis data. These variables are only accessible via integration of other thermodynamic quantities, which accumulates statistical errors contained in the latter.
Wang-Landau sampling, on the other hand, directly calculates the density of states $g(E)$, which readily delivers e.g. the free energy:

$$F(T) = -k_\mathrm{B}T \ln Z = -k_\mathrm{B}T \ln \sum_\nu g(E_\nu)\, e^{-E/k_\mathrm{B}T} \,, \tag{3.56}$$

The density of states is independent of the temperature. Hence, after $g(E)$ has been calculated once, thermodynamic means can be calculated for any temperature.

Improvement of convergence

The improvement proposed by Zhou and Bhatt [48] involves an additional constraint to the number of histogram entries. Not only has the histogram to be flat, but also a minimum number of samples has to be gathered for each iteration of the algorithm, depending on the current modification factor f:

$$h(E) > \frac{1}{\sqrt{\ln f}} \quad \forall E \,. \tag{3.57}$$

Using this scheme, the efficiency of each iteration of the algorithm is optimized. Without the Zhou-Bhatt constraint, the algorithm can too quickly decrease the modification factor f in early iterations, while the approximation of the density of states $g(E)$ can still be very inaccurate. In later iterations, with small modification factor f, the algorithm will then take many more steps of the random walk to improve $g(E)$.

3.5.2 Application to the classical Heisenberg model

The Wang-Landau algorithm will be applied to the classical Heisenberg model in this project. Since the Hamiltonian function (3.10) is the sum of scalar products between classical vectors, the energy is a continuous function of the spin orientations. In order to apply the Wang-Landau method, the energy interval between the ground state E_0 and the state with maximum energy E_max has to be discretized into bins. We will use equidistant energy bins, but this is not a necessity for the algorithm. The number of energy bins will be chosen according to the desired resolution of $g(E)$.
The update procedure between subsequent steps of the random walk involves the change of the spin vectors. Unlike for the Ising model, where changing the spins is

simply done by "flipping" to the opposite direction, the procedure here has to be able to access the complete unit sphere (see parametrization in eq.(3.13)). The update scheme has to produce uniformly distributed random configurations on the unit sphere. A simple approach would be to use uniformly distributed random numbers for each Cartesian coordinate of the spin vector (from the interval $[-1, 1]$). If the length of the proposed spin is less than or equal to one (inside unit sphere), the spin can be used as a new configuration (after renormalization to length one).
An alternative procedure is the Marsaglia method [10]. Two random numbers r_1 and r_2 are generated from a uniform distribution on $[0, 1]$, forming the vector

$$\boldsymbol{\xi} = \begin{pmatrix} 1 - 2r_1 \\ 1 - 2r_2 \end{pmatrix} \text{ with (squared) length } \xi^2 = \xi_1^2 + \xi_2^2 \,. \tag{3.58}$$

If the length $\xi^2 < 1$, the new spin configuration is

$$\mathbf{s}_{i+1} = \begin{pmatrix} 2\xi_1\sqrt{1-\xi^2} \\ 2\xi_2\sqrt{1-\xi^2} \\ 1 - 2\xi^2 \end{pmatrix} \,. \tag{3.59}$$

Both methods described above will produce random configurations that are uniformly distributed on the unit sphere. They can in principle be implemented as the update procedure for Wang-Landau algorithm for the Heisenberg model. However, allowing the spins to change to an arbitrary direction with each step of the random walk implicates problems for the evaluation of the whole range of the energy spectrum. We have performed simulations based on the update scheme described above, and an analysis of the random walk showed that the parts of the energy spectrum which only carry a small weight $g(E)$ were visited very rarely. Hence, the algorithm cannot produce a flat histogram $h(E)$. We have therefore implemented a refined update procedure.
The spin states are now only allowed to change to a new configuration that is inside a cone with a given radius $r_{\max}$ around the previous configuration. The algorithm is based on the update procedure used in the Ψ-Mag toolkit for computational magnetism [49], with some minor modifications.
First, a cylindrical coordinate system is defined with the previous spin configuration $\mathbf{s}_i = (x, y, z)^T$ defining the z'-axis. Then, two random numbers r_1 and r_2 (uniformly distributed in the interval $[0, 1]$) are generated. In the cylindrical system, the radius $\rho = r_1\, r_{\max}$ is limited by the maximum radius $r_{\max}$, whereas the azimuth is allowed assume all angles: $\alpha = 2\pi\, r_2$. The z'-component has to be $z' = \sqrt{1-\rho^2}$ in order to retain unit length. In Cartesian coordinates ($\mathbf{s}_i$ is direction of z-axis), the new spin configuration can be written as

$$\mathbf{s}'_{i+1} = \begin{pmatrix} \rho\,\cos\alpha \\ \rho\,\sin\alpha \\ z' \end{pmatrix} \,. \tag{3.60}$$

The vector $\mathbf{s}'_{i+1}$ has to be transformed into the original coordinate system:

$$\mathbf{s}_{i+1} = R\,\mathbf{s}'_{i+1}\,, \tag{3.61}$$

with the rotation matrix

$$R = \begin{pmatrix} \frac{xz}{r} & -\frac{y}{r} & x \\ \frac{yz}{r} & \frac{x}{r} & y \\ -r & 0 & z \end{pmatrix}\,, \tag{3.62}$$

where $r = \sqrt{x^2 + y^2}$. The resulting vector is normalized and is inside the cone defined by the previous state $\mathbf{s}_i$ and the radius $r_{\max}$.
Using the refined update scheme, the random walk can explore regions with small spectral weight $g(E)$ more efficiently (usually the regions close to E_0 and $E_{\max}$). An update to the configuration will produce a state in the near energetic vicinity, whereas an unrestricted reorientation of the spin can easily lead to a long jump in the energy spectrum.

Random number generator

For the generation of random numbers in our implementation, we use the MT19937 ("Mersenne Twister") algorithm from the GNU scientific library [50]. It provides a very large recurrence period of $2^{19937} - 1$ and has been shown to be uniformly distributed (even in high dimensions) and having very weak correlations [51].

3.5.3 Results

We will now present results obtained with our implementation of the Wang-Landau algorithm for classical spin systems. These results are compared to exact results, if available, or otherwise their statistical errors will be analyzed.

Trimer

Figure 3.5(left) shows the Wang-Landau data for the spin trimer, with the density of states normalized so the integral over all energies yields one. The right graph in this figure shows the deviation from the exact result (cf. Sec. 3.3.3). We find very good agreement between the exact result and our numerical data.
The algorithm was performed using 100 energy bins between ground state and maximum energy, the histogram flatness criterion was $x = 0.95$. We decreased the modification factor f with the exponent 0.8, with $f_{\text{final}} = 10^{-9}$.

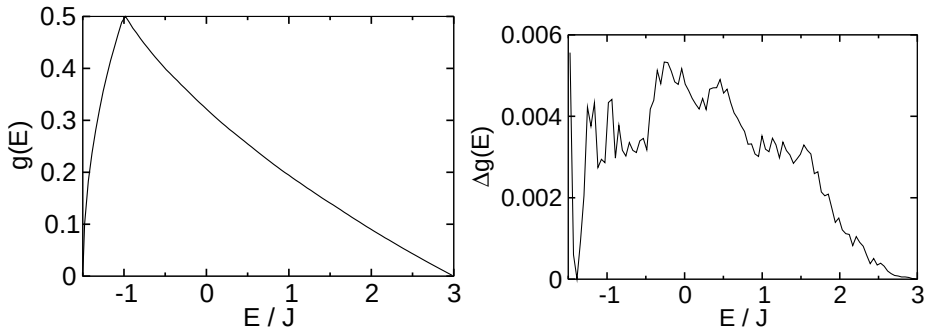

Figure 3.5: Left: Wang-Landau result for the classical density of states of the trimer. Right: Absolute difference from the exact result (3.34).

Ring with N=6

We also present the Wang-Landau data for our standard example, the spin ring with $N = 6$. Since we have access to numerical exact data for the density of states of spin rings, we can directly compare the results. Figure 3.6(left) gives the Gaussian-like density of states, and the right graph shows the absolute difference from the exact result obtained from (3.24). Again, we only find small deviations of the Wang-Landau data from the exact result.

The simulation was performed with 1000 energy bins, the histogram was considered flat at a ratio of $x = 0.95$, f was decreased with the exponent 0.8, and the algorithm terminated at $f_{\text{final}} = 10^{-9}$.

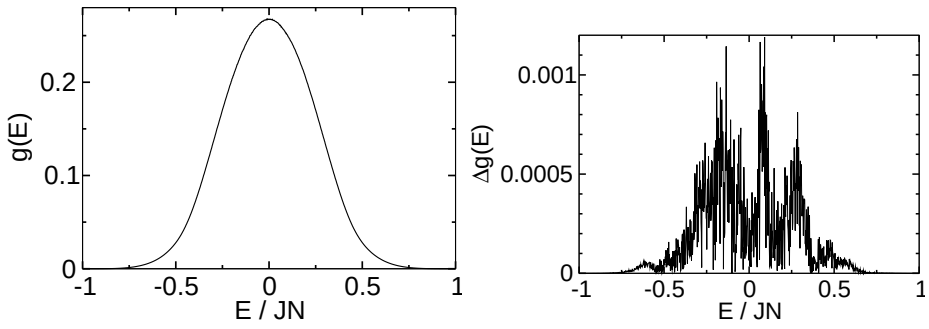

Figure 3.6: Left: Wang-Landau result for the classical density of states of the ring with $N = 6$. Right: Absolute difference from the exact result (3.24).

Classical model for $\{\mathbf{Mo_{72}Fe_{30}}\}$

Figure 3.7 shows the logarithm of the density of states for the classical model of the magnetic molecule $\{Mo_{72}Fe_{30}\}$. The weights of the energy bins are scaled so that the maximum weight at zero energy is $g(E = 0) = 1$. The graph reveals the vast difference in spectral weight of states near $E = 0$ compared to states at the borders of the spectrum, which occupy many orders of magnitude less of phase space.

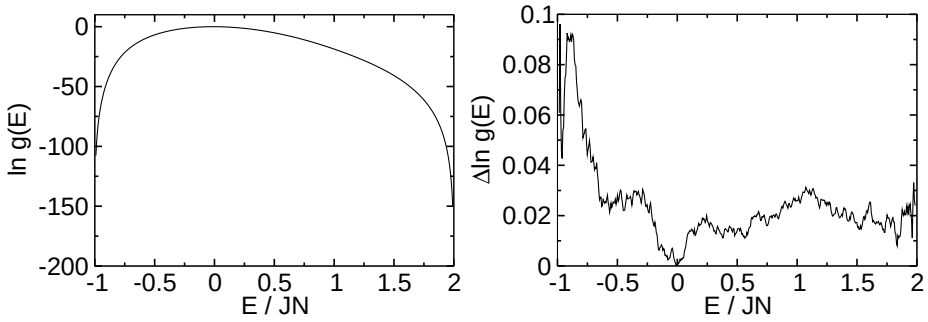

Figure 3.7: Classical density of states of $\{Mo_{72}Fe_{30}\}$ calculated with Wang-Landau. The left graph shows the relative logarithmic density of states, and the right graph shows the statistical error.

The density of states for $\{Mo_{72}Fe_{30}\}$ cannot be calculated analytically. We can therefore only give statistical errors of our results. The right graph of figure 3.7 shows the standard deviation of the logarithm of the density of states obtained from five independent runs of the algorithm. The parameters used for these results were: 500 energy bins, criterion for flatness $x = 0.85$, exponent for decreasing the modification factor 0.5, and $f_{\text{final}} = 10^{-9}$.

Since the statistical errors cannot show systematic errors in the algorithm, we additionally compare the second moment of the numerical density of states with the analytical result given in section 2.3.2. We find a relative error of $3 \cdot 10^{-4}$ from the exact result $\sigma^2 = 20$, hence the general compliance with the (unknown) exact result is good. However, the weight of states near the boundaries of the spectrum cannot be calculated accurately in the same simulation as the complete spectrum, because the probability of finding states from the center is so much larger. For the generation of figure 3.7, the histogram entries of the three energy bins nearest to both boundaries were not considered when deciding about the flatness of the whole histogram. This is necessary, because otherwise the algorithm will need unpredictably large amounts of computer time to advance to the next Wang-Landau iteration. Naturally, the data for these energy bins does not have the same statistical quality as for the other bins. If e.g. the low-energy section of the spectrum is required with good accuracy, the

Wang-Landau algorithm has to be limited to this interval, thus preventing the occurrence of too large differences in the spectral weight $g(E)$.

3.5.4 Discussion

Analyzing the results presented in the previous section, we find (in compliance with reference [52]) that the Wang-Landau algorithm can deliver accurate results for the Heisenberg model. This is not self-evident, since the Wang-Landau algorithm was developed for systems with a discrete set of energy values, e.g. the Ising model. For systems described by continuous variables, such as the classical Heisenberg model, the energy interval has to be discretized, where one has to decide about the size of the energy bins. The size of the bins could affect the convergence of the algorithm. However, for the systems we analyzed, the algorithm proved applicable for a wide range of bin sizes ($\Delta E = 0.001J$ to $\Delta E = 0.1J$). For systems with a large number of spins, e.g. the classical model of $\{Mo_{72}Fe_{30}\}$, the phase space volumes occupied by states from the center of the energy spectrum is orders of magnitude larger than the phase space volume of states that are energetically near the ground state. If the algorithm is applied to such a system, one has to subdivide the energy spectrum into smaller intervals and apply the algorithm to these subunits. The intervals have to be defined so that they have an overlap with the neighboring intervals. This way, the normalization of the whole spectrum can be achieved by matching the density of states at the overlapping energy values. The procedure of performing multiple Wang-Landau runs on subunits of the energy range, however, is also necessary for discrete models with a large number of sites (cf. Ref. [47]), and is not a special problem of the Heisenberg model.
The Wang-Landau algorithm completes our set of tools for the description of classical systems. Whereas the exact solution presented in section 3.3 is limited to the class of spin rings and becomes numerically demanding for a large number of spins, the Wang-Landau algorithm is general and delivers an approximation of the density of states for systems with an arbitrary interaction matrix J_{ij}. It serves as the basis for the connection between classical and quantum spectrum in chapter 4.

4 Quantum corrections for the classical density of states

In the previous chapters we have discussed properties of spin systems either in the quantum mechanical or in the classical regime. The classical description of a physical system can be regarded as the limiting case of quantum mechanics for large quantum numbers. For the spin systems described here, the classical limit is expected for $s \to \infty$ (and $\hbar \to 0$ at the same time), i.e., the spin angular momentum becoming a continuous variable. However, different definitions of the classical limit exist in the literature. The Ehrenfest classical limit, e.g., is realized, when the dynamics of a wave packet can be described by the Hamiltonian equations of motion for a classical particle. This picture is valid for large masses and slowly changing potentials (compared to the width of the wave packet) [53].
In this chapter, we will discuss relations between the density of states for quantum and classical systems. In quantum mechanics, energy eigenstates are calculated by solving the time-independent Schrödinger equation, i.e., the Hamiltonian is diagonalized. One obtains a set of eigenvalues, which constitute the energy spectrum of the system. The spectrum can be described by the density of states, $g^q(E)$, which is defined in the following way. Let $G^q(E, \epsilon)$ denote the number of states in the energy interval $[E - \epsilon/2, E + \epsilon/2]$. If the number of states scales linearly with ϵ, the density of states is the number of states contained in a small interval per interval width,

$$g^q(E) = \frac{G^q(E, \epsilon)}{\epsilon} \,. \tag{4.1}$$

We cannot take the limit $\epsilon \to 0$, because this will either yield $g^q(E) = 0$, or (4.1) does not converge, in case E equals an eigenvalue of the quantum Hamiltonian.
Compared to the definition of the classical density of states in eq.(3.2), the quantum mechanical density of states is based on an entirely different source. While the classical density of states is always well-defined by the integral over continuous variables p and q, $g^q(E)$ is derived from a discrete set of energy eigenvalues and only makes sense for well-behaved distributions, i.e., when eq.(4.1) can be used.
Following from their different definitions, one cannot expect a general similarity between the classical and the quantum version of the density of states. However, we will show in this chapter that a general expression can be established, which connects classical and quantum spectrum. Furthermore, we will demonstrate specifically for Heisenberg spin systems, how this correspondence can be constructed.

4.1 Correspondence of classical and quantum spectrum

In the course of this section, we will give an alternative expression for the number of quantum states in a given energy interval, based on the spectra of states which span the Hilbert space [54].
The quantum spectrum of the Hamiltonian, $G^q(E) := G^q(E, \epsilon \to 0)$, is not evaluated directly. We will instead analyze the probability distribution of the totally mixed state

$$\hat{\mathbb{1}} := \sum_{\nu} |\,\psi_\nu\,\rangle\langle\,\psi_\nu\,| \;, \tag{4.2}$$

where all states $|\,\psi_\nu\,\rangle$ are occupied with the same probability. The probability to find $\hat{\mathbb{1}}$ in an arbitrary energy interval is proportional to the number of states contained in that interval. Since $\hat{\mathbb{1}}$ is an incoherent mixture of states $|\,\psi_\nu\,\rangle$, the spectrum will result as the sum of the individual spectra of these states. If we can write $\hat{\mathbb{1}}$ as a mixture of states, where each state corresponds to a point in classical phase space, a connection between classical and quantum spectrum is established.
In section 4.2, we will introduce the spin-coherent states, which yield the same energy expectation values for the quantum Heisenberg Hamiltonian as the corresponding classical spins with the same parameters do for the classical Hamiltonian. The spin-coherent states will serve as the basis of a numerical algorithm to derive quantum corrections for the classical density of states.

4.1.1 Formal description

We introduce the special operator $\hat{\Pi}(E)$, defined by the equation

$$\hat{H} =: \sum_{E} E\,\hat{\Pi}(E) \;, \tag{4.3}$$

i.e., $\hat{\Pi}(E)$ projects onto the eigenspace of the Hamiltonian $\hat{H}$ with corresponding energy E. The trace of this operator equals the number of states with the given energy E:

$$G^q(E) = \mathrm{Tr}\,\hat{\Pi}(E) \;. \tag{4.4}$$

When we think of states characterized by parameters $\vec{\gamma}$, the trace in the previous formula can be expressed as

$$\mathrm{Tr}\,\hat{\Pi}(E) = \int \mathrm{d}\vec{\gamma}\,\langle\,\vec{\gamma}\,|\,\hat{\Pi}\,|\,\vec{\gamma}\,\rangle \;, \tag{4.5}$$

if the integral over the projectors $|\,\vec{\gamma}\,\rangle\langle\,\vec{\gamma}\,|$ yields the $\hat{\mathbb{1}}$-operator:

$$\int \mathrm{d}\vec{\gamma}\;|\,\vec{\gamma}\,\rangle\langle\,\vec{\gamma}\,| = \hat{\mathbb{1}} \;. \tag{4.6}$$

The validity of (4.5) only depends on the completeness relation (4.6). Orthogonality is not required, i.e., $\langle \vec{\gamma}' \,|\, \vec{\gamma} \rangle \neq 0$ for different parameters $\vec{\gamma}$, $\vec{\gamma}'$ is allowed. We also require the states $|\, \vec{\gamma} \,\rangle$ to be normalized in the following way:

$$\int\limits_{\vec{\gamma} \in V} \mathrm{d}\vec{\gamma} \, \langle \, \vec{\gamma} \,|\, \vec{\gamma} \, \rangle = V \tag{4.7}$$

The volume integral over the norm of the state yields the volume itself.
We now define the spectrum of a single state $|\, \vec{\gamma} \,\rangle$,

$$g(\vec{\gamma}, E) := \langle \, \vec{\gamma} \,|\, \hat{\Pi}(E) \,|\, \vec{\gamma} \, \rangle \; . \tag{4.8}$$

Thus, we find that the quantum mechanical spectrum can be expressed as

$$G^q(E) = \int \mathrm{d}\vec{\gamma} \, g(\vec{\gamma}, E) \; . \tag{4.9}$$

The full spectrum $G^q(E)$ is obtained by integrating over the individual spectra of the contributions $|\, \vec{\gamma} \,\rangle$.

Connection to classical density of states

Let us now assume we have quantum states whose energy expectation values equal the classical Hamiltonian function for the parameters $\vec{\gamma}$, i.e.

$$\langle \, \vec{\gamma} \,|\, \hat{H} \,|\, \vec{\gamma} \, \rangle = H(\vec{\gamma}) \; . \tag{4.10}$$

We will switch back to a description with energy bins of a finite width. When we recall the expression for the volume of classical phase space occupied by the states with energies $[E - \epsilon/2, E + \epsilon/2]$ given in eq.(3.1), we find

$$G^c(E, \epsilon) = \int \mathrm{d}\vec{\gamma} \, \Theta \left(\frac{\epsilon}{2} - |E - H(\vec{\gamma})| \right) = \int\limits_{E - \epsilon/2 \leq H(\vec{\gamma}) \leq E + \epsilon/2} \mathrm{d}\vec{\gamma} \; . \tag{4.11}$$

We can reformulate the quantum mechanical spectrum (4.9) as an integral over energy:

$$G^q(E, \epsilon) = \int \mathrm{d}E' \; G^c(E', \epsilon) \, \bar{g}_{E'}(E, \epsilon) \; , \tag{4.12}$$

where $\bar{g}_{E'}(E, \epsilon)$ denotes the normalized accumulated spectrum of all states in the energy interval $[E' - \epsilon/2, E' + \epsilon/2]$:

$$g_{E'}(E, \epsilon) = \int\limits_{E' - \epsilon/2 \leq H(\vec{\gamma}) \leq E' + \epsilon/2} \mathrm{d}\vec{\gamma} \, g(\vec{\gamma}, E) \tag{4.13}$$

and

$$\bar{g}_{E'}(E,\epsilon) := \frac{g_{E'}(E,\epsilon)}{G^c(E,\epsilon)} \ , \tag{4.14}$$

so that, because of (4.7),

$$\int \mathrm{d}E \ \bar{g}_{E'}(E,\epsilon) = 1 \ . \tag{4.15}$$

The accumulated spectrum of the states in the ϵ-neighborhood of E' represents the phase space volume $G^c(E',\epsilon)$, since these states correspond to classical states with $|H(\vec{\gamma}) - E'| \leq \epsilon/2$. Hence, the full quantum spectrum $G^q(E',\epsilon)$ in eq.(4.12) can be written as an integral over all contributing normalized spectra $\bar{g}_{E'}(E,\epsilon)$, weighted with the classical phase space volumes $G^c(E',\epsilon)$.
Thus, we have arrived at an expression that connects the quantum spectrum $G^q(E,\epsilon)$ to the classical phase space volume $G^c(E,\epsilon)$. The energy distribution $\bar{g}_{E'}(E,\epsilon)$ of the states with mean energy E' determines the degree of similarity between quantum and classical spectrum. If the weight distributions $\bar{g}_{E'}(E,\epsilon)$ are concentrated very closely around the mean energies E', the integration (4.12) will not modify the classical spectrum $G^c(E,\epsilon)$ to a significant extent. In this case, i.e. for very narrow energy distributions of the states used to span the Hilbert space, the quantum spectrum will be similar to the classical density of states.
Generally, the limit of narrow energy distributions of the contributing states $|\,\vec{\gamma}\,\rangle$ cannot be expected to be satisfied. Eq.(4.12) can then be used as the basis for an approximate scheme to describe the quantum spectrum. If we have access to the classical spectrum $G^c(E',\epsilon)$ for the energy intervals E' and the spectra of quantum states contained in these intervals, we can approximate the total quantum spectrum by

$$G^q(E,\epsilon) \approx \sum_{E'} G^c(E',\epsilon)\, \bar{g}_{E'}(E) \tag{4.16}$$

Of course the method will not be able to deliver the set of exact eigenvalues of the quantum Hamiltonian, but it can give an estimate of the number of states contained in the ϵ-interval around the energy E. That is, the method will not be able to predict, e.g., the energy gap between ground state and first excited state. However, as we have demonstrated in section 2.3.1, the information about how many quantum states are present in an energy interval is sufficient to calculate thermodynamic properties such as the specific heat with a good accuracy, even with only 100 energy bins.

4.2 Spin-coherent states

In the previous section, we established a correspondence of classical and quantum spectrum. The derivation relied on a special set of states $|\,\vec{\gamma}\,\rangle$, where $\vec{\gamma}$ denotes a

point in classical phase space. We will show in this section that for the Heisenberg model, we can base our approach upon the so-called spin-coherent states

In reference [55] it was shown that one can construct spin states analogous to the coherent states of the harmonic oscillator. Whereas the coherent states were introduced as minimum position-momentum uncertainty states and are characterized by p and q representing a point in phase space, the spin-coherent states relate states in quantum spin space to classical spin vectors.

The spin-coherent states originally were introduced without a specific purpose, but rather for showing the analogy to the already known coherent states in position-momentum space. Later, other authors picked up the formalism and developed various applications. The spin-coherent states were used e.g. to analyze ferromagnetic Heisenberg chains in the continuum limit [56] or for the semi-classical description of spin dynamics [57].

The spin-coherent states can be generated from the fully magnetized $\hat{s}^z$-eigenstate $|\, s, m = s \,\rangle \equiv |\, s \,\rangle$ using the unitary operator $U(\theta, \phi)$ with the spherical angles θ and ϕ. The operator can be defined as a consecutive rotation about y- and z-axis [57]

$$U(\theta, \phi) = e^{-\mathrm{i}\phi\hat{s}^z} e^{-\mathrm{i}\theta\hat{s}^y} \tag{4.17}$$

with $0 \leq \theta \leq \pi$ and $0 \leq \phi \leq 2\pi$. In the basis of $\hat{s}^z$ eigenstates, the spin-coherent states can then be expressed as

$$\begin{aligned}
|\, s, \Omega \,\rangle = |\, s, \theta, \phi \,\rangle &= U(\theta, \phi) \,|\, s \,\rangle \\
&= \sum_{n=0}^{2s} |\, s-n \,\rangle\langle\, s-n \,|\, U(\theta, \phi) \,|\, s \,\rangle \\
&= \sum_{n=0}^{2s} e^{\mathrm{i}\phi\,(n-s)} \,|\, s-n \,\rangle\langle\, s-n \,|\, \exp\left(-\mathrm{i}\theta\hat{s}^y\right) \,|\, s \,\rangle \\
&= \sum_{n=0}^{2s} \binom{2s}{n}^{\frac{1}{2}} \left(\cos\frac{\theta}{2}\right)^{2s-n} \left(\sin\frac{\theta}{2}\right)^{n} e^{\mathrm{i}\phi\,(n-s)} \,|\, s-n \,\rangle\,,
\end{aligned} \tag{4.18}$$

where we have made use of Wigner's formula (A.1) to calculate the matrix elements $\langle\, s-n \,|\, e^{-\mathrm{i}\theta\hat{s}^y} \,|\, s \,\rangle$ of the operator describing the rotation about the y-axis.

The following operator identities will be useful for the derivation of expectation values $\langle\, s, \Omega \,|\, \hat{A} \,|\, s, \Omega \,\rangle$, with $\hat{A}$ being a product of the spin operators $\hat{s}^z$, $\hat{s}^+$, and $\hat{s}^-$. The transformation of $\hat{s}^z$ by the operator $\hat{U}$ can be expressed as a rotation about the

y-axis:

$$\begin{aligned}\hat{U}^\dagger\,\hat{s}^z\,\hat{U} &= e^{\mathrm{i}\theta\hat{s}^y}\,\hat{s}^z e^{-\mathrm{i}\theta\hat{s}^y} \\ &= -\sin\theta\;\hat{s}^x + \cos\theta\,\hat{s}^z \\ &= -\frac{1}{2}\sin\theta\;\hat{s}^+ - \frac{1}{2}\sin\theta\;\hat{s}^- + \cos\theta\;\hat{s}^z\;. \end{aligned} \tag{4.19}$$

The identity

$$\hat{U}^\dagger\,\hat{s}^+\,\hat{U} = e^{\mathrm{i}\phi}\left[\cos^2\frac{\theta}{2}\;\hat{s}^+ - \sin^2\frac{\theta}{2}\;\hat{s}^- + \sin\theta\;\hat{s}^z\right] \tag{4.20}$$

can be derived using the Baker-Campbell-Hausdorff formula [58] and the commutator relations for the three spin operators. Analogously,

$$\hat{U}^\dagger\,\hat{s}^-\,\hat{U} = \left(\hat{U}^\dagger\,\hat{s}^+\,\hat{U}\right)^\dagger = e^{-\mathrm{i}\phi}\left[\cos^2\frac{\theta}{2}\;\hat{s}^- - \sin^2\frac{\theta}{2}\;\hat{s}^+ + \sin\theta\;\hat{s}^z\right]\;. \tag{4.21}$$

4.2.1 Some properties of spin-coherent states

Following the above definition, the spin-coherent states have interesting features relating them to classical spin vectors [57]. The expectation value of the vector spin operator equals a classical vector with length s, classified by the pair of angles $\Omega(\theta,\phi)$:

$$\langle\, s,\Omega \,|\, \hat{\mathbf{s}} \,|\, s,\Omega\,\rangle = \begin{pmatrix} s\,\cos\phi\,\sin\theta \\ s\,\sin\phi\,\sin\theta \\ s\,\cos\theta \end{pmatrix} = s\,\mathbf{e}_{\theta,\phi} \tag{4.22}$$

and the normalization

$$\langle\, s,\Omega \,|\, s,\Omega\,\rangle = 1\;. \tag{4.23}$$

However, the spin-coherent states are not orthogonal, since following from (4.18), the overlap is

$$\langle\, s,\Omega_k \,|\, s,\Omega_l\,\rangle = e^{\mathrm{i}\,(\phi_k-\phi_l)\,s}\cdot\left(\cos\frac{\theta_k}{2}\,\cos\frac{\theta_l}{2} + \sin\frac{\theta_k}{2}\,\sin\frac{\theta_l}{2}\,e^{\mathrm{i}\,(\phi_l-\phi_k)}\right)^{2s}\;. \tag{4.24}$$

The absolute value of the overlap can be expressed by the corresponding classical unit vectors:

$$|\langle\, s,\Omega_k \,|\, s,\Omega_l\,\rangle| = \sqrt{\langle\, s,\Omega_k \,|\, s,\Omega_l\,\rangle\langle\, s,\Omega_l \,|\, s,\Omega_k\,\rangle} = \left(\frac{1+\mathbf{e}_{\theta_k,\phi_k}\cdot\mathbf{e}_{\theta_l,\phi_l}}{2}\right)^s\;. \tag{4.25}$$

The overlap is zero only if the vectors $\mathbf{e}_{\theta_k,\phi_k}$ and $\mathbf{e}_{\theta_l,\phi_l}$ are aligned anti-parallelly.

As their counterparts in the harmonic oscillator, the spin-coherent states exhibit the minimum uncertainty product

$$\Delta\left(\mathbf{e}_1 \cdot \hat{\mathbf{s}}\right) \Delta\left(\mathbf{e}_2 \cdot \hat{\mathbf{s}}\right) = \frac{1}{2} \left|\langle \mathbf{e}_3 \cdot \hat{\mathbf{s}} \rangle\right| \ , \tag{4.26}$$

with an arbitrary orthonormal system of vectors $\mathbf{e}_1$, $\mathbf{e}_2$, $\mathbf{e}_3$. Furthermore, the spin-coherent states fulfill the completeness relation

$$\frac{2s+1}{4\pi} \int_0^{2\pi} \mathrm{d}\phi \int_0^{\pi} \mathrm{d}\theta \, \sin\theta \, |\, s, \Omega \,\rangle\langle\, s, \Omega \,| \, = \hat{\mathbb{1}} \ . \tag{4.27}$$

N-spin system

In order to describe a system of spins by coherent states, we can construct the product of spin-coherent states

$$|\, \vec{s}, \vec{\Omega} \,\rangle = |\, s_1, \Omega_1 \,\rangle \otimes |\, s_2, \Omega_2 \,\rangle \otimes \ldots \otimes |\, s_N, \Omega_N \,\rangle \ . \tag{4.28}$$

This definition allows the system to be comprised of spins with different quantum numbers s_i. For the work presented here, only systems with a common s are investigated, and the notation can be simplified to $|\, s, \vec{\Omega} \,\rangle$ in these cases.

Expectation values for the Heisenberg Hamiltonian

The above described properties have useful consequences for the calculation of expectation values of the quantum mechanical Heisenberg Hamiltonian (2.2).
The energy expectation value becomes

$$\begin{aligned} \langle\, s, \vec{\Omega} \,|\, \hat{H} \,|\, s, \vec{\Omega} \,\rangle &= \sum_{i<j} J_{ij} \, \langle\, s, \vec{\Omega} \,|\, \hat{\mathbf{s}}_i \cdot \hat{\mathbf{s}}_j \,|\, s, \vec{\Omega} \,\rangle \\ &= \sum_{i<j} J_{ij} \, \mathbf{s}_i \cdot \mathbf{s}_j = \sum_{i<j} J_{ij} \, s^2 \, \mathbf{e}_{\theta_i,\phi_i} \cdot \mathbf{e}_{\theta_j,\phi_j} \ , \end{aligned} \tag{4.29}$$

where we have used eqs.(4.22) and (4.28). When we compare the expectation value to the definition of the classical Heisenberg model in eq.(3.10), we find that the two quantities only differ in the scaling of the interaction matrix. This follows the fact that the Heisenberg model only depends on the scalar products between interacting spins, and the expectation value of the spin vector operator for spin-coherent states yields the corresponding classical vector. Thus, the spin-coherent states can be used as a direct mapping of classical vectors to quantum states.

4.2.2 Spectrum of spin-coherent states

For the evaluation of the spectrum of a spin coherent state $|\,\vec{s},\vec{\Omega}\,\rangle$, we can represent the projector in eq.(4.3) with the eigenstates $|\,\phi_j\,\rangle$ of $\hat{H}$:

$$\hat{\Pi}(E) = \sum_j \delta(E - E_j)\;|\,\phi_j\,\rangle\langle\,\phi_j\,|\;. \tag{4.30}$$

Therefore, the spectrum of the spin-coherent state $|\,\vec{s},\vec{\Omega}\,\rangle$ becomes

$$\begin{aligned} g(\vec{s},\vec{\Omega},E) &= \sum_j \delta(E - E_j)\,\langle\,\vec{s},\vec{\Omega}\,|\,\phi_j\,\rangle\langle\,\phi_j\,|\,\vec{s},\vec{\Omega}\,\rangle \\ &= \sum_j \delta(E - E_j)\,\left|\langle\,\vec{s},\vec{\Omega}\,|\,\phi_j\,\rangle\right|^2\;. \end{aligned} \tag{4.31}$$

Thus, for the evaluation of $g(\vec{s},\vec{\Omega},E)$, we need to calculate the projections of the given state $|\,\vec{s},\vec{\Omega}\,\rangle$ onto all eigenstates of $\hat{H}$. In numerical exact diagonalization, it is often convenient to choose the eigenstates of the total $\hat{S}^z$ operator as basis states. In this case the numerical data represents the eigenstates as coefficients C_{jk} of the linear combination of basis states $|\,\vec{m}_k\,\rangle := |\,m_{k1}, m_{k2}, \ldots, m_{kN}\,\rangle$:

$$|\,\phi_j\,\rangle = \sum_k C_{jk}\;|\,\vec{m}_k\,\rangle\;. \tag{4.32}$$

In this representation, the spectrum of a given state $|\,\vec{s},\vec{\Omega}\,\rangle$ can be expressed as

$$g(\vec{s},\vec{\Omega},E) = \sum_j \delta(E - E_j)\,\left|\sum_k C_{jk}\,\langle\,\vec{s},\vec{\Omega}\,|\,\vec{m}_k\,\rangle\right|^2\;. \tag{4.33}$$

Now we consider the overlaps $\langle\,\vec{s},\vec{\Omega}\,|\,\vec{m}_k\,\rangle$. The N-spin state $|\,\vec{s},\vec{\Omega}\,\rangle$ is a product state of spin-coherent states. We use the definition given in eq.(4.18) to obtain a representation with $\hat{S}^z$-eigenstates, which is useful for the evaluation of the inner products in eq.(4.33). These can be written as

$$\begin{aligned} &\langle\,\vec{s},\vec{\Omega}\,|\,\vec{m}_k\,\rangle = \prod_{l=1}^{N}\langle\,s_l,\Omega_l\,|\,m_{kl}\,\rangle = \prod_{l=1}^{N}\langle\,s_l\,|\,U^\dagger(\theta_l,\phi_l)\,|\,m_{kl}\,\rangle \\ &= \prod_{l=1}^{N}\left\{\sum_{n_l=0}^{2s_l}\binom{2s_l}{n_l}^{\frac{1}{2}}\left(\cos\frac{\theta_l}{2}\right)^{2s_l-n_l}\left(\sin\frac{\theta_l}{2}\right)^{n_l}\;e^{-\mathrm{i}\phi_l\,(n_l-s_l)}\langle\,s_l-n_l\,|\,m_{kl}\,\rangle\right\} \\ &= \prod_{l=1}^{N}\left\{\binom{2s_l}{s_l-m_{kl}}^{\frac{1}{2}}\left(\cos\frac{\theta_l}{2}\right)^{s_l+m_{kl}}\left(\sin\frac{\theta_l}{2}\right)^{s_l-m_{kl}}\;e^{\mathrm{i}\phi_l m_{kl}}\right\}\;, \end{aligned} \tag{4.34}$$

because the eigenstates of $\hat{S}^z$ are orthonormal:

$$\langle\, s_l - n_l \,|\, m_{kl} \,\rangle = \delta_{s_l - n_l, m_{kl}} \,. \tag{4.35}$$

The spectrum $g(\vec{s}, \vec{\Omega}, E)$ of an arbitrary spin-coherent state $|\, \vec{s}, \vec{\Omega} \,\rangle$ can now be evaluated using eq.(4.34). It could serve as part of an algorithm that generates spin-coherent states and adds up their contributions to the total energy spectrum of the system, according to eq.(4.16). However, the evaluation of (4.34) consumes significant computer time. The fact that, for each spin-coherent state's spectrum to be added, eq.(4.34) has to be evaluated many times prohibits this approach (from (4.33) we find that for each spin-coherent state, (4.34) is required $\dim \mathcal{H}$ times). Additionally, it would require the knowledge of all eigenstates of the system. Therefore, it could only serve as a verification tool for the method, because the properties of the system could then also be calculated directly from the eigenstates and eigenvalues.
We have implemented eq.(4.33) mainly as a tool for the investigation of the spectra of special states in the system. The information gained from the spectra is later used to decide on the shape of simplified spectral functions to approximate $g(\vec{s}, \vec{\Omega}, E)$ for the algorithm.

4.2.3 Example spectra

Using formula (4.33), we can calculate the distribution of spectral weight of a given spin-coherent state. In the following paragraph, we show example spectra for different spin systems and spin configurations.

Spectrum of the spin ring N=6, s=5/2

Figure 4.1 shows spectra for spin-coherent states of the ring with $N = 6$, $s = \frac{5}{2}$. The left graph shows the state corresponding to the classical ground state of the system, the right graph gives the spectrum of a state with classical energy $E = 0$. Whereas the spectrum of the latter is a broad distribution that exhibits an approximate Gaussian shape, the spin-coherent state corresponding to the classical ground state shows a spectrum constituted by a few separated peaks.

Spectrum of the spin ring N=10, s=1

Figure 4.2 shows the spectra of the ring with $N = 10$, $s = 1$ for equivalent states as in the previous paragraph.
The results qualitatively resemble the ones found for the ring with $N = 6$, $s = \frac{5}{2}$. States from the center of the classical energy interval exhibit a Gaussian shape, whereas the classical ground state configuration yields a sparse spectrum.

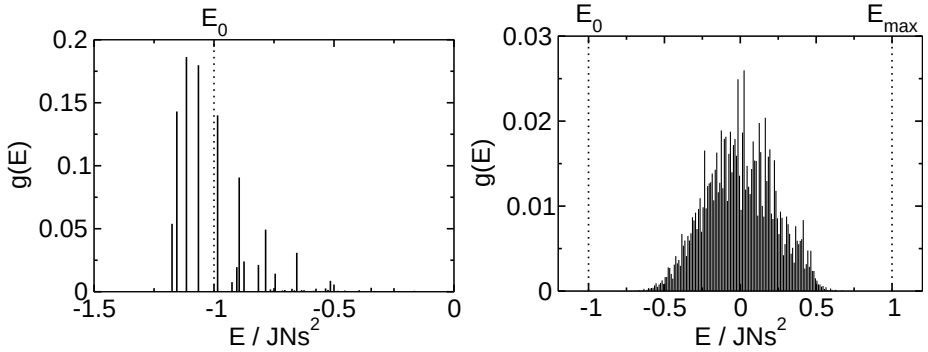

Figure 4.1: Spectra of two spin-coherent states for the Heisenberg Hamiltonian of a spin ring with $N = 6$, $s = \frac{5}{2}$. The spectral weight is integrated in equally spaced bins (width $0.01\,JNs^2$). The left graph shows a state configured equivalently to a classical ground state ($E_0 = -37.5J$), and the right graph a state with classical energy of $E = 0$. The boundaries of the classical energy range are marked by E_0 and $E_{\max}$

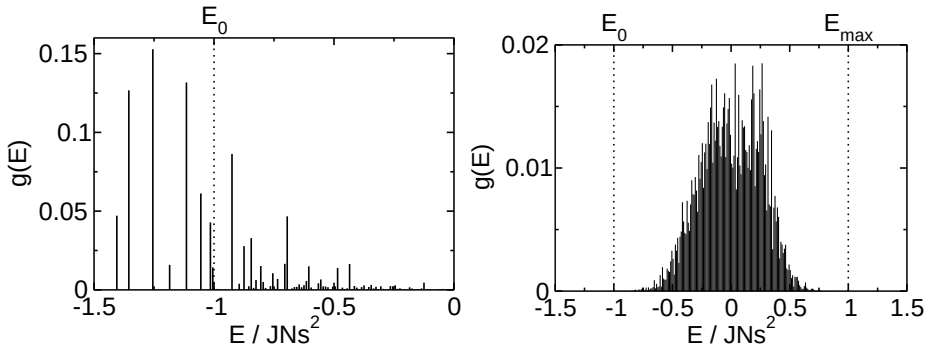

Figure 4.2: Spectra of two spin-coherent states for the Heisenberg Hamiltonian of a spin ring with $N = 10$, $s = 1$. The spectral weight is integrated in equally spaced bins (width $0.01\,JNs^2$). The left graph shows a state configured equivalently to a classical ground state ($E_0 = -10J$), and the right graph a state with classical energy of $E = 0$. The boundaries of the classical energy range are marked by E_0 and $E_{\max}$.

4.2.4 Moments of spin-coherent states

The evaluation of eq.(4.34) relies on the knowledge of all the eigenstates of the system in question. For large systems, the eigenstates are not accessible (and if they were, no approximations for the spectrum would be needed). Therefore, the spectra of the

spin-coherent states will have to be expanded into moments of the Hamiltonian. For the following formulae, we assume the total weight of the state to be normalized to one, i.e.

$$\int_{-\infty}^{\infty} \mathrm{d}E\, g(s,\vec{\Omega},E) = 1\ , \tag{4.36}$$

which can always be achieved by rescaling the weights.
The expectation value of the energy equals the Hamiltonian function for the classical Heisenberg model, as noted before:

$$\bar{E} = \int_{-\infty}^{\infty} \mathrm{d}E\, g(s,\vec{\Omega},E)\, E = H(s,\vec{\Omega})\ . \tag{4.37}$$

The variance of the Hamiltonian describes the width of the energy distribution of the given state, and is defined as the expectation value of the squared distance to the mean energy $\bar{E}$:

$$\sigma^2 = \int_{-\infty}^{\infty} \mathrm{d}E\, g(s,\vec{\Omega},E)\left(E-\bar{E}\right)^2 = \langle\, s,\vec{\Omega}\,|\,\hat{H}^2\,|\,s,\vec{\Omega}\,\rangle - \langle\, s,\vec{\Omega}\,|\,\hat{H}\,|\,s,\vec{\Omega}\,\rangle^2\ . \tag{4.38}$$

The skewness measures the asymmetry of the distribution:

$$\begin{aligned}\gamma_1 = \frac{1}{\sigma^3}\int_{-\infty}^{\infty} \mathrm{d}E\, g(s,\vec{\Omega},E)\left(E-\bar{E}\right)^3 \\ = \frac{1}{\sigma^3}\left[\langle\, s,\vec{\Omega}\,|\,\hat{H}^3\,|\,s,\vec{\Omega}\,\rangle - 3\sigma^2\bar{E} - \langle\, s,\vec{\Omega}\,|\,\hat{H}\,|\,s,\vec{\Omega}\,\rangle^3\right]\ .\end{aligned} \tag{4.39}$$

Evaluation of the second moment

The variance of a spin-coherent state $|\,s,\vec{\Omega}\,\rangle$ can be expanded as follows:

$$\begin{aligned}\sigma^2 &= \left\langle\hat{H}^2\right\rangle - \left\langle\hat{H}\right\rangle^2 = \langle\, s,\vec{\Omega}\,|\,\hat{H}^2\,|\,s,\vec{\Omega}\,\rangle - \langle\, s,\vec{\Omega}\,|\,\hat{H}\,|\,s,\vec{\Omega}\,\rangle^2 \\ &= \sum_{k<l}\sum_{k'<l'} J_{kl}J_{k'l'}\langle\, s,\vec{\Omega}\,|\,(\hat{\mathbf{s}}_k\cdot\hat{\mathbf{s}}_l)\,(\hat{\mathbf{s}}_{k'}\cdot\hat{\mathbf{s}}_{l'})\,|\,s,\vec{\Omega}\,\rangle \\ &\quad - \sum_{k<l}\sum_{k'<l'} J_{kl}J_{k'l'}\langle\, s,\vec{\Omega}\,|\,(\hat{\mathbf{s}}_k\cdot\hat{\mathbf{s}}_l)\,|\,s,\vec{\Omega}\,\rangle\langle\, s,\vec{\Omega}\,|\,(\hat{\mathbf{s}}_{k'}\cdot\hat{\mathbf{s}}_{l'})\,|\,s,\vec{\Omega}\,\rangle \\ &= \sum_{k<l}\sum_{k'<l'} J_{kl}J_{k'l'}\left[\langle\, s,\vec{\Omega}\,|\,(\hat{\mathbf{s}}_k\cdot\hat{\mathbf{s}}_l)\,(\hat{\mathbf{s}}_{k'}\cdot\hat{\mathbf{s}}_{l'})\,|\,s,\vec{\Omega}\,\rangle - (\mathbf{s}_k\cdot\mathbf{s}_l)\,(\mathbf{s}_{k'}\cdot\mathbf{s}_{l'})\right]\ ,\end{aligned} \tag{4.40}$$

where in the last line, the expectation values of the scalar products have been rewritten with classical vectors (cf. eq.(4.29)). For the further evaluation of the sum (4.40), we have to make a case differentiation of the indices $\{k,l,k',l'\}$, in order to find the combinations that lead to a contribution to the variance. As a matter of course, only

combinations in which the interaction matrix does not vanish have to be considered, i.e. $J_{kl} \neq 0$ and $J_{k'l'} \neq 0$. In the case where the indices are mutually different, the spin operators commute and can be replaced by the classical vectors. These combinations do not contribute, since they appear in the same way in both the expansions of $\langle \hat{H}^2 \rangle$ and $\langle \hat{H} \rangle^2$.
This leaves the cases where either one or two indices are equal in $\{k, l, k', l'\}$. We separate (4.40) into two sums, representing these two cases:

$$\begin{aligned}\sigma^2 = \; & J^2 \sum_{\{m,n',o'\}} \langle\, s, \vec{\Omega} \,|\, (\hat{\mathbf{s}}_m \cdot \hat{\mathbf{s}}_{n'})\,(\hat{\mathbf{s}}_m \cdot \hat{\mathbf{s}}_{o'}) \,|\, s, \vec{\Omega} \,\rangle - (\mathbf{s}_m \cdot \mathbf{s}_{n'})\,(\mathbf{s}_m \cdot \mathbf{s}_{o'}) \\ & + J^2 \sum_{\{a,b\}} \langle\, s, \vec{\Omega} \,|\, (\hat{\mathbf{s}}_a \cdot \hat{\mathbf{s}}_b)^2 \,|\, s, \vec{\Omega} \,\rangle - (\mathbf{s}_a \cdot \mathbf{s}_b)^2 \;, \end{aligned} \tag{4.41}$$

where $\{a, b\}$ denotes the cases, in which $a := k = k'$, $b := l = l'$, and $J_{ab} \neq 0$. The subset $\{m, n', o'\}$ contains the cases where the index m appears twice in $\{k, l, k', l'\}$, and $J_{mn'} J_{mo'} \neq 0$. Here we have restricted the calculation to systems with a common interaction constant, i.e. each non-zero elements of J_{kl} is assumed to be equal to J. When we combine the cases $\{m, n', o'\}$ and $\{m, o', n'\}$ to $\{m, n, o\}$, we can rewrite eq.(4.41) as a sum over real terms only:

$$\sigma^2 = J^2 \left(\sum_{\{m,n,o\}} \sigma^2_{\{m,n,o\}} + \sum_{\{a,b\}} \sigma^2_{\{a,b\}} \right) \;, \tag{4.42}$$

with

$$\sigma^2_{\{a,b\}} = \langle\, s, \vec{\Omega} \,|\, (\hat{\mathbf{s}}_a \cdot \hat{\mathbf{s}}_b)^2 \,|\, s, \vec{\Omega} \,\rangle - (\mathbf{s}_a \cdot \mathbf{s}_b)^2 \tag{4.43}$$

and

$$\begin{aligned}\sigma^2_{\{m,n,o\}} = & \langle\, s, \vec{\Omega} \,|\, (\hat{\mathbf{s}}_m \cdot \hat{\mathbf{s}}_n)\,(\hat{\mathbf{s}}_m \cdot \hat{\mathbf{s}}_o) \,|\, s, \vec{\Omega} \,\rangle \\ & + \langle\, s, \vec{\Omega} \,|\, (\hat{\mathbf{s}}_m \cdot \hat{\mathbf{s}}_o)\,(\hat{\mathbf{s}}_m \cdot \hat{\mathbf{s}}_n) \,|\, s, \vec{\Omega} \,\rangle - 2\,(\mathbf{s}_m \cdot \mathbf{s}_n)\,(\mathbf{s}_m \cdot \mathbf{s}_o) \end{aligned} \tag{4.44}$$

The terms $\sigma^2_{\{m,n,o\}}$ and $\sigma^2_{\{a,b\}}$ can be expressed with expectation values of the form $\langle\, s, \Omega \,|\, \hat{s}^\alpha \hat{s}^\beta \,|\, s, \Omega \,\rangle$, but the resulting expressions become rather lengthy. They are therefore given in the appendix in eqs.(A.3) and (A.4). The expectation values $\langle\, s, \Omega \,|\, \hat{s}^\alpha \hat{s}^\beta \,|\, s, \Omega \,\rangle$ can be evaluated using the generating operator $\hat{U}$. We give the results for the example of $\hat{s}^x \hat{s}^x$ here:

$$\begin{aligned}\langle\, s, \Omega \,|\, \hat{s}^x \hat{s}^x \,|\, s, \Omega \,\rangle &= \langle\, s \,|\, \hat{U}^\dagger \hat{s}^x \hat{U} \hat{U}^\dagger \hat{s}^x \hat{U} \,|\, s \,\rangle \\ &= \frac{1}{4} \langle\, s \,|\, \left(\hat{U}^\dagger \hat{s}^+ \hat{U} + \hat{U}^\dagger \hat{s}^- \hat{U} \right)^2 \,|\, s \,\rangle \\ &= \frac{1}{4} s \left[1 + \cos^2\theta + \left(4s \cos^2\phi - \cos 2\phi \right) \sin^2\theta \right] \;, \end{aligned} \tag{4.45}$$

where we have made use of the definition of the spin coherent states (4.17) and the operator identities (4.19) through (4.21). The expectation values for other combinations α,β can be derived accordingly and are given in the appendix in eqs.(A.7)-(A.12). In the actual implementation, the interaction matrix J_{ij} is analyzed at the initialization stage, and the index sets $\{m, n, o\}$ and $\{a, b\}$ of contributing terms are saved in a table for fast access for the repeated calculation of moments.

Third moment

In principle, the above scheme could be used to calculated third moments (skewness) of the spectra. The evaluation of the third moment (cf. eq.(4.39)) requires the expansion of the expectation value of the cube of the Hamiltonian,

$$\begin{aligned}\langle\, s, \vec{\Omega} \,|\, \hat{H}^3 \,|\, s, \vec{\Omega} \,\rangle &= \langle\, s, \vec{\Omega} \,|\, \left(\sum_{i<j} J_{ij}\, \hat{s}_i \cdot \hat{s}_j \right)^3 \,|\, s, \vec{\Omega} \,\rangle \\ &= \sum_{i<j} \sum_{k<l} \sum_{m<n} J_{ij} J_{kl} J_{mn} \langle\, s, \vec{\Omega} \,|\, (\hat{s}_i \cdot \hat{s}_j)\,(\hat{s}_k \cdot \hat{s}_l)\,(\hat{s}_m \cdot \hat{s}_n) \,|\, s, \vec{\Omega} \,\rangle \;. \quad (4.46)\end{aligned}$$

Whereas the square of the Hamiltonian yielded two types of contributing terms to the second moment, the situation is much more complicated for the cube. We have identified seven types of contributions in the index set $\{i, j, k, l, m, n\}$. Thus, the calculation of the third moment of $\hat{H}$ from the parameters $\vec{\Omega}$ of the spin-coherent states needs a more refined case differentiation than the evaluation of the second moment, and it would be numerically more time-consuming. We have therefore not implemented the third moment in our algorithm.

4.3 Algorithm

As we have stated in section 4.1, quantum spectrum and classical density of states can be related to each other, and the quantum spectrum can be written as an integral over contributions of states that are parametrized with $\vec{\gamma}$:

$$G^q(E) = \int \mathrm{d}\vec{\gamma}\, g(\vec{\gamma}, E) \;. \quad (4.47)$$

According to eq.(4.27), the spin-coherent states span the Hilbert space. Additionally, the expectation value of the Heisenberg Hamiltonian equals the energy of the corresponding vector array for the classical model (cf. eq.(4.29)). Hence we have a set of states that are complete on the Hilbert space and whose average energy coincides with the corresponding classical energy. However, the width of their energy distributions is not negligible (cf. Sec. 4.2.3). If this were the case, the quantum spectrum would already be well approximated by the classical density of states.

We base the approximation on the discrete representation of the integral over weighted spectra, introduced in section 4.1:

$$G^q(E,\epsilon) \approx \sum_i G^c(E_i,\epsilon)\,\bar{g}_{E_i}(E)\ , \tag{4.48}$$

where E_i denotes the mean energy of the bin i.
In our approach, we cannot sum over the complete individual spectra of the contributing configurations as in eq.(4.47), because the calculation of these spectra would require the knowledge of the spectrum of the entire system. We will rather use approximations of the individual spectra $\bar{g}_{E_i}(E)$, based on the calculation of the moments of the energy distributions. For this purpose, we replace the spectra $\bar{g}_{E_i}(E)$ in eq.(4.48) by the normalized functions $f(E-E_i,\vec{\mu}(i))$. The vector $\vec{\mu}_i$ represents the moments of the energy distribution $\bar{g}_{E_i}(E)$, i.e.

$$\mu_0(i) = 1\ , \tag{4.49}$$
$$\mu_1(i) = 0\ , \tag{4.50}$$
$$\mu_2(i) = \langle\hat{H}^2\rangle - \langle\hat{H}\rangle^2\ ,\ \text{etc.} \tag{4.51}$$

The function $f(E)$ is an arbitrary function, with the constraint that it exhibits the specified moments. Only if all moments are known, f is fully specified and equals the spectrum $\bar{g}_{E_i}(E)$. The first moment has been set to 0 (rather than to $\langle\hat{H}^1\rangle = H(s,\vec{\Omega})$), so that we can use functions with vanishing average energy and shift them by the mean energy of the bin E_i when the summation is performed:

$$G^q(E,\epsilon) \approx \sum_i G^c(E_i,\epsilon)\,f(E-E_i,\vec{\mu}(i)) \tag{4.52}$$

The evaluation of (4.52) is performed in consecutive steps. In a first step, the classical spectrum $G^c(E,\epsilon)$ has to be acquired. For certain systems (cf. Sec. 3.3) the classical density of states can be calculated exactly, but usually a Wang-Landau procedure will be performed. In the second stage, the spectra of the states from the intervals E_i have to be calculated. These spectra cannot be calculated exactly in most cases, hence we will limit the calculation to a number of moments of the energy distributions. The third step incorporates the classical spectrum and the acquired moments of the quantum spectra for the calculation of (4.52), where we have to choose a broadening function complying with the moments.
Using the above recipe we have a converging scheme, which yields the exact quantum spectrum for the limit that both the exact classical density of states and all moments of the quantum mechanical energy distributions of the states in the intervals E_i are incorporated into eq.(4.52). For the actual implementation, as noted in section 4.2.4, we limit the calculation to the second moments.

Variance of quantum spectrum (high-T approximation)

As stated in the previous section, the estimate of the quantum spectrum is written as a sum over individual (normalized) spectra f_i centered at energies E_i, weighted with the classical weight $G^c(E_i)$:

$$G^q(E) = \sum_i G^c(E_i)\, f_i(E - E_i)\ , \tag{4.53}$$

$$\text{with}\ \sum_i G^c(E_i) = 1\ \text{ and }\ \int \mathrm{d}E\ f_i(E - E_i) = 1\ . \tag{4.54}$$

The variance of the quantum spectrum is then

$$\begin{aligned}
\sigma_q^2 &= \int \mathrm{d}E\ E^2\, G^q(E) - \left(\int \mathrm{d}E\ E\, G^q(E)\right)^2 \\
&= \sum_i G^c(E_i) \underbrace{\int \mathrm{d}E\ E^2\, f_i(E - E_i)}_{=\left(\sigma_i^2 + E_i^2\right)} - \left(\sum_i G^c(E_i) \underbrace{\int \mathrm{d}E\ E\, f_i(E - E_i)}_{=E_i}\right)^2 \\
&= \sum_i G^c(E_i)\sigma_i^2 + \underbrace{\sum_i G^c(E_i)E_i^2 - \left(\sum_i G^c(E_i)E_i\right)^2}_{=\sigma_c^2}\ ,
\end{aligned} \tag{4.55}$$

where σ_i^2 denotes the variance of the individual spectrum centered at E_i, and σ_c^2 is the variance of the classical spectrum. Following from the above, the variance of the quantum spectrum only depends on the classical spectrum and on the variances of the spectra $f_i(E-E_i)$. In other words, if the correct second moments of the contributions f_i are used for the approximation scheme, automatically the high-temperature limit of the specific heat will be reproduced correctly.

Sampling of the second moment

The second moments of the spin-coherent states are sampled with an algorithm similar to the Wang-Landau random walk. Starting from an arbitrary state, for each step, a new configuration is proposed by randomly changing the spin vectors. The probability of accepting the move is adopted from the Wang-Landau algorithm, eq.(3.48),

$$p\,(E_1 \to E_2) = \min\left(\frac{G^c(E_1)}{G^c(E_2)}, 1\right)\ . \tag{4.56}$$

For each configuration, the width of the energy distribution is calculated according to eq.(4.42) and used for the averages in the respective bin. The weights $G^c(E)$ have to

be known before the sampling of the moments can be started. They can be obtained from a previous Wang-Landau calculation and are not modified while performing the random walk for sampling the moments. The random walk with Wang-Landau transition probability is only used to achieve a flat histogram situation, i.e. each energy bin is visited equally often. Thus, the averaging of the moments will be of similar statistical quality in all bins.

4.3.1 Broadening functions with given second moment

For the broadening of the classical density of states, we have to choose a function $f(E, \vec{\mu})$ in eq.(4.52) that complies with the given moments μ_0 (normalization), μ_1 (centering), and μ_2 (width). We will now give examples of functions that have a specified second moment σ^2, a vanishing first moment, and are normalized to 1.

Gaussian

The most general form for a function, when only the variance is known, is the Gaussian distribution; it is the "most unbiased guess":

$$f(E) = \frac{1}{\sigma\sqrt{2\pi}}\, e^{-\frac{E^2}{2\sigma^2}} \,, \tag{4.57}$$

with no limitation to the energy interval. However, the use of unbounded distributions as broadening functions leads to unphysical results. Eq.(4.52) would yield a non-vanishing density of states in regions far outside the interval $[E_0^q, E_{\max}^q]$ given by the quantum Hamiltonian. As can be seen in the case of representing the spectrum by a single Gaussian (cf. Sec. 2.3.2), the specific heat diverges for the temperature T approaching zero.
Therefore, the following distributions are limited to a specified energy interval, and vanish for other energy values. We will list a set of functions that all comply with the above stated, and compare them with regard to their similarity with the Gaussian distribution.

Rectangle

The simplest form of a bounded distribution is a uniform distribution (rectangular shape), its functional representation can be given as

$$f(E) = \frac{1}{2\sqrt{3}\,\sigma} \quad \text{with} \quad |E| \leq \sqrt{3}\,\sigma \,. \tag{4.58}$$

The uniform distribution certainly is a very coarse approximation of the real distribution, since we know that the spectra of most spin-coherent states show a peaked weight around the mean energy (cf. Sec. 4.2.3).

Triangle

Therefore, a triangular shape is more appropriate. It can be described by

$$f(E) = \frac{1}{\sqrt{6}\,\sigma}\left(1 - \frac{|E|}{\sqrt{6}\,\sigma}\right) \quad \text{with} \quad |E| \leq \sqrt{6}\,\sigma\ . \tag{4.59}$$

Parabola

For numerical reasons, it is desirable to have "smooth" distributions, i.e. they should not introduce kinks to the density of states, as the previous two function do. The use of these distributions can lead to oscillatory behavior of functions derived from the spectrum, e.g. the specific heat.
A parabola eliminates the non-differentiable point at the center of the triangular distribution:

$$f(E) = \frac{3}{4\sqrt{5}\,\sigma}\left(1 - \frac{E^2}{5\,\sigma^2}\right) \quad \text{with} \quad |E| \leq \sqrt{5}\,\sigma\ . \tag{4.60}$$

Cosine

Leaving the class of polynomials, we introduce the cosine distribution, which has the advantage that it is differentiable at the boundaries of the interval:

$$f(E) = \frac{\sqrt{\pi^2 - 6}}{2\sqrt{3}\,\pi\sigma}\left[1 + \cos\left(\frac{\sqrt{\pi^2 - 6}}{\sqrt{3}\,\sigma}\,E\right)\right] \quad \text{with} \quad |E| \leq \frac{\sqrt{3}\,\pi\sigma}{\sqrt{\pi^2 - 6}}\ . \tag{4.61}$$

Comparison of the distributions

When we compare the graphs of the functions introduced above in figure 4.3, we find that the cosine is the "most similar" to the Gaussian. Speaking in terms of information theory, the cosine function has the largest Shannon entropy in this set of bounded functions (the Gaussian maximizes the Shannon entropy). We choose the cosine function as broadening function with given second moment, since it combines the advantages of being smooth on the defining interval, vanishing at the boundaries, and containing the least information of the presented distributions.

4.3.2 Results

The algorithm described above is now applied to an exactly solvable system, namely the ring with $N = 6$ and $s = \frac{5}{2}$. Systems with a spin quantum number as large as $s = \frac{5}{2}$ are often considered to be close to the classical regime, and classical methods are used to describe their properties [11]. Hence the correction to the classical density of states introduced by the scheme presented above should only be minor.

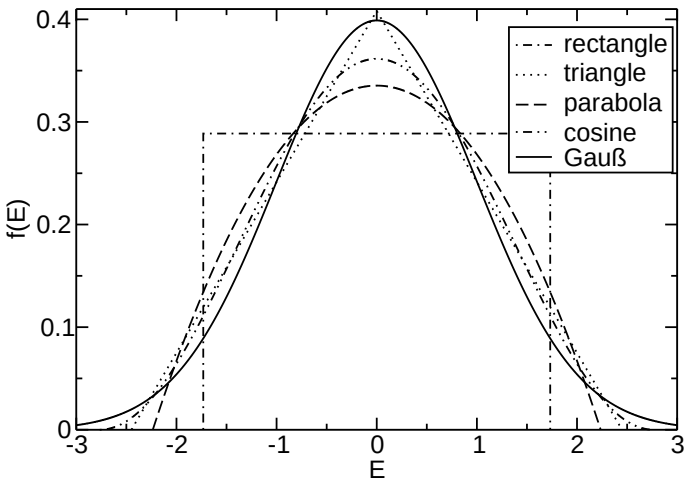

Figure 4.3: Comparison between different broadening functions. The second moment is $\sigma = 1$ for all curves

As we have demonstrated in section 3.5, we can accurately calculate the density of states for this system. The acquisition of the second moments is performed according to the modified Wang-Landau procedure. Since we will average over the second moments in each bin, we have to analyze how these moments are distributed, in order to justify this procedure. If the variance of the uncertainties of the spin-coherent states in the same bin was too large, this averaging procedure would not be appropriate.

Distribution of the second moment

Figure 4.4(left) shows the distribution of the uncertainty of the spin-coherent states as a function of energy. The uncertainty vanishes for the fully magnetized state with energy $E = JNs^2$, because it is a direct mapping of the classical state to the quantum state with maximum M quantum number. The uncertainty exhibits three local maxima and does not vanish for the classical ground state, since the quantum spectrum of the corresponding spin-coherent state, unlike the spectrum of the maximum energy state, is comprised of many contributions.

The standard deviation of the distribution of uncertainties in the bins is shown in the right graph of figure 4.4. We find that for low energies, where the spectrum is important for low-temperature properties of quantities such as the specific heat, the relative deviation is less than 10%, with a peak value of 20% in the total energy range. Thus, we conclude that the averaging procedure for generating $\sigma(E)$ is applicable.

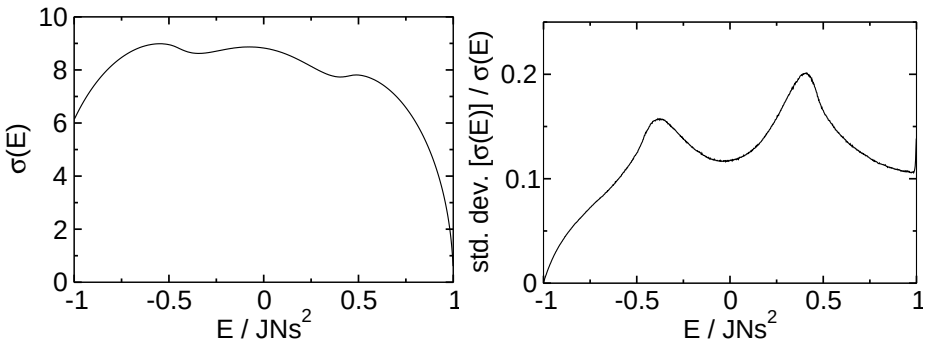

Figure 4.4: Left: distribution of the width of the spin-coherent wave-functions vs. energy. Right: relative standard deviation of wave-function widths contributing to the average of the respective bin E.

Broadening of the classical spectrum

With the gathered data of the uncertainty distribution, we can now perform the summation according to eq.(4.52). As noted in section 4.3.1, we use a cosine distribution as broadening function $f(E, \vec{\mu})$, since it represents a comparably weakly biased guess for the true energy distribution, while being bounded.

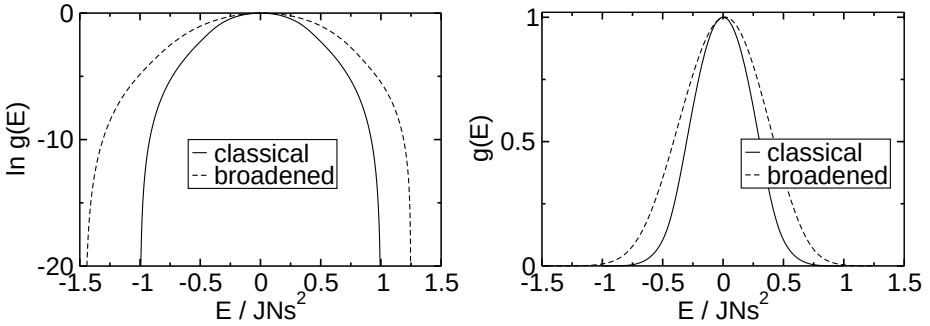

Figure 4.5: Classical density of states and broadened spectrum for the ring with $N = 6$, $s = \frac{5}{2}$. The left graph shows the logarithm of $g(E)$.

Figure 4.5 shows the resulting spectrum after the summation (4.52). In the linear plot, the Gaussian-like density of states appears to be scaled almost symmetrical about the maximum. The logarithmic plot, however, clearly illustrates that the broadening procedure has modified the low-energy region of the spectrum to a larger extend compared to higher energies. The ground state energy of the estimated quantum spectrum is shifted by about $0.5\,JNs^2$ from the classical ground state.

Although we have access to the complete quantum spectrum of the system, a direct comparison to the first approximation is not straightforward, since we would have to set up a measure for the difference of two spectra. As shown in section 2.3, the specific heat is very sensitive to deviations in the spectrum. Hence we will use $C(T)$ to judge the quality of our approximation.

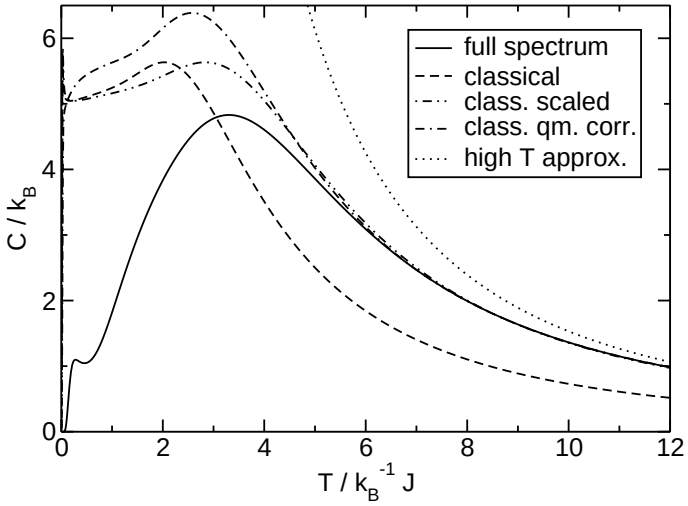

Figure 4.6: Specific heat for the quantum corrected density of states of the ring with $N = 6$, $s = \frac{5}{2}$.

Figure 4.6 shows the specific heat of the spin ring with $N = 6$, $s = \frac{5}{2}$ for the exact eigenvalue spectrum as well as for different approximations. The classical curve corresponds to the density of states $G^c(E)$, and the scaled classical result is obtained by multiplying all energies by the factor $\frac{s+1}{s}$, thus adjusting to a classical spin length of $|\mathbf{s}| = \sqrt{s(s+1)}$. The quantum corrected result represents the broadened spectrum generated with (4.52). For completeness, the high-temperature expansion (cf. Sec. 2.3.2) is given as well.

As shown above, the incorporation of the second moments for the broadening procedure automatically yields the correct high-temperature limit of the specific heat, since the variance of the approximate spectrum equals the variance of the true quantum spectrum. Figure 4.6 confirms the correct high-temperature behavior and also shows that our approximation can accurately describe the specific heat down to temperatures of about $6\,k_{\mathrm{B}}^{-1}J$. Qualitatively, the low-temperature behavior is only similar to the exact quantum result. Our approach is therefore superior to a pure high-temperature expansion, which approaches the exact quantum result just at the border of this figure ($\sim 12\,k_{\mathrm{B}}^{-1}J$).

On the other hand, however, the low-temperature behavior is not accurately reproduced, and even the simple rescaling of the density of states yields an approximation of the same quality.

4.3.3 Discussion

The algorithm presented in this section was developed as a numerical tool for the calculation of an approximation of the quantum energy spectrum of magnetic molecules. It is a converging scheme, in the sense that the use of all moments of the contributions $\bar{g}_{E'}(E)$ for the approximation (4.52) will yield the exact quantum spectrum.
Especially for large spin quantum numbers such as $s = \frac{5}{2}$, we expected to obtain good results from the method, since this situation is often referred to as being close to the classical limit. Therefore, the corrections introduced by the moments of the spin-coherent states should have been small.
However, when we review figure 4.4, we find that the peak width of the spin-coherent states is about $8\,J$. From section 2.3.2, or alternatively from exact diagonalization data, we can calculate the width of the total quantum spectrum. For a ring system, the total width is $\sigma_{\text{total}} = \sqrt{\frac{N}{3}}s(s+1)\,J$, which is about $12.4\,J$ for the ring with $N = 6$, $s = \frac{5}{2}$. Thus, the corrections are of the order of magnitude of the width of the complete quantum spectrum. The system is evidently still far away from the classical limit, where the spectral contributions of the spin-coherent states will approach delta peaks.

Classical limit

As we have learned from the example given above, $s = \frac{5}{2}$ cannot be considered a "classical" spin. We will now analyze the characteristics of the width of the contributing spin-coherent states relative to the total width of the quantum spectrum. Figure 4.7 shows the average widths of the energy distributions of spin-coherent states with corresponding classical energies E for increasing spin quantum numbers s.
We find that, as expected, the width of the individual contributions decreases with growing spin quantum number s. However, the rate of decrease is rather slow. Whereas it is natural that for small s the contributions have to be widespread, since the system clearly is in the quantum regime for $s = \frac{1}{2}$ and $\frac{3}{2}$, we had expected the width of the spin-coherent states to be much smaller for large quantum numbers $s = 5$ or $s = 10$. Since the contributions are still significant for these large quantum numbers, we conclude that the convergence to the classical limit is much slower than initially expected. Hence it follows that classical methods for spins as large as $s = 10$ still cannot be applied without precaution, although $s = 10$ is often considered a classical spin.

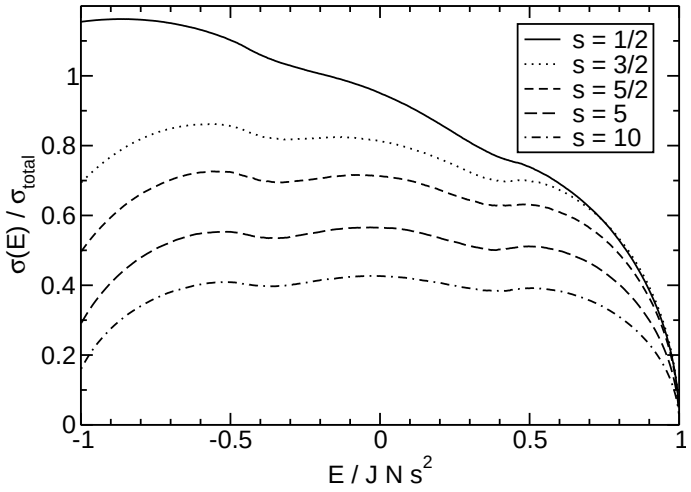

Figure 4.7: Distribution of the average width $\sigma(E)$ of spin-coherent states relative to the total width of the quantum spectrum for the ring with $N = 6$ for different spin quantum numbers s.

Shape of energy distributions $\bar{\mathbf{g}}_{\mathbf{E}'}(\mathbf{E})$

Since we have found in the previous paragraph that the corrections introduced by our method are not small, we will now discuss the shape of the energy distributions $\bar{g}_{E'}(E)$. Our algorithm will yield the correct quantum spectrum in the limit that the exact energy distributions $\bar{g}_{E'}(E)$ are known, i.e. all moments are incorporated into eq.(4.52). If the spectra of the spin-coherent states were narrow, symmetric broadening functions would probably yield adequate results. Due to the fact that the uncertainty of the spin-coherent states is of the order of magnitude of the width of the total spectrum, higher moments will have significant influence on the approximated spectrum (4.52).
Our approach was to implement only the second moments of $\bar{g}_{E'}(E)$, hence neglecting any asymmetry. The spin-coherent states are only symmetric in the center of the spectrum, i.e. for classical energies $E \approx 0$, but states near the classical ground state exhibit a significant third moment. Hence the assumption of symmetric broadening functions proves to be an oversimplification, and the existing asymmetry (skewness) of the spectra $\bar{g}_{E'}(E)$ would have to to be incorporated in order to achieve a more accurate approximation of the quantum spectrum.
Since the calculation of the third moments is a very (computer) time-consuming effort, our algorithm cannot be promoted as a standard numerical tool for the derivation of an approximate quantum spectrum. It is however valuable for the analysis of the way how a system approaches the classical limit, and whether it is justified to regard

a system as being in the classical regime.

4.4 Truncated classical spectrum

When we analyze the broadened spectrum (cf. Fig. 4.5) for the ring with $N = 6$, $s = \frac{5}{2}$, we find that the approximate quantum spectrum extends to very low energies. However, we can calculate the ground state energy of the quantum mechanical Hamiltonian exactly for this system, and even for larger systems this information is available via Lanczos and DMRG calculations. We will now discuss the effect of incorporating the constraint into the approximation that the spectral weight vanishes below the true quantum ground state.
Figure 4.8 shows the classical spectrum of the ring $N = 6$, $s = \frac{5}{2}$ as well as the scaled spectrum corresponding to a spin length of $|\mathbf{s}| = \sqrt{s(s+1)}$. The ground state energy of the system (obtained from exact diagonalization) is marked by the dotted line.

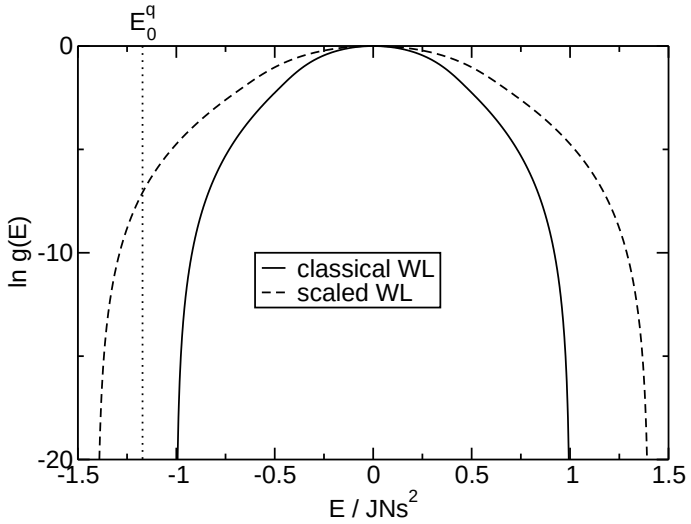

Figure 4.8: Classical spectrum of the ring with $N = 6$, $s = \frac{5}{2}$ for both spin lengths of s and $\sqrt{s(s+1)}$. The dotted line marks the quantum mechanical ground state of the system.

We will now take the scaled spectrum, which extends beyond the true ground state energy E_0^q, and truncate it to the allowed energy interval above E_0^q. The resulting spectrum is then used to calculate an approximation of the specific heat for this system. Figure 4.9 shows a comparison of the approximated specific heat, obtained from the scaled and truncated spectrum, with the exact result. Additionally, it shows

the result from the scaled spectrum, which is equivalent to a classical Monte Carlo simulation with spin length $|s| = \sqrt{s(s+1)}$.

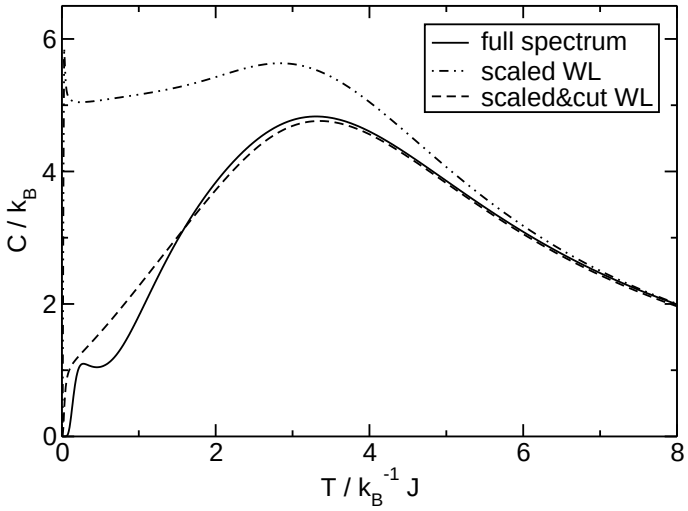

Figure 4.9: Specific heat for the spin ring with $N = 6$, $s = \frac{5}{2}$ calculated from the full eigenvalue spectrum compared to scaled Wang-Landau result.

Astoundingly, the truncated spectrum yields a very accurate approximation of the specific heat for the complete temperature region. We analyzed various systems by applying the same approach, in order to identify the behavior found in the ring with $N = 6$, $s = \frac{5}{2}$ as either a singular phenomenon of this specific system or a general property of Heisenberg spin systems. Empirically, we find that the approach can accurately deliver the specific heat of all ring systems we analyzed, notably even for small quantum numbers s.

Figure 4.10 gives the results for the spin ring with $N = 10$ and the cuboctahedron (both for $s = 1$) as examples. As noted above, the specific heat for the ring system is approximated very accurately. We find that even for the frustrated structure of the cuboctahedron, the truncation approach can deliver an adequate result. Naturally it cannot predict the position and height of the Schottky-peak (cf. Sec. 2.3.1), since it is a property that depends solely on the gap between ground state and first excited state.

Summarizing the results, we state that the truncation method represents a tool that accurately predicts the specific heat of the quantum system from the corresponding classical density of states. However, we have not developed the method based on a theory that describes the relations between the quantum spectrum and the truncated classical density of states. It was found coincidentally when we incorporated

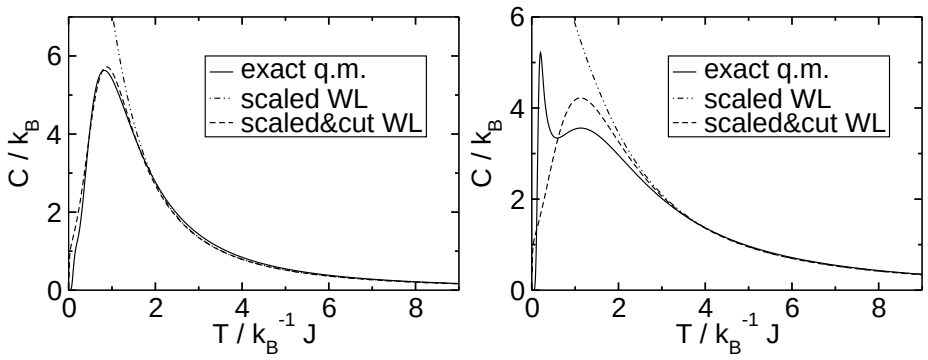

Figure 4.10: Specific heat for two systems with $s = 1$. Left: ring with $N = 10$, right: cuboctahedron. Each graph shows the exact quantum mechanical result and the scaled Wang-Landau data.

the ground state energy of the quantum Hamiltonian into the approximation. Hence further studies will have to be conducted in order to explain the success of the truncation method, which proved superior both to the approximate scheme presented in section 4.3 and to classical Monte Carlo calculations, while requiring a comparably small numerical effort.

5 Summary and outlook

In this work, we have presented different aspects of classical and quantum spectra of Heisenberg spin systems. For the class of quantum spectrum methods, we reviewed the rotational band model and analyzed it with respect to the behavior under the influence of an external magnetic field. The rotational band model was introduced to allow the calculation of an approximate low-energy spectrum for spin systems whose large Hilbert space dimensions preclude the use of exact diagonalization techniques. It simplifies the full Hamiltonian to an effective interaction between "super-spins", which represent the sites of sublattices of the total system. For two and three sublattices, the rotational band Hamiltonian is exactly solvable, and the energy eigenvalues can be expressed as a parabolic function of the total spin quantum number S. This is a significant simplification compared to the full Heisenberg Hamiltonian, and the validity of the model has to be verified for the systems it is applied to. For ring systems, both even numbered (bipartite) and odd numbered, the model is known to show good agreement in the low-energy region of the spectrum [13]. For $\{Mo_{72}Fe_{30}\}$, the model was shown to describe the series of ground state energies in subspaces $\mathcal{H}(S)$ correctly and to give accurate estimates for the magnetization depending on an applied magnetic field [24]. This is despite the fact that the molecule is of a more complicated structure that does not allow bipartition.

We utilized the rotational band model to predict results of inelastic neutron scattering experiments with $\{Mo_{72}Fe_{30}\}$, in order to verify the validity of the model by comparing to experimental results. To this end, we incorporated the general results for the dependence of the rotational band spectrum on the magnetic field into a scheme that approximates the inelastic neutron scattering cross-section as a function of the energy transfer.

For zero-field, our estimates showed a very good agreement with the experimental results for different temperatures of the sample. However, with a magnetic field present, the experimental results are inaccurate and do not allow a clear answer whether our simulation and therefore the rotational band model is valid in the form it is presented here. This is mainly because the scattering data contains a strong background from non-magnetic contributions, whose subtraction is not trivial. Since new experimental setups with better controlled background parameters have recently become available, one should pursue the analysis of $\{Mo_{72}Fe_{30}\}$ with neutron scattering. Further research can deliver more information on the true energy spectrum of the molecule, and it can tell us whether the rotational band model persists in the

form presented here, or to which extent it has to be modified in order to be able to reproduce these results. As a final remark on the rotational band model, it remains to emphasize that, up to now, it is still the only adequate model that describes the inelastic neutron scattering results.

In chapter 3 we introduced the classical density of states, which can be regarded as the analogon to the quantum mechanical eigenvalue spectrum, since its knowledge allows the calculation of thermodynamic averages. We have presented an exact solution for the class of spin rings, as well as the stochastic algorithms of classical Monte Carlo and Wang-Landau sampling, whereas only the latter can give a direct estimate of the density of states. We have demonstrated that the density of states is numerically accessible for models with continuous variables such as the Heisenberg model. However, for large systems such as $\{Mo_{72}Fe_{30}\}$, the evaluation poses a considerable numerical effort because of the huge differences of spectral weight between states near the ground state and states from the center of the spectrum.

We have limited the description of the density of states to a function of energy, but one can extend the definition to a function of both energy and magnetization $\rho(E, M)$. This allows the calculation of thermodynamic averages of magnetic quantities such as the susceptibility, as well. The approach with a joint density of states $\rho(E, M)$ has recently been demonstrated to be applicable to the three-dimensional Heisenberg model [52]. Alternatively, field-dependent quantities can be obtained by calculating $\rho(E)$ in independent Wang-Landau runs at different magnetic fields, which are kept constant within each run. This approach does not require any modification to the random walk algorithm, but only to the function that calculates the energy from the configuration of the system.

Although being an interesting field of research on their own, the methods for the description of the classical density of states were primarily introduced to form the basis of chapter 4, where we related the classical density of states to the spectrum of the corresponding quantum system.

We have established a scheme that expresses the total quantum spectrum of a system as an integral over individual quantum spectra weighted by the corresponding classical density of states. The method relies on special quantum states that allow a mapping of classical phase space points to elements of the Hilbert space. Whereas for the harmonic oscillator this mapping is accomplished by the coherent states, the analogous spin-coherent states exhibit this feature for Heisenberg spin systems. We have replaced the quantum spectra of the spin-coherent states by broadening functions, complying with a number of moments of the quantum spectra. This scheme is convergent, since if all moments agree, the exact quantum spectrum is obtained.

For numerical reasons, only the second moment of the distributions could be incorporated without rendering the algorithm unfeasible. For large spin quantum numbers such as $s = \frac{5}{2}$, we expected only minor corrections to the classical density of states. Our main goal was the prediction of the specific heat $C(T)$ for the molecule

$\{Mo_{72}Fe_{30}\}$, since there is no quantum method that can deliver accurate results. Quantum Monte Carlo is affected by the sign problem because of the frustrated structure of $\{Mo_{72}Fe_{30}\}$, and exact diagonalization techniques cannot deal with the large Hilbert space. Lanczos or DMRG method only target ground state (and very few excited states') properties, hence they cannot give thermodynamic averages. Classical Monte Carlo and spin-dynamics deliver impressive results for $\{Mo_{72}Fe_{30}\}$, but they are purely classical methods. Therefore, they do not feature a measure for the quality of the simulation, in terms of whether the system is in the classical regime or not.

Since we introduced a scheme that includes information of the quantum spectrum, we expected to obtain results superior to classical Monte Carlo. However, we found that the simplification to only use second moments of the energy distributions leads to results of the same quality as classical Monte Carlo. That is, the specific heat can be described well for high temperatures, whereas the region near to the peak and below cannot be reproduced correctly. This is despite the fact that our method extends the classical density of states based on the second moments of the spin-coherent states as a function of energy, while in classical Monte Carlo, the imitation of the quantum result is simply achieved by adjusting the spin length.

We have learned from these results that even for high spin quantum numbers such as $s = \frac{5}{2}$, the system is still far away from the classical limit, which is assumed for $s \to \infty$. We have also found that the convergence to the classical limit with growing spin quantum number is rather slow, so that, e.g., even $s = 10$ cannot be regarded as a completely classical spin.

Although the use of higher moments in our algorithm will lead to better results, we do not promote the method as a standard numerical tool for the calculation of thermodynamic quantities because of the significant numerical effort to include these moments. It is better suited for the analysis of "how classical" a given system is. We hence propose it as an accompanying tool that is utilized to verify the applicability of a classical numerical method.

Analyzing the effects of the broadening procedure in our algorithm, we discovered an interesting alternative method to estimate thermodynamic properties of the quantum spectrum. After calculating the density of states with the Wang-Landau algorithm and scaling the result to a spin length of $|\mathbf{s}| = \sqrt{s(s+1)}$, the energy interval is extended beyond the true quantum mechanical ground state of the system. Since the Rayleigh-Ritz constraint does not allow quantum states to exist below the ground state energy, we have truncated the broadened classical spectrum to the allowed quantum mechanical energy interval. The specific heat approximation obtained from the truncated spectrum described the exact quantum mechanical result very well. This extraordinary agreement was found for ring systems of various sizes and spin quantum numbers, and the method delivered adequate results even for the cuboctahedron. The clarification of the reasons for the success of this very simple approach

will have to be provided by further studies.
Since it has been demonstrated recently that the joint density of states $\rho(E, M)$ can be calculated for the Heisenberg model with a modified Wang-Landau algorithm [52], the truncation procedure should be applied to $\rho(E, M)$ as well. The possibility of an accurate estimation of magnetic properties such as the susceptibility would be an even more valuable tool, hence further investigations should be aimed at the correspondence of the classical $\rho(E, M)$ and the quantum spectrum.

A Appendix

A.1 Wigner's formula for rotation matrices

Reference [58] gives an explicit formula for the matrix elements of the rotation about the y-axis. We only present the result

$$\begin{aligned} d^{(j)}_{m'\,m}(\beta) &:= \langle\, j, m' \,|\, \exp\left(\frac{-\mathrm{i}\beta \hat{J}^y}{\hbar}\right) \,|\, j, m \,\rangle \\ &= \sum_k (-1)^{k-m+m'} \frac{\sqrt{(j+m)!\;(j-m)!\;(j+m')!\;(j-m')}}{(j+m-k)!\,k!\;(j-k-m')!\;(k-m+m')!} \\ &\qquad \times \left(\cos\frac{\beta}{2}\right)^{2j-2k+m+m'} \left(sin\frac{\beta}{2}\right)^{2k-m+m'} \quad . \end{aligned} \tag{A.1}$$

A.2 Summands of the variance of spin-coherent states

As shown in eq.(4.42), the variance of the energy distribution of a spin coherent state $|\, s, \vec{\Omega} \,\rangle$ can be expressed as

$$\sigma^2 = J^2 \left(\sum_{\{m,n,o\}} \sigma^2_{\{m,n,o\}} + \sum_{\{a,b\}} \sigma^2_{\{a,b\}} \right) \quad . \tag{A.2}$$

The summands can be expanded in terms of expectation values of first and second-order products of the spin operators:

$$\begin{aligned} \sigma^2_{\{m,n,o\}} = 2\Big[&\left(s^{xx}_m - (s^x_m)^2\right) s^x_n s^x_o + \left(s^{yy}_m - (s^y_m)^2\right) s^y_n s^y_o + \left(s^{zz}_m - (s^z_m)^2\right) s^z_n s^z_o \\ &+ \left(\mathrm{Re}(s^{xy}_m) - s^x_m s^y_m\right)\left(s^x_n s^y_o + s^y_n s^x_o\right) \\ &+ \left(\mathrm{Re}(s^{yz}_m) - s^y_m s^z_m\right)\left(s^y_n s^z_o + s^z_n s^y_o\right) \\ &+ \left(\mathrm{Re}(s^{zx}_m) - s^z_m s^x_m\right)\left(s^z_n s^x_o + s^x_n s^z_o\right) \Big] \end{aligned} \tag{A.3}$$

and

$$\begin{aligned}\sigma^2_{\{a,b\}} =& s_a^{xx}s_b^{xx} - (s_a^x s_b^x)^2 + s_a^{yy}s_b^{yy} - \left(s_a^y s_b^y\right)^2 + s_a^{zz}s_b^{zz} - (s_a^z s_b^z)^2 \\ &+ 2\Big[\mathrm{Re}\left(s_a^{xy}\right)\mathrm{Re}\left(s_b^{xy}\right) - s_a^x s_a^y s_b^x s_b^y \\ &+ \mathrm{Re}\left(s_a^{yz}\right)\mathrm{Re}\left(s_b^{yz}\right) - s_a^y s_a^z s_b^y s_b^z \\ &+ \mathrm{Re}\left(s_a^{zx}\right)\mathrm{Re}\left(s_b^{zx}\right) - s_a^z s_a^x s_b^z s_b^x\Big] \\ &- \frac{1}{2}\left[s_a^x s_b^x + s_a^y s_b^y + s_a^z s_b^z\right] \end{aligned} \tag{A.4}$$

with

$$s_k^\gamma := \langle\, s, \Omega_k \,|\, \hat{s}^\gamma \,|\, s, \Omega_k \,\rangle \;\text{ and }\; s_k^{\alpha\beta} := \langle\, s, \Omega_k \,|\, \hat{s}^\alpha \hat{s}^\beta \,|\, s, \Omega_k \,\rangle\,. \tag{A.5}$$

A.3 Expectation values of various operators for spin-coherent states

Expectation values of operator products of the form $\hat{s}^\alpha \hat{s}^\beta$ with $\alpha, \beta \in \{x, y, z\}$ can be calculated using the generating operator $\hat{U}$ of the spin-coherent states introduced in eq.(4.17), and the identities (4.19) and (4.20):

$$\langle\, s, \Omega \,|\, \hat{s}^\alpha \hat{s}^\beta \,|\, s, \Omega \,\rangle = \langle\, s \,|\, \hat{U}^\dagger \hat{s}^\alpha \hat{U} \hat{U}^\dagger \hat{s}^\beta \hat{U} \,|\, s \,\rangle \tag{A.6}$$

$$\langle\, s, \Omega \,|\, \hat{s}^x \hat{s}^x \,|\, s, \Omega \,\rangle = \frac{1}{4} s \left[1 + \cos^2\theta + \left(4s\cos^2\phi - \cos 2\phi\right)\sin^2\theta\right] \tag{A.7}$$

$$\langle\, s, \Omega \,|\, \hat{s}^y \hat{s}^y \,|\, s, \Omega \,\rangle = \frac{1}{4} s \left[1 + \cos^2\theta + \left(4s\sin^2\phi + \cos 2\phi\right)\sin^2\theta\right] \tag{A.8}$$

$$\langle\, s, \Omega \,|\, \hat{s}^z \hat{s}^z \,|\, s, \Omega \,\rangle = s^2 \left(\cos^2\theta + \frac{1}{2s}\sin^2\theta\right) \tag{A.9}$$

$$\langle\, s, \Omega \,|\, \hat{s}^x \hat{s}^y \,|\, s, \Omega \,\rangle = \frac{1}{2}\left[s\,(2s-1)\sin^2\theta\,\cos\phi\,\sin\phi + \mathrm{i}\,s\cos\theta\right] \tag{A.10}$$

$$\langle\, s, \Omega \,|\, \hat{s}^y \hat{s}^z \,|\, s, \Omega \,\rangle = \frac{1}{2}\left[s\,(2s-1)\sin\theta\,\cos\theta\,\sin\phi + \mathrm{i}\,s\sin\theta\,\cos\phi\right] \tag{A.11}$$

$$\langle\, s, \Omega \,|\, \hat{s}^z \hat{s}^x \,|\, s, \Omega \,\rangle = \frac{1}{2}\left[s\,(2s-1)\sin\theta\,\cos\theta\,\cos\phi + \mathrm{i}\,s\sin\theta\,\sin\phi\right] \tag{A.12}$$

Bibliography

[1] T. Lis. Preparation, structure, and magnetic properties of a dodecanuclear mixed-valence manganese carboxylate. *Acta Chrytallogr. B*, 36:2042, 1980.

[2] R. Sessoli, D. Gatteschi, A. Caneschi, and M. A. Novak. Magnetic bistability in a metal-ion cluster. *Nature*, 365:141, 1993.

[3] D. Gatteschi, A. Caneschi, L. Pardi, and R. Sessoli. Large clusters of metal ions: The transition from molecular to bulk magnets. *Science*, 265:1054, 1994.

[4] A. Müller, S. Sarkar, S. Q. N. Shah, H. Bögge, M. Schmidtmann, S. Sarkar, P. Kögerler, B. Hauptfleisch, A. X. Trautwein, and V. Schünemann. Archimedean synthesis and magic numbers: "sizing" giant molybdenum-oxide-based molecular spheres of the Keplerate type. *Angew. Chem. Int. Ed.*, 38:3238, 1999.

[5] D. Gatteschi. Molecular magnetism: A nasis for new materials. *Adv. Mater.*, 6:635, 1994.

[6] M. N. Leuenberger and D. Loss. Quantum computing in molecular magnets. *Nature*, 410:789, 2001.

[7] A. Bencini and D. Gatteschi. *Electron paramagnetic resonance of exchange coupled systems*. Springer, Berlin, Heidelberg, 1990.

[8] K. Bärwinkel, H.-J. Schmidt, and J. Schnack. Structure and relevant dimension of the Heisenberg model and applications to spin rings. *J. Magn. Magn. Mater.*, 212:240, 2000.

[9] U. Schollwöck. The density-matrix renormalization group. *Rev. Mod. Phys.*, 77:259, 2005.

[10] D. P. Landau and K. Binder. *A Guide to Monte Carlo Simulations in Statistical Physics*. Cambridge University Press, 2000.

[11] C. Schröder. *Numerische Simulationen zur Thermodynamik magnetischer Strukturen mittels deterministischer und stochastischer Wärmebadankopplung*. Dissertation, Universität Osnabrück, 1999. `http://elib.ub.uos.de/publications/diss/E-Diss28_arbeit.ps.gz`.

[12] L. Engelhardt and M. Luban. Low temperature magnetization and the excitation spectrum of antiferromagnetic Heisenberg spin rings. *Phys. Rev. B*, 2006. accepted.

[13] J. Schnack and M. Luban. Rotational modes in molecular magnets with antiferromagnetic Heisenberg exchange. *Phys. Rev. B*, 63:014418, 2001.

[14] J. Schnack, M. Luban, and R. Modler. Rotational band structure of low-lying excitations in small Heisenberg systems. *Int. J. Mod. Phys. B*, 17:5053, 2003.

[15] J. Gemmer, M. Michel, and G Mahler. *Quantum Thermodynamics*. Springer, Berlin, Heidelberg, 2004.

[16] W. Nolting. *Grundkurs Theoretische Physik 5/2 Quantenmechanik - Methoden und Anwendungen*. Springer, 2002.

[17] Linear Algebra PACKage. `http://www.netlib.org/lapack`.

[18] W. Nolting. *Grundkurs Theoretische Physik 6 Statistische Mechanik*. Springer, 2002.

[19] H.-J. Schmidt, J. Schnack, and M. Luban. Heisenberg exchange parameters of molecular magnets from the high-temperature susceptibility expansion. *Phys. Rev. B*, 64:224415, 2001.

[20] A. Lascialfari, D. Gatteschi, F. Borsa, and A. Cornia. Spin dynamics in mesoscopic size magnetic systems: A ^{1}H NMR study in rings of iron (III) ions. *Phys. Rev. B*, 21:14341, 1997.

[21] A. Lascialfari, D. Gatteschi, F. Borsa, and A. Cornia. Erratum: Spin dynamics in mesoscopic size magnetic systems: A ^{1}H NMR study in rings of iron (III) ions. *Phys. Rev. B*, 56:8434, 1997.

[22] G. L. Abbati, A. Caneschi, A. Cornia, A. C. Fabretti, and D. Gatteschi. [Fe(OCH3)2(dbm)](12): synthesis, solid-state characterization and reactivity of a new molecular ferric wheel. *Inorganica Chimica Acta*, 297:291, 2000.

[23] M. Axenovich and M. Luban. Exact ground state properties of the classical Heisenberg model for giant magnetic molecules. *Phys. Rev. B*, 63:100407, 2001.

[24] J. Schnack, M. Luban, and R. Modler. Quantum rotational band model for the Heisenberg molecular magnet $\{Mo_{72}Fe_{30}\}$. *Europhys. Lett.*, 56:863, 2001.

[25] M. Exler and J. Schnack. Evaluation of the low-lying energy spectrum of magnetic Keplerate molecules using the density-matrix renormalization group technique. *Phys. Rev. B*, 67:094440, 2002.

[26] S.R. White. Density matrix formulation for quantum renormalization groups. *Phys. Rev. Lett.*, 69:2863–2866, 1992.

[27] I. N. Bronstein, K. A. Semendjajew, G. Musiol, and H. Mühlig. *Taschenbuch der Mathematik*. Harri Deutsch, 2001.

[28] ISIS Pulsed Neutron & Muon Source. `http://www.isis.rl.ac.uk`.

[29] S. W. Lovesey. *Theory of Neutron Scattering from Condensed Matter*, volume 1 and 2. Oxford University Press, 1984.

[30] A. Müller, M. Luban, C. Schröder, R. Modler, P. Kögerler, M. Axenovich, J. Schnack, P. Canfield, S. Bud'ko, and N. Harrison. Classical and quantum magnetism in giant Keplerate magnetic molecules. *ChemPhysChem*, 2:517–521, 2001.

[31] W. Nolting. *Grundkurs Theoretische Physik 3 Elektrodynamik*. Vieweg, 1997.

[32] W.-K. Tung. *Group Theory in Physics*. World Scientific, 1985.

[33] O. Waldmann. Spin dynamics of finite antiferromagnetic Heisenberg spin rings. *Phys. Rev. B*, 65:024424, 2001.

[34] V. O. Garlea, S. E. Nagler, J. L. Zarestky, C. Stassis, D. Vaknin, P. Kögerler, D. F. McMorrow, C. Niedermayer, D. A. Tennant, B. Lake, Y. Qiu, M. Exler, J. Schnack, and M. Luban. Probing spin frustration in high-symmetry magnetic nanomolecules by inelastic neutron scattering. *Phys. Rev. B*, 73:024414, 2006.

[35] O. Waldmann, T Guidi, S. Carretta, C. Mondelli, and A. L. Dearden. Elementary excitations in the cyclic molecular nanomagnet Cr_8. *Phys. Rev. Lett.*, 91:237202, 2003.

[36] A. Tennant. Spin-polarized neutron scattering. Talk at the Mini Workshop Molecular Magnetism, Osnabrück, 2005.

[37] M. Toda, R Kubo, and N. Saito. Statistical physics I: Equilibrium statistical mechanics. In *Solid-State Sciences*, number 30. Springer, Berlin, Heidelberg, New York, 1978.

[38] M. E. Fisher. Magnetism in one-dimensional systems - The Heisenberg model for infinite spin. *Am. J. Phys.*, 32:343, 1964.

[39] G. S. Joyce. Classical Heisenberg model. *Phys. Rev.*, 155:478, 1967.

[40] M. Abramowitz, editor. *Handbook of mathematical functions with formulas, graphs, and mathematical tables*. Wiley, 1972.

[41] Wolfram Research Inc. *Mathematica*. Wolfram Research Inc., Champaign, Illinois.

[42] O. Ciftja, M. Luban, M. Auslender, and J. H. Luscombe. Equation of state and spin-correlation function of ultrasmall classical Heisenberg magnets. *Phys. Rev. B*, 60:10122, 1999.

[43] D. Mentrup. Untersuchungen zu kleinen Heisenberg-Spin-Systemen. Diplomarbeit, Universität Osnabrück, 1999.

[44] N. Metroplis, A. W. Rosenbluth, M. N. Rosenbluth, M. N. Teller, and E. Teller. Equation of state calculations by fast computing machines. *J. Chem. Phys.*, 21:1087, 1953.

[45] F. Alet, P. Dayal, A. Grzesik, A. Honecker, M. Körner, A. Läuchli, S. R. Manmana, I. P. McCulloch, F. Michel, R. M. Noack, G. Schmid, U. Schollwöck, F. Stöckli, S. Todo, S. Trebst, M. Troyer, P. Werner, and S. Wessel. The ALPS project: Open source software for strongly correlated systems. *J. Phys. Soc. Jpn. Suppl.*, 74:30, 2005.

[46] F. Wang and D. P. Landau. Efficient, multiple-range random walk algorithm to calculate the density of states. *Phys. Rev. Lett.*, 86:2050, 2001.

[47] D. P. Landau, S.-H. Tsai, and M. Exler. A new approach to Monte Carlo simulations in statistical physics: Wang-Landau sampling. *Am. J. Phys.*, 72:1294, 2004.

[48] C. Zhou and R. N. Bhatt. Understanding and improving the Wang-Landau algorithm. *Phys. Rev. E*, 72:025701, 2005.

[49] Ψ-Mag toolkit: C++ library for computational magnetism. `http://mri-fre.ornl.gov/psimag`.

[50] GNU scientific library. `http://www.gnu.org/software/gsl`.

[51] M. Matsumoto and T. Nishimura. Mersenne twister: a 623-dimensionally equidistributed uniform pseudo-random number generator. *ACM Transactions on Modeling and Computer Simulation*, 8:3, 1998.

[52] C. Zhou, T. C. Schulthess, S. Torbrügge, and D. P. Landau. Wang-Landau algorithm for continuous models and joint density of states. *cond-mat*, 0509335, 2005. `http://arxiv.org/cond-mat/0509335`.

[53] C. Cohen-Tannoudji, B. Diu, and F. Laloë. *Quantenmechanik Teil 1*. de Gruyter, 1997.

[54] M. Exler, J. Gemmer, and J. Schnack. On the correspondence of classical and quantum state densities: General theory and application to the strongly frustrated magnetic molecule $\{Mo_{72}Fe_{30}\}$. to be published.

[55] J. M. Radcliffe. Some properties of coherent spin states. *J. Phys. A: Gen. Phys.*, 4:313, 1971.

[56] R. Balakrishnan and A. R. Bishop. Nonlinear excitations on a quantum ferromagnetic chain. *Phys. Rev. Lett.*, 55, 1985.

[57] J. Schliemann and F.G. Mertens. Semiclassical description of Heisenberg models via spin-coherent states. *J. Phys: Condensed Matter*, 10:1091, 1998.

[58] J. J. Sakurai. *Modern Quantum Mechanics*. Addison Wesley, 1994.

Acknowledgments

I am particularly grateful to apl. Prof. Dr. J. Schnack for supervising my thesis. With his unmatched enthusiasm and extensive knowledge, he has always been a great source of inspiration. He also raised the funds for the project "Approximative Beschreibung antiferromagnetisch gekoppelter magnetischer Moleküle im Heisenberg-Modell", which allowed me to prepare my thesis in Osnabrück. The financial support by the DFG is gratefully acknowledged.
I would like to thank Jun.-Prof. Dr. J. Gemmer for many helpful discussions, particularly about the connection between classical and quantum world. Prof. Dr. K. Bärwinkel and apl. Prof. Dr. H.-J. Schmidt provided many useful suggestions and helped me to understand the theoretical background of spin systems.
Furthermore, I would like to thank Prof. M. Luban for the hospitality at the Ames Laboratory in Ames, USA and many fruitful discussions, especially about the rotational band model and neutron scattering. I am grateful to Prof. D. P. Landau for his hospitality at the Center for Simulational Physics at the University of Georgia, Athens, USA. Among many other numerical algorithms, he introduced me to the Wang-Landau technique presented in this work.
Finally, I would like to thank all members of the groups "Makroskopische Systeme und Quantentheorie" and "Quantenthermodynamik" at the physics department of the University of Osnabrück for creating an open and pleasant atmosphere, which made the past years very enjoyable.